Design, Modeling, and Simulation of Directly Frequency- and Intensity-Modulated Semiconductor DFB Lasers

DESIGN, MODELING, AND SIMULATION OF DIRECTLY FREQUENCY- AND INTENSITY-MODULATED SEMICONDUCTOR DFB LASERS

By Sangzhi Zhao, B.S., M.S.

A Thesis Submitted to the School of Graduate Studies in Partial Fulfilment of the Requirements for the Degree Doctor of Philosophy

DOCTOR OF PHILOSOPHY (2021) McMaster University
(Electrical and Computer Engineering) Hamilton, Ontario

TITLE: Design, Modeling, and Simulation of Directly Frequency- and Intensity-Modulated Semiconductor DFB Lasers
AUTHOR: Sangzhi Zhao, B.S. (Huazhong University of Science and Technology, China)
M.S. (Huazhong University of Science and Technology, China)
SUPERVISOR: Professor Xun Li
NUMBER OF PAGES: XV, 126

Lay Abstract

Semiconductor lasers are by far the most ubiquitous of all lasers, with their applications ranging from communication to manufacturing and from cooling of atoms to sensing of minor movement. And as the fabrication technique of semiconductor laser mature, numerical simulation tools now play the critical role in laser development.

This thesis focuses on the design and simulation of novel structures for distributed-feedback (DFB) lasers to improve the performance of such devices, including the frequency tuning efficiency, relative intensity noise (RIN), and modulation bandwidth. The proposed new structures and the underlying ideas led to them are thoroughly explained in the thesis. The device performances are also investigated numerically by applying traveling wave method (TWM). Simulation results are presented and discussed to provide design guidelines for the proposed structures.

Abstract

With the rapid development of fiber access networks, data centers, 5th generation cellular networks, and many more, there is an increasing demand for cost effective light sources possessing specification including high frequency modulation efficiency, low noise figure, and high data rate up to 40 Gb/s or even 100 Gb/s. Semiconductor lasers are considered the most attractive candidate in such applications for their low cost, high energy efficiency, and compact size. The focus of this thesis is the development of novel designs of semiconductor DFB lasers for device performance improvement with the help of numerical simulation tools.

The governing equations used in the simulation of DFB lasers are briefly explained, which covers the calculation of optical field, carrier transport, material gain, and thermal diffusion. The TWM based on these governing equations are adopted for the numerical laser solver used in the following chapters for device performance simulation.

Three novel DFB structures are then proposed in the thesis to achieve different specifications. The first proposed structure is a three-electrode DFB laser which can be directly frequency modulated. Numerical simulation shows that a high frequency modulation efficiency of 26GHz/mA from 0 to 100GHz and 17GHz/mA from 100GHZ to 200GHz can be achieved, respectively. Large-signal simulation of the waveform and eye-diagram of a frequency shift-keying (FSK) signal generated by the laser is also performed by converting it to an amplitude shift-keying (ASK) signal through an optical slope filter. The second proposed structure is a DFB laser with asymmetric λ/8 phase-shifted grating designed to flatten the relaxation oscillation peak through longitudinal spatial hole burning (LSHB) effect. Optimization of the phase-shift position to be 25% (in terms of the total length of the cavity) away from the high reflective (HR)-coated facet leads to reduced power leakage thus a higher quality factor of the cavity. The combined effect provides an improved RIN figure for the proposed DFB laser. The third proposed structure is a DFB laser with periodic current blocking grating. This novel grating is designed to improve the modulation bandwidth of DFB lasers by exploiting the enhancement of net differential gain. The effectiveness of the design is verified numerically, and excellent 3dB bandwidth enhancement are found for both uniform grating and λ/4 phase-shifted grating structures.

Acknowledgements

I would like to express my appreciation to everyone and anyone who have shown their support, provided guidance, and shaped me into who I am today.

Among them, I would like to express my deepest gratitude to Dr. Xun Li as my supervisor during my pursuit for the Ph. D. degree, for his insightful guidance and the passion for knowledge I learned from him. He did not only provide great supervision on my research, but also taught me how to be an independent researcher. He worked as a model with professionalism and responsibility.

I also wish to express my sincere thanks to the committee members, Prof. Shiva Kumar and Prof. Chang-Qing Xu, for their constructive criticism and valuable suggestions on my research. They have provided potential applications for my research I have missed, the ideas of how to improve my research skill, and more. I would like to thank them again for their time.

I greatly appreciate the administrative assistance I have received from Ms. Cheryl Gies. I am also grateful to all my colleagues in Photonics CAD Lab for their friendship and companionship.

Finally, my great gratitude and love to my parents Taoying Rui/GaishanZhao and wife Yi Zhang for their love, encouragement, and moral support. I owe them all I have achieved.

Abbreviations

AM: amplitude modulation

AR: anti-reflection

ASK: amplitude shift-keying

CPR: carrier-photon resonance

CW: continuous wave

DBR: distributed Bragg reflector

DFB: distributed-feedback

DFL: directly frequency-modulated laser

DL: detuned loading

DML: directly modulated laser

DR: distributed reflector

EML: external modulated laser

FFT: fast Fourier transform

FM: frequency modulation

FP: Fabry-Perot

FSK: frequency shift-keying

GRINSCH: graded index separate confinement heterostructure

HR: high reflection

IM: intensity modulation

LD: laser diode

LEF: linewidth enhancement factor

LI: light power vs current

LSHB: longitudinal spatial hole burning

MEMS: micro-electromechanical system

MMI: multi-mode interferometer

MQW: multiple quantum well

NF: noise figure

ODE: ordinary differential equation

ONU: optical network unit

PD: photodetector

PDE: partial differential equation

PFL: Passive-feedback laser

PON: passive optical network

PPR: photon-photon resonance

QWI: quantum well intermixing

RIN: relative intensity noise

ROADM: reconfigurable optical-add-drop multiplexer

ROF: radio-over-fiber

RW: ridge waveguide

SOA: semiconductor optical amplifier

SWM: standing wave method

TD: time domain

TWM: travelling wave method

TWDM: time and wavelength division multiplexing

WDM: wavelength division multiplexing

1D: one-dimensional

Contents

Lay Abstract ii

Abstract iii

Acknowledgements v

Abbreviations vi

Contents ix

List of Tables xi

List of Figures xii

Chapter 1 Introduction 1

- 1.1 Motivation 1
- 1.2 Recent Development 6
- 1.3 Thesis Outline 13

Chapter 2 Modeling and Solution Techniques for DFB Lasers 14

- 2.1 Introduction 14
- 2.2 Governing Equations 17
  - 2.2.1 Optical Wave Equations 17
  - 2.2.3 Carrier Rate Equations 20
  - 2.2.4 Material Gain Equations 21
  - 2.2.5 Thermal Diffusion Equations 24
- 2.3 1D Time Domain Traveling Wave Model 25
  - 2.3.1 Implementation of TWM 26
  - 2.3.2 Validation of Laser Solver 31
- 2.4 Summary 34

Chapter 3 Design of Directly Frequency-Modulated DFB Laser 35

- 3.1 Structure and Working Principle 35
- 3.2 Gain Elimination with QWI 40

3.3 Performance Simulation and Results 46
3.4 Summary 56
Chapter 4 Design of Direct-Modulated Semiconductor Laser with Asymmetric λ/8 Phase-Shifted Grating 58
4.1 Reduction of Relaxation Oscillation Peak and Improvement of RIN 58
4.2 Asymmetric λ/8 Phase-Shifted Grating 63
4.3 Performance Simulation and Results 67
4.4 Summary 78
Chapter 5 Design of Direct-Modulated Semiconductor Laser with the Periodic Current Blocking Grating 79
5.1 Comprehensive Rate Equation Model for Small Signal Response 79
5.2 Structure of the Periodic Current Blocking Grating 84
5.3 Performance Simulation and Results 88
5.4 Summary 98
Chapter 6 Conclusions and Future Work 100
6.1 Conclusions 100
6.2 Future work 101
Bibliography 103
Appendix A Derivation of Small Signal AM Response 121
Appendix B List of Publications Related to the Thesis Work 126

List of Tables

Table 2-1 Parameters in Ref [93]……………………………………………………………32

Table 3-1 Layer Structure for DFL……………………………………………………..37

Table 3-2 Parameters in DFL Simulation………………………………………………42

Table 4-1 Parameters in Laser Simulation…………………………………………….65

Table 4-2 Comparison Result for Ideal Facet condition (100% HR and 0% AR)……….67

Table 5-1 Layer Structure for the 1310nm DFB Laser………………………………..89

Table 5-2 Parameters in Laser Simulation…………………………………………….95

Table 5-3 3dB Bandwidth Enhancement ……………………………………………...99

Table 5-4 3dB Bandwidth Enhancement Under Constant Output Power (one facet)……99

List of Figures

Figure 1-1 Schematic illustration of the optical loopback technique in [1]........................2

Figure 1-2“pattern effect” in burst mode operation. 2

Figure 1-3 Schematic illustration of a ROF link. 4

Figure 1-4 Market share of telecommunication and data center. Source: Inphi Corp. Feb. 2020...5

Figure 1-5 Schematic illustration of Tunable laser array..8

Figure 1-6 Schematic illustration of (a) External cavity laser; (b) coupled cavity laser; (c) Vernier effect based laser...9

Figure 1-7 Schematic illustration of the detuned loading effect.......................................11

Figure 1-8 Schematic illustration of PPR. 12

Figure 2-1 Typical DFB laser structure. 16

Figure 2-2 Major physical processes in semiconductor laser. 16

Figure 2-3 Spatial grid for TWM..27

Figure 2-4 Marching of optical waves described in (2.28)...29

Figure 2-5 The flow chart of the 1D TD TWM solver. 30

Figure 2-6 LI curve. 32

Figure 2-7 (a) Carrier density and (b) photon density distribution...................................33

Figure 2-8 Large signal optical wave form...33

Figure 3-1 Schematic illustration of the DFL structure. 36

Figure 3-2 (a) Wavelength (frequency) detuning from the Bragg wavelength (frequency) as a function of the phase shift in grating center. (The cavity length is 300μm, the normalized coupling coefficient κL=2.8, both facet reflectivities are set to zero.) (b) Grating phase shift as a function of the effective index change Δn in the grating center. (Different markers are for different center lengths.) (c) Effective index change Δn as a function of the injected carrier density. (The inset shows material gain and material index change profiles. Different curves correspond to different injected carrier densities varying from 0.7×10^{18}cm^{-3} to 7×10^{18}cm^{-3}.)..39

Figure 3-3 Dependence of the lasing frequency tuning range on the normalized coupling coefficient κL. 39

Figure 3-4 (a) Average injected carrier density in the phase shift section as a function of I_m. (b) Lasing frequency tuning and optical power change as functions of I_m. (The inset shows the average effective index of DC biased section and the phase shift section as a function of I_m, respectively.) 43

Figure 3-5 (a) Material gain distribution along the laser cavity under different I_m. (b) Photon density distribution along the laser cavity under different I_m. (c) Carrier density distribution along the laser cavity under different I_m. (The inset shows the magnified local carrier density distribution from 0μm to 140μm.) 44

Figure 3-6 Calculated gain and index change profiles for InGaAsP/InP quantum wells (a) before intermixing; (b) after intermixing. 46

Figure 3-7 (a) Lasing frequency tuning as a function of I_m in DFL with the uniform and λ/4 phase-shifted grating, respectively. (The inset shows the photon density distribution inside the DFL cavity with the uniform and λ/4 phase-shifted grating, respectively.) (b) Optical power change as a function of I_m in DFL with the uniform and $\lambda/4$ phase-shifted grating, respectively. (The inset shows the average index changes of the phase shift sections under different I_m for two different gratings.) 48

Figure 3-8 (a) Lasing frequency tuning and optical power change as functions of I_m for different values of the grating coupling coefficient κ, with a fixed cavity length L of 300μm. (b) Lasing frequency tuning and optical power change as functions of I_m for different values of the cavity length L, with a fixed grating coupling coefficient κ at 100cm^{-1}. The phase shift section length L_2 is fixed at 20μm in both cases. (c) The grating Bragg stopband width in GHz for different combinations of (κ, L), where the dashed lines indicate fixed κL values of 1.0 to 5.0 (from bottom left to top right) with an increment of 1.0. 50

Figure 3-9 Lasing frequency tuning and optical power change as functions of I_m for different values of the phase shift section length L_2, with a fixed cavity length L of 300μm. 50

Figure 3-10 Lasing frequency tuning and optical power change of an optimized DFL as functions of the modulation current I_m at different output power levels. (The inset shows the LI curve of the optimized DFL.) 51

Figure 3-11 Emission spectrum of the DFL at different modulation current I_m with optical power of 2mW. 53

Figure 3-12 Lasing frequency tuning and optical power change as functions of the modulation current I_m with and without the thermal effect. (The inset shows the LI curve of the optimized DFL with and without the thermal effect.) 53

Figure 3-13 The frequency modulation response of the optimized DFL with different carrier lifetimes in the phase shift section. The carrier lifetime in the side sections are still 0.1ns, as listed in Table 3-2. 54

Figure 3-14 Schematic illustration of an optical FSK direct detection (DD) communication system with the DFL used as the light source 55

Figure 3-15 (a) The modulation current waveform. (b) The optical FSK signal power waveform. (c) The optical FSK signal power spectrum. (d) The optical IM signal power waveform after FSK to IM conversion by the slope filter. (e) The normalized eye-diagram. 56

Figure 4-1 Measured RIN in Ref [109] 61

Figure 4-2(a) Illustration of the flattening of small signal modulation transfer function with LSHB and (b) small signal modulation transfer functions of a conventional uniform grating DFB and a conventional λ/4 phase-shifted grating DFB. 63

Figure 4-3 Illustration of the (a) conventional λ/4 phase-shifted grating DFB and (b) the asymmetric λ/8 phase-shifted grating DFB. 64

Figure 4-4 Grating profile of the uniform grating (UG), the partially corrugated grating (PG), and the apodized grating (AG). 65

Figure 4-5 Normalized field distribution along laser cavity for UG, PG, AG, and conventional uniform DFB. 66

Figure 4-6(a) Modulation bandwidth, (b) linewidth, and (c) RIN peak value as the function of the grating phase-shift position. Power reflectivity of HR- and AR-coated facets are 90% and 0.1%, respectively. Cavity length is 400μm and output power is 20mW. 69

Figure 4-7 Normalized field distribution along laser cavity for different phase-shift positions. 70

Figure 4-8(a) Modulation bandwidth, (b) linewidth, and (c) RIN peak value as functions of the grating coupling coefficient κ at 20mW. 72

Figure 4-9(a) Modulation bandwidth, (b) linewidth, and (c) RIN peak value as functions of the cavity length L at 20mW. 73

Figure 4-10(a) Modulation bandwidth, (b) linewidth, and (c) RIN peak value as functions of the normalized coupling strength κL at 20mW. 75

Figure 4-11(a) LI curve and (b) normalized field distribution at 20mW for the optimized structure......76

Figure 4-12(a) Small signal AM Response and (b) RIN at 20mW for the optimized structure. 77

Figure 5-1 (a) AM response curves for different f_d with fixed f_r of 20GHz. (b) 3dB-bandwidth calculated from (5.1). 81

Figure 5-2 3D schematic diagram of the DFB laser. 84

Figure 5-3 (a) 3D schematic diagram of the periodic current blocking grating; (b) Side view of the grating structure; (c) Illustration of the current flow in high index and low index regions. 85

Figure 5-4 Normalized cavity loss of DFB laser as a function of the normalized grating coupling strength. 87

Figure 5-5 (a) Calculated refractive index change spectrum for the p-type grating layer; (b) Calculated Refractive index change as a function of the carrier density at 1310nm. The fitting polynomial is $\Delta n = p_1 \times N^3 + p_2 \times N^2 + p_3 \times N + p_4$ with $p_1 = -7.2598 \times 10^{-5}, p_2 = 0.0013 , p_3 = -0.0091 , p_4 = -4.0075 \times 10^{-4}$......91

Figure 5-6 (a) Example of the field distribution for optical mode in the cross-section and (b) the calculated κ~ Δn curve. 93

Figure 5-7 (a) L-I curves of DFB laser with conventional grating; (b) AM small signal response of conventional uniform grating DFB laser; (c) AM small signal response of conventional λ/4 phase-shifted grating DFB laser. 96

Figure 5-8 (a) L-I curves of DFB laser with conventional grating; (b) AM small signal response of conventional uniform grating DFB laser; (c) AM small signal response of conventional λ/4 phase-shifted grating DFB laser. 98

Chapter 1 Introduction

1.1 Motivation

Wavelength Tunable Laser:

1) Directly Frequency-modulated Laser (DFL)

DFLs are desirable in a variety of applications. Such devices can be used to generate FSK signal and to be combined with the ASK signal in optical loopback technique as illustrated in Figure 1-1, in which the downstream/upstream channels need to share the same wavelength for colorless optical network unit (ONU) in wavelength division multiplexing (WDM) passive optical network (PON) [1], [2]. As a FSK signal source, such a device can also be used to mitigate the "pattern effect" (i.e., the thermal crosstalk as shown in Figure 1-2) caused by the unbalanced heating of laser diodes between the "on" and "off" status when they are operated in burst mode status in time and wavelength division multiplexed (TWDM) systems with 100GHz or 50GHz channel spacing [3]. The thermal control circuits are usually too slow to offset this effect as the burst length in TWDM systems are in the order of micro-seconds. Under the FSK scheme, however, the transmitted power is always a constant regardless of symbol "on" or "off" in either normal or burst mode and the "pattern effect" naturally disappears. And since the FSK signal can be directly detected by passing the signal through an optical slope-filter prior to a photodetector (PD), no significant cost increase will be involved with this reconfiguration.

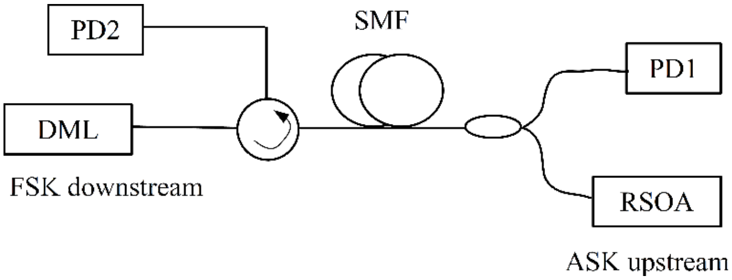

Figure 1-1 Schematic illustration of the optical loopback technique in [1].

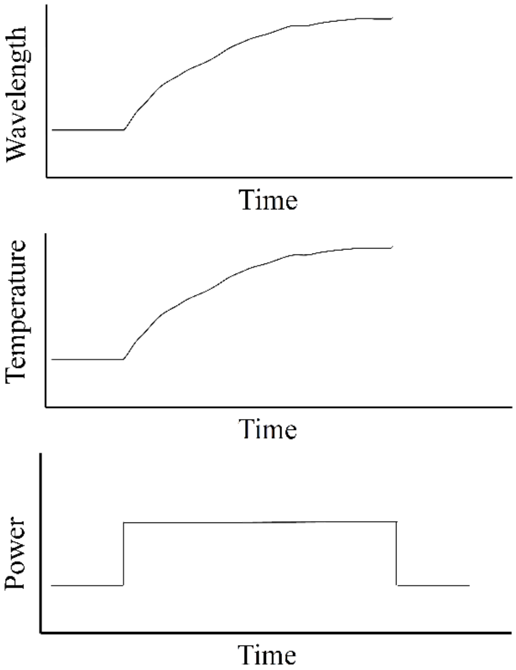

Figure 1-2“pattern effect” in burst mode operation.

DFL can also be used as the local oscillator in coherent detection systems [4], where only a fine tuning within a narrow band is required, for its short response time in frequency alignment with the incoming signal, low intensity fluctuation, and linear continuous wavelength tunability.

2) Wideband Tunable Laser with Low RIN

Wideband tunable semiconductor lasers are considered the key component in future optical communication and sensing systems [5], [6] with inventory reduction and flexibility [7] been the initial driver behind the pursuing of wavelength tunability. In WDM systems, dozens of fixed frequency lasers must be fabricated and inventoried for different signal channels. However, with full band tunability, single tunable lasers can work as a universal light source for all channels and greatly reduce the inventory of lasers. Wide range tunable laser can also find their applications in reconfigurable optical-add-drop multiplexers (ROADMs) [8] and optical switches of all kinds [9].

There are also applications for wideband tunable lasers in analog systems. With the development of wireless and mobile communication systems, the radio-over-fiber (ROF) link shown in Figure 1-3 is now attracting more attention as a promising candidate for their low loss, light weight, large bandwidth, and immunity to electromagnetic interference [10], [11]. The advantages of optical links also made them a better choice for other analog microwave systems, e.g., radar systems and cable TV [12]. Full-band wavelength tunability and narrow linewidth are also desired together with direct-modulation ability for lasers in such systems. Meanwhile, the main limiting factor of such analog systems is the noise figure (NF) which is proportional to the RIN of the light source and a typical RIN of less than -150dB/Hz from 0.1Hz to 20 GHz is required [13],[14]. Therefore, mitigation of the RIN of the semiconductor laser utilized in such systems becomes the key in the development of analog optical links. Semiconductor lasers with all the features can also find their applications in optical sensing systems [15], [16].

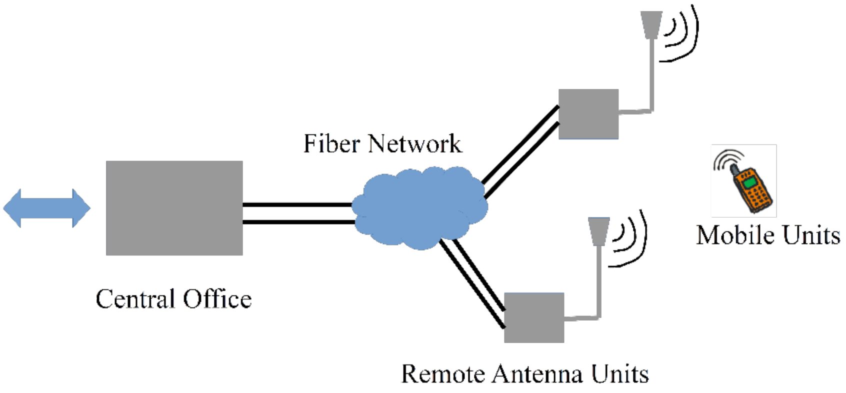

Figure 1-3 Schematic illustration of a ROF link.

Directly Modulated Laser (DML):

Single mode external modulated laser (EML) has previously dominated the market as the light source for the long-haul and backbone fiber-optic communication systems for their controlled chirp [17]. Deployment of EMLs in such systems is not cost-sensitive as the quantity of lasers used is limited and the high cost of EMLs is shared by a large amount of users. However, as shown in Figure 1-4, with the rapid development of fiber access networks [18], data centers [19], 5th generation mobile networks [20], [21], and many more sharing the feature of distributed networks, the number of lasers required increases drastically and the number of users who is going to share the cost of each laser decreases remarkably. For such systems, DMLs are considered the more attractive candidate over EMLs for their lower cost, higher energy efficiency, and compacter size [22].

The device performance of conventional DMLs is inferior when compared to EMLs, which is the result of handling the generation and modulation of the light power simultaneously. As a result, great interest has been drawn to the improvement of the performance of DMLs to make the commercialization possible. Among all the device characteristics, high modulation bandwidth [23] is the keystone of DML. Without a specialized design, the modulation bandwidth of a traditional DML is limited by its relatively low carrier-photon resonance (CPR) frequency at around 10~15 GHz [22]. A variety of approaches have been proposed to overcome this limitation of modulation bandwidth and some are successfully implemented in commercially available products operating at 25 Gb/s [24], [25], [26]. However, the fiber-optic communication systems have evolved from 10Gb/s, 4×25Gb/s, to 100Gb/s single channel, or even 400Gb/s [27]. And with an increased modulation bandwidth of DMLs, fewer channels are needed in such high-speed systems which will reduce the complexity and eventually the operational cost. Therefore, there is a great interest in pushing the modulation bandwidth of DMLs to over 40GHz under uncooled operation condition.

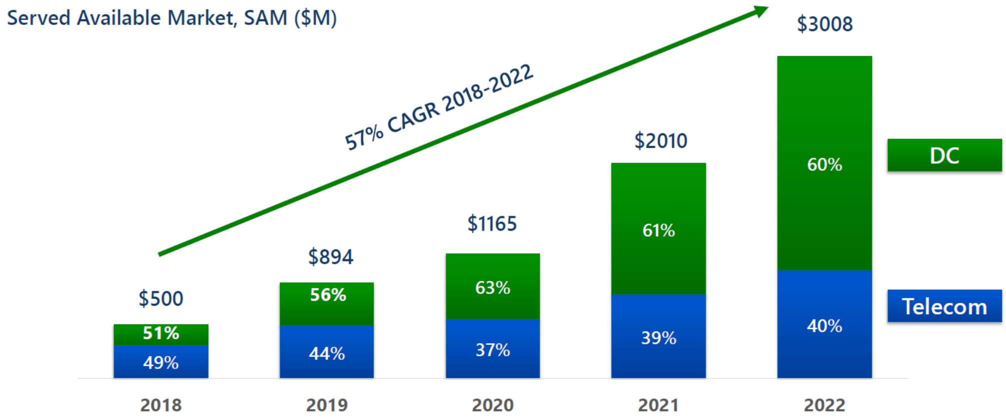

Figure 1-4 Market share of telecommunication and data center. Source: Inphi Corp. Feb. 2020.

1.2 Recent Development

Wavelength Tunable Laser:

1) Tuning Mechanism

The relationship between the lasing wavelength λ, effective refractive index $\bar{n}$, effective cavity length L, and the cavity mode number m is given by $m\lambda = 2\bar{n}L$ [7]. The lasing wavelength will change if any of the three, $\bar{n}$, L, or m, is changed and the relative change of wavelength can be derived as $\frac{\Delta\lambda}{\lambda} = \frac{\Delta\bar{n}}{\bar{n}} + \frac{\Delta L}{L} - \frac{\Delta \mathrm{m}}{m}$. The effective refractive index $\bar{n}$ can be directly tuned electronically or thermally and is the tuning mechanism behind most narrow band tunable lasers which can usually cover the range of 3~6 nm [28], [29]. The effective cavity length L can be tuned by physically moving the reflective mirror at one or two ends of the cavity, which is the main mechanism behind most micro-electromechanical system (MEMS) based tunable lasers [30], [31]. The cavity mode number m can be tuned using mode-selection filter, which is usually a grating [32], [33]. There is also the widely exploited Vernier effect which utilizes the two reflection combs with different wavelength spacings [34], [35]. Vernier effect will give a tuning range enhancement factor of $\Delta\lambda/\delta\lambda$. Here $\Delta\lambda$ is the average peak spacing in two combs and $\delta\lambda$ is the difference of the peak spacings between two combs.

2) DFL

DFLs can essentially be viewed as narrow band tunable lasers with high-speed tuning ability. Thermal or MEMS based tuning of index/cavity length/lasing mode suffers from slow response time and can not be used in such applications, which makes the electronical tuning of index the only possible approach. Several laser structures, including Fabry-Perot lasers [36], four-sectional distributed Bragg reflector (DBR) lasers [37], and single or multi-section DFB lasers [38], have been investigated for frequency modulation (FM) or FSK signal generation through direct modulation. Among them, the DFB laser structure presented the best performance in terms of dynamic single wavelength property and modulation speed. These previous works, however, either only exploited the parasitic frequency modulation effect accompanied with the intensity modulation (IM), and therefore suffered from a low frequency modulation efficiency around 0.1~1GHz/mA and a large residual IM or require selective growth in different sections to achieve nonuniform gain profiles [38], [39]. A solution with high modulation efficiency and no extra fabrication burden is still not achieved.

3) Wideband Tunable Laser with Low RIN

Wideband tunable semiconductor lasers can be categorized into (1) laser arrays [40], [41] and (2) individual lasers [42], [43], [44]. As shown in Figure 1-5, laser arrays consist of several individual narrow band tunable lasers, usually DFB lasers, each covering a portion of the total tuning range. An array with 12 DFB lasers can provide full C-band coverage utilizing thermal tuning [28]. Such devices can provide continuous and mode-hop-free tuning in the total operating range with simple control scheme, which is the result of the excellent mode stability of DFB lasers. However, a large loss is introduced at the multi-mode interferometer (MMI) or funnel combiner, therefore a SOA is needed after the combiner to boost the output power. The draw back of the laser arrays are large size, complexity in fabrication, and high-power consumption [28].

Individual wideband tunable lasers can generally be divided into external cavity lasers [45], [46], [47], coupled cavity lasers [48], [49], [50], and the lasers based on Vernier effect, e.g., sampled grating DBR laser [51], [52], multiple ring lasers [53], [54]. Examples of typical structures are shown in Figure 1-6. External cavity lasers can provide wide tuning range but suffer from low modulation speed and fabrication complexity. Coupled cavity lasers usually have mode hopping issue and are hard to reach large modulation bandwidth. Vernier effect based tunable lasers are the most accepted tunable light source today and can provide a maximum tuning range of 60nm [55], [56]. However, they also suffer from a low modulation speed due to the large cavity length, fabrication complexity due to the regrowth required, and complexity in operation due to the difficulty to obtain the combination of currents in different sections for a specific frequency.

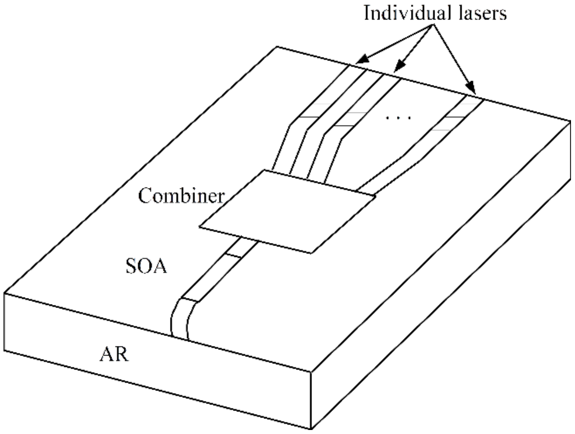

Figure 1-5 Schematic illustration of Tunable laser array.

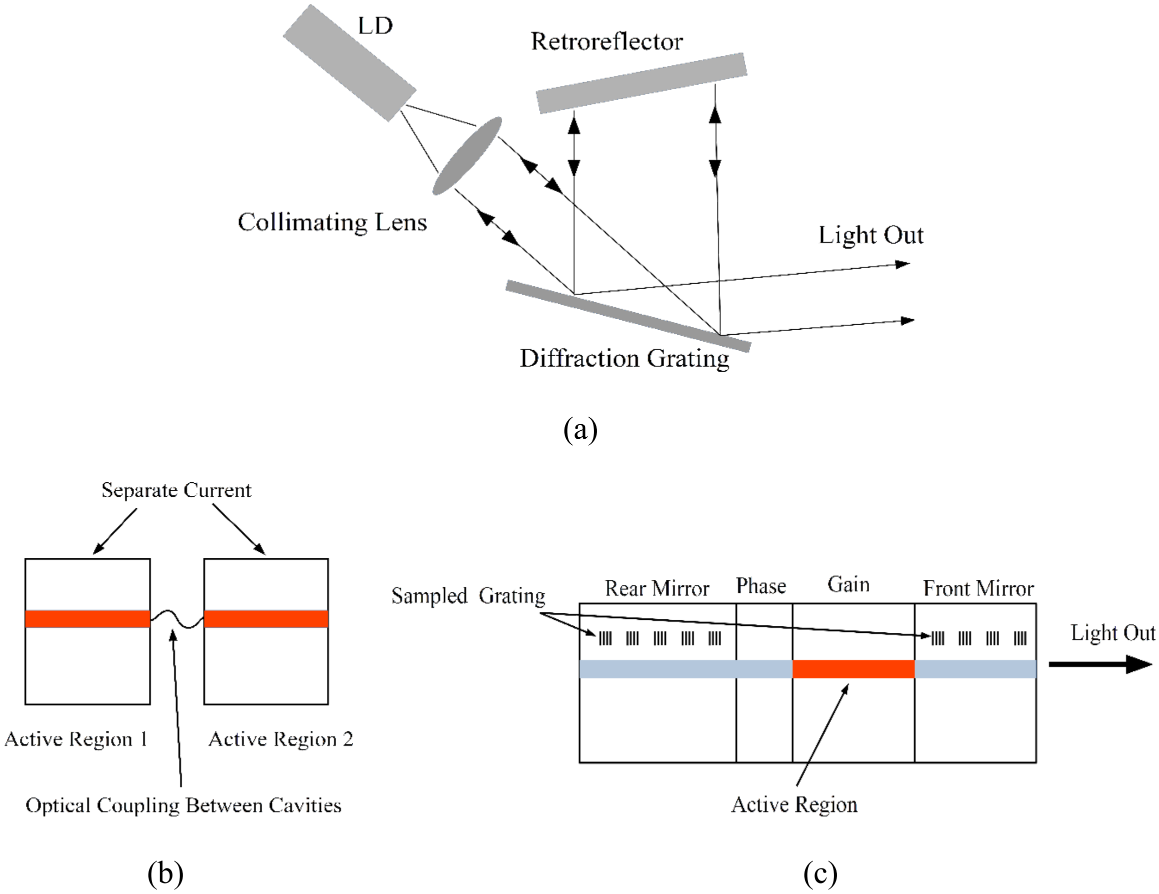

(a)

(b)

(c)

Figure 1-6 Schematic illustration of (a) External cavity laser; (b) coupled cavity laser; (c) Vernier effect based laser.

4) Laser with Low RIN

A variety of approaches have been investigated to suppress the RIN of the semiconductor lasers, with the easiest being increasing the laser bias to suppress the relaxation oscillation peak and push it to higher frequency [57]. A frequency-dependent loss can be put inside the cavity or an external dispersive component can be used to process the generated light from the laser to reduce the RIN through amplitude-phase noise decorrelation [58], [59]. Controlled optical feedback from external reflector into the laser and gain saturation in a SOA can also be utilized for RIN reduction [60]. However, these approaches either only reduce the RIN over limited frequency range or cannot be achieved monolithically. Asymmetric phase-shifted structure [61] has also been propose but the physical reason behind the RIN reduction with such structure has not been clearly identified and the position of the phase-shift is not optimized to our knowledge.

High Speed DML:

To overcome the limited modulation bandwidth of conventional DMLs, a variety of approaches have been proposed and investigated over the past decades. Compressive strained InGaAsP/AlGaInAs MQWs with optimized structure is used to improve the differential gain [62] and cavity length is shortened to reduce photon lifetime [63]. Combining of these two approaches have pushed the modulation bandwidth of the DMLs over 25 Gb/s [64]. Detuned loading (DL) effect is proposed and utilized firstly in DBR laser to improve the net differential gain and reached a modulation bandwidth of about 30 GHz [65]. As depicted in Figure 1-7, the improvement of the net differential gain is realized by positioning the lasing mode away from the reflection peak of the DBR and operating the laser in such a way that when the injected current is increased, the lasing mode moves towards the reflection peak. Membrane Lasers bonded onto SiC substrate can also be adopted to enhance the optical confinement factor [66] and be able to extend the 3dB bandwidth over 100GHz. However, the output power is limited below 1mW for the reported device.

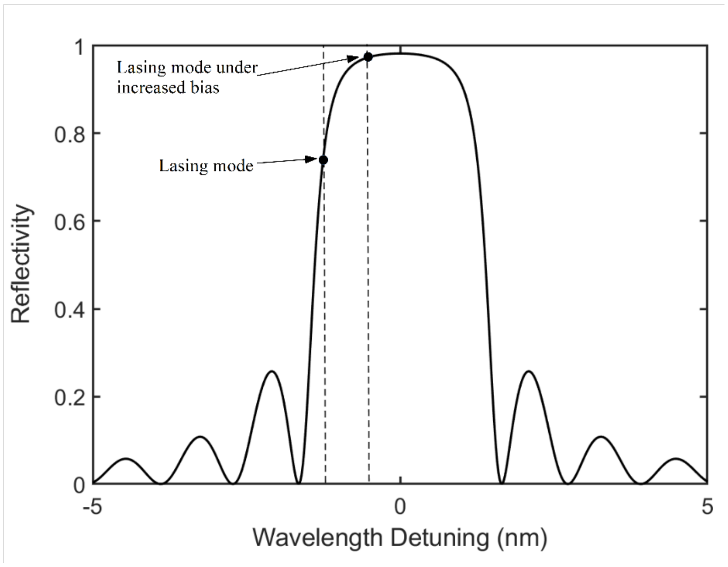

Figure 1-7 Schematic illustration of the detuned loading effect.

Aforementioned approaches all focus on improving the CPR frequency which is limited by the time constant of carrier and photon interaction. There are also other approaches trying to introduce the PPR to further increase the modulation bandwidth of DMLs [67], [68], [69]. As shown in Figure 1-8, the PPR effect is attributed to the existence of a second mode in the cavity that is separated spectrally from the dominate mode. The modulation sidebands of the dominate mode will then be resonantly amplified because of the cavity resonance of the second mode. Passive-feedback laser (PFL) [70], [71] and distributed reflector (DR) laser [72], [73] both utilize the PPR effect and are proposed to replace their discrete device counterparts to take advantage of monolithic integration. For a PFL, a passive waveguide is integrated with a DFB laser to provide optical feedback, therefore creating an external cavity mode in the vicinity of the main DFB mode. A modulation bandwidth of 37 GHz is realized by such a structure [70]. The DR laser proposed in [73] utilizes both detuned loading effect and PPR effect to further increase the modulation bandwidth to 50 GHz. The DR laser consists of a DFB section integrated with a DBR section for optical feedback. The DBR section provides a cavity mode for PPR effect and is also specially designed to adopt the DL effect. When the DFB section is modulated, the frequency up-chirp introduced by the plasma effect [74] will be translated into a reduction of cavity loss, which enhances the net differential gain by the DL effect.

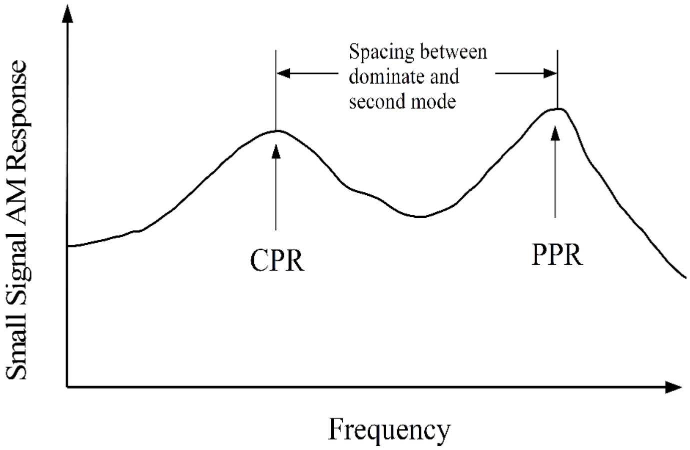

Figure 1-8 Schematic illustration of PPR.

With all the proposed approaches, due to the limited choices on material systems and the up-boundary of achievable strain for a reasonable quality of grown structure, the differential gain of strained-MQW has almost reached its limit. Designs taking advantage of detuned loading effect and PPR effect usually require the integration of active and passive waveguides in the same structure to avoid a significant optical loss, therefore a regrowth process is necessary. The membrane III-V laser on SiC also requires special bonding technique to combine the III-V active region with the low index SiC substrate.

Those extra burdens in fabrication could prohibit the application of such designs in cost sensitive scenarios.

1.3 Thesis Outline

This thesis contains six chapters in total. The 1st chapter is an introduction to the research covered in the thesis and the 6th chapter presents a summary of the principal findings of the study and concluding comments. The 2nd chapter provides a description of the modelling and solution techniques of semiconductor DFB lasers. The major contributions of this thesis are corresponding to the research work covered from chapter 3 to chapter 5. All the chapters are arranged as follows.

Chapter 3 presents a proposed 3-section DFL which can be used as a FSK signal generator or a linear and continuous narrow band tunable laser. An asymmetric λ/8 phase-shift DFB laser with low RIN will be presented in chapter 4 as a candidate of the individual laser used in tunable laser array. Chapter 5 is devoted to a DFB laser with periodic current blocking grating which can be used to improve the 3dB bandwidth of the laser.

Chapter 2 Modeling and Solution Techniques for DFB Lasers

2.1 Introduction

Almost six decades have been passed since the debut of the semiconductor laser in 1962 [75], [76], [77] and they have become an indispensable component of our daily life. And as the fabrication techniques for semiconductor lasers get mature and standardized, along with more challenging device performances are required by the market, device design is now playing the critical role in the development of new devices as well as optimization of existing devices for cost reduction. Computer aided design, modelling, and simulation becomes the indispensable tool for semiconductor lasers with complicated structure. The semiconductor laser models can generally be categorized into (1) behavior model and (2) physics-based model and compete on the trade-off between computational time and accuracy.

The behavior model, which is also known as zero-dimension rate equation model, ignores the physical size of the semiconductor lasers and treat the photons and carriers as collective quantities. The time dependent photon number and charge carrier number in the cavity are described by a set of coupled ordinary differential equations (ODEs). The rate equation model can only give an estimation of the laser performance with moderate accuracy and is usually integrated into signal propagation level simulation tools [78]. The physics-based models take into consideration of the spatial dependence for all physical quantities and give a description of the physical processes inside the devices. The most precise models are usually described by a quasi-3D system of partial differential equations (PDEs), which consider all 3 space dimensions but separate the 2D cross-section from the 1D longitudinal direction [79]. However, the simulation with such models could be time consuming. The 1D TWM [80] adopted in this thesis covers the spatial dependence in the direction along the laser cavity and is a compromise between accuracy and computational time.

The working principle of DFB laser was first introduced by Kogelnik and Shank with the coupled-mode theory [81]. A typical DFB laser structure is illustrated in Figure 2-1 and consists of (1) a waveguide to guide the optical waves along the laser cavity, (2) a Bragg grating to provide the coupling between forward and backward propagating optical waves, (3) an active region (strained MQW) to provide the optical gain through recombination, and (4) a forward biased PN junction along with a pair of electrodes to inject carriers into active region. There are mainly four coupled physical process inside a DFB laser as shown in Figure 2-2 [82]. Holes and electrons are injected from P-side electrode and N-side electrode respectively, and transport into active region through the PN junction. The holes and electrons then recombine inside the MQW in the active region and generate optical gain along with material refractive index change. The optical waves originated from spontaneous emission are guided by the waveguide and get amplified by the stimulated emission coherently. The optical waves also experience feedback from the Bragg grating and facets (if not AR coated). The temperature inside the device will also vary as heat is generated through nonradiative recombination and absorption of photons. The variation of the temperature will again affect the material properties and form the last chain of the loop.

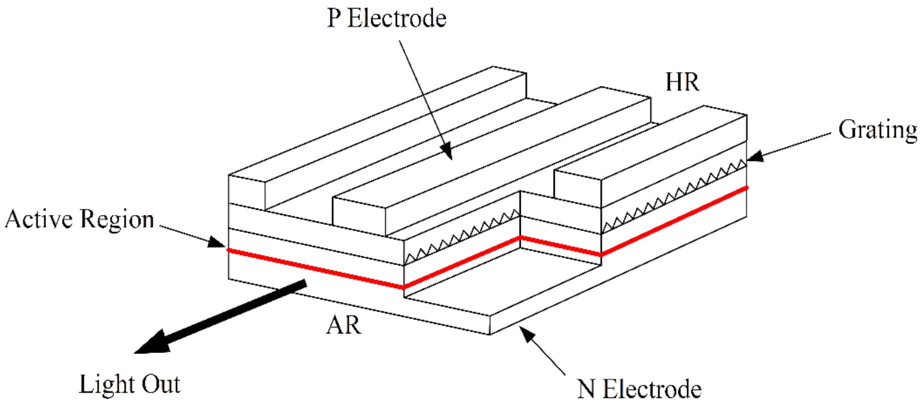

Figure 2-1 Typical DFB laser structure.

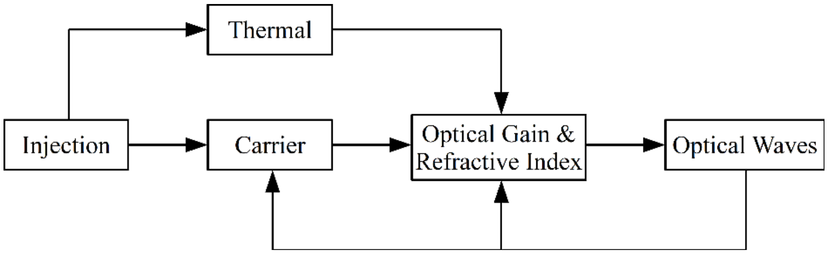

Figure 2-2 Major physical processes in semiconductor laser.

Four coupled governing equations are required to describe the four physical processes mentioned, which are:

1. Equations for waves,
2. Equations for carriers,
3. Equation for material gain,
4. Equations for heat.

The detailed governing equations will be given in section 2.2 and the time domain (TD) TWM will be discussed in section 2.3 with a summary covered in section 2.4.

2.2 Governing Equations

2.2.1 Optical Wave Equations

For DFB lasers, the electric field vector can be expressed as:

$$\boldsymbol{E}(x,y,z,t) = \frac{1}{2}\hat{\boldsymbol{s}}\sum_{i=1}^{M}\phi_i(x,y)\left[e_i^f(z,t)e^{j\beta_i z} + e_i^b(z,t)e^{-j\beta_i z}\right]e^{-j\omega_i t} + c.c., \qquad (2.1)$$

after making following assumptions [83]:

1. The optical wave travel along the waveguide direction only
2. The optical wave is fully confined in the cross-section area
3. The optical wave has slow-varying envelopes with discrete fast oscillation frequencies.

Here x, y is the cross-section directions and z is the wave propagating direction. $\hat{\boldsymbol{s}}$ is a unit vector in the (x,y) plane which denotes the polarization direction of the electric field and $\phi_i(x,y)$ is the normalized field distribution in the cross-section for the ith transverse mode. e_i^f and e_i^b are the forward and backward propagating slow-varying envelops of the ith transverse mode. $e^{-j(\omega_i t \pm \beta_i z)}$ represents the forward and backward traveling plane waves with frequency ω_i and propagation constant β_i . $c.c.$ stands for the complex conjugate of the preceding term on the right-hand side (RHS).

We can ignore the complex conjugate in (2.1) and consider only a single transverse mode with single polarization by assuming the linearity, which will give the well-known coupled equations for the slow-varying envelops as:

$$\left(\frac{1}{v_g}\frac{\partial}{\partial t} + \frac{\partial}{\partial z}\right)e^f(z,t) = \left\{j[\delta(z,t) + \Gamma k_0 \Delta n(z,t)] + \frac{1}{2}[\Gamma g(z,t) - \alpha_L]\right\}e^f(z,t) + j\kappa e^b(z,t) + s^f(z,t), \qquad (2.2a)$$

$$\left(\frac{1}{v_g}\frac{\partial}{\partial t}-\frac{\partial}{\partial z}\right)e^b(z,t)=\Big\{j[\delta(z,t)+\Gamma k_0\Delta n(N,P,T,\omega_0)]+\frac{1}{2}[\Gamma g(N,P,T,\omega_0)-\alpha_L]\Big\}e^b(z,t)+j\kappa^* e^f(z,t)+s^b(z,t). \quad (2.2b)$$

The assumption of a much broader system (indicated by χ) bandwidth compared to the signal (indicated by e) bandwidth is applied for the derivation of (2.2), which is valid for single frequency semiconductor lasers [82]. Here v_g is the group velocity of the optical waves inside the cavity, $k_0=\omega_0/c$ is the reference wave number, $\Delta n(N,P,T,\omega_0)$ is the material refractive index change which is connected to the material gain change through Kramers-Kronig transformation [84]. $g(N,P,T,\omega_0)$ is the material gain provided by the active region and α_L is the internal optical loss inside the cavity. Γ is the optical confinement factor of the transverse mode, κ and κ^* are the grating coupling coefficients for backward to forward and forward to backward coupling of the optical waves, and δ is the detuning factor, which are defined as:

$$\Gamma=\int_{AR}\phi^2(x,y)dxdy, \quad (2.3)$$

$$\kappa=\frac{k_0}{2n_{eff}^0}\int_\Sigma[\chi_H(x,y,z,\omega_0)-\chi_L(x,y,z,\omega_0)]\phi^2(x,y)dxdy, \quad (2.4)$$

$$\delta=\beta-\beta_0=\frac{2\pi n_{eff}^0}{\lambda_0}-\frac{m\pi}{\Lambda}. \quad (2.5)$$

Here AR and Σ indicate an integration in the active region and the entire cross-section region, respectively. λ_0 is the reference wavelength corresponding to the reference frequency ω_0, n_{eff}^0 is the effective refractive index without injection, $\beta\equiv k_0 n_{eff}^0$ and $\beta_0\equiv m\pi/\Lambda$ are the propagation and Bragg constant, respectively. m is the grating order and Λ is the grating period. $\chi_{H,L}$ are the susceptibilities in the high and low index (or gain) cross-section regions of the grating.

The material refractive index change term $\Gamma k_0 \Delta n(N, P, T, \omega_0)$ in (2.2) can be replaced by $-\alpha_H \Gamma g/2$ if we introduce the linewidth enhancement factor (LEF, also known as Henry's factor) α_H. LEF can be calculated follow the definition as [85]

$$\alpha_H = -\frac{dn/dN}{dg/dN}\frac{4\pi}{\lambda_0}. \tag{2.6}$$

The transverse mode $\phi_i(x, y)$ can be obtained along with β by solving the following eigen equation in (x, y) plane:

$$\nabla_t^2\phi(x, y) + k_0^2 n^2(x, y, \omega_0)\phi(x, y) = \beta^2\phi(x, y), \tag{2.7}$$

$s^{f,b}(z, t)$ are the spontaneous emissions noise contributing to the forward and backward propagating waves. The real and image part of $s^{f,b}(z, t)$ in (2.2) can be approximated by two independent Gaussian distributed random processes. Both Gaussian distributed random processes take zero mean and satisfies the autocorrelation function given as [82]:

$$\langle |s^{f,b}(z, t)||s^{f,b}(z', t')| \rangle = 2\sqrt{\frac{\mu_0}{\varepsilon_0}}\frac{\gamma\Gamma g_{sp}(N,P,T,\omega_0)\hbar\omega_0}{n_{eff}}\delta(z - z')\delta(t - t'), \tag{2.8}$$

where ε_0 is the vacuum permittivity, γ is the coupling parameter introduced to describe the percentage of photons coupled to the guided transverse mode inside the laser cavity at the lasing wavelength, and $g_{sp}(N, P, T, \omega_0)$ is the spontaneous emission gain.

The boundary conditions at the two facets are given as:

$$e^f(0, t) = r_L e^b(0, t),\ e^b(L, t) = r_R e^f(L, t), \tag{2.9}$$

where 0 and L are the positions of the left and right facet in z direction, $r_{L,R}$ are the amplitude reflectivity of the left and right facet. And the output power from the facets can be obtained by following

$$P_{out}^{L}(t) = \frac{dw}{\Gamma} v_g \frac{hc}{\lambda_0}(1 - r_L^2)|\, e^b(0,t)|^2, \tag{2.10a}$$

$$P_{out}^{R}(t) = \frac{dw}{\Gamma} v_g \frac{hc}{\lambda_0}(1 - r_R^2)\left|\, e^f(L,t)\right|^2, \tag{2.10b}$$

with Planck's constant h and active region width w and thickness d.

2.2.3 Carrier Rate Equations

The derivative of the carrier density along the wave propagating direction can usually be neglected as the diffusion length of minority carriers is much smaller compared to the total length of cavity [86]. Further, if the carrier transport effect in the cross-section area can be neglected, a carrier rate equation can be extracted from the more complicate carrier transport model. The carrier rate equation can be obtained by balancing the carrier generation and recombining rates

$$\frac{dN}{dt} = R_{gen} - R_{rec}. \tag{2.11}$$

Here R_{gen} is the rate of injected carriers from the bias current given as:

$$R_{gen} = \frac{\eta I}{eV}, \tag{2.12}$$

where η is the injection efficiency, I is the bias current, e is the unit charge, and V is the volume of the active region. R_{rec} is the recombination rate of the carriers and includes four components as follows

$$R_{rec} = R_{sp} + R_{nr} + R_{leak} + R_{st}, \tag{2.13}$$

where R_{sp} is the spontaneous recombination rate which involves the two-carrier spontaneous emission process and can be represented as BN^2, R_{nr} is the nonradiative recombination rate which involves the minority carrier SRH and Auger recombination process and can be represented as $AN + CN^3$. R_{sp} and R_{nr} can also be combined and represented as N/τ_e with τ_e be the carrier lifetime. R_{leak} is the carrier leakage rate which can usually be neglected and will not be considered here, and the last term R_{st} is the net stimulated recombination rate and can be represented as $v_g g P$. Therefore, the carrier rate equation (2.11) can be written as

$$\frac{dN(z,t)}{dt} = \frac{\eta I(z,t)}{eL\Sigma} - \frac{N(z,t)}{\tau_e} - v_g g(z,t)P(z,t), \tag{2.14}$$

2.2.4 Material Gain Equations

For semiconductor lasers, the stimulated and spontaneous emission gains can be calculated by applying the free carrier model, which assumes (1) it takes negligible time for injected carriers to reach their quasi-Fermi distributions at the lattice temperature; (2) the Coulomb interaction between carriers is fully screened and has no effects on the transition energy and dipole matrix element. By ignoring the many body effect, the stimulated and spontaneous emission gains of quantum well structures are given as [87]:

$$g(\omega_0) = \frac{\pi e^2}{n_r c \varepsilon_0 m_0^2 \omega_0} \frac{2}{L_W} \sum_\sigma \sum_{n,m} \int_0^\infty \frac{k_t dk_t}{2\pi} M_{nm}^\sigma(k_t) \times \frac{\Gamma_t/2\pi}{(\Gamma_t/2)^2 + \left(E_{hm}^{en}(k_t) - \hbar\omega_0\right)^2} [f_c^n(k_t) - f_v^{\sigma m}(k_t)], \tag{2.15a}$$

$$g_{sp}(\omega_0) = \frac{\pi e^2}{n_r c \varepsilon_0 m_0^2 \omega_0} \frac{2}{L_W} \sum_\sigma \sum_{n,m} \int_0^\infty \frac{k_t dk_t}{2\pi} M_{nm}^\sigma(k_t) \times \frac{\Gamma_t/2\pi}{(\Gamma_t/2)^2 + \left(E_{hm}^{en}(k_t) - \hbar\omega_0\right)^2} f_c^n(k_t)[1 - f_v^{\sigma m}(k_t)]. \quad (2.15b)$$

The non-parabolic valence band structure caused by valence-band-mixing is considered in (2.15) and the integrals are over the momentum space. $\hbar$ is the reduced Planck's constant, m_0 is the free electron mass, Γ_t is the Lorentzian linewidth broadening factor introduced to describe the intra-band scattering of electrons and L_W is the thickness of the quantum well. σ indicates the upper or lower blocks of the Hamiltonian used to calculate the band structures, and (n, m) are sub-band indices in conduction and valence band. $M_{nm}^\sigma(k_t)$ is the optical dipole matrix element between the nth sub-band in the conduction band and the mth subband in the valence band which is polarization dependent [88]. $E_{hm}^{en}(k_t)$ is the energy separation between the nth sub-band in the conduction band and the mth subband in the valence band. The dimensionless Fermi functions for the nth sub-band in the conduction band and the mth subband in the valence band are given as:

$$f_c^n(k_t) = \frac{1}{1 + e^{(E_g + E_{en}(k_t) - E_{Fc})/k_B T}}, \quad (2.16a)$$

$$f_v^{\sigma m}(k_t) = \frac{1}{1 + e^{(E_m^\sigma(k_t) - E_{Fv})/k_B T}}, \quad (2.16b)$$

with E_{Fc} and E_{Fv} defined as the quasi-Fermi levels in the conduction and valence bands, respectively. Given the electron and hole concentrations, the quasi-Fermi levels can be determined numerically and then be used in (2.15) to determine the stimulated and spontaneous emission gains.

To obtain the band structure and the electron and hole wave functions, the multiband effective-mass theory can be applied assuming the decoupling between the conduction and valence band [88]. The conduction band is assumed to be isotropic and take the parabolic band shape, whereas the valence band is described by a 4×4 Luttinger–Kohn Hamiltonian matrix derived from the k·p method [89]. The strain effect is added by including a Pikus–Bir perturbation term in the Hamiltonians [90]. The 4×4 Hamiltonian can be further block-diagonalized into two 2×2 matrices under a unitary transformation to reduce the effort for solving the eigenvalue equations [88]. The two block-diagonalized 2×2 matrices are the aforementioned upper and lower Hamiltonian and the eigen equations for them are given as:

$$-\begin{bmatrix} P+Q-V_h(y) & \tilde{R} \\ \tilde{R}^{+} & P-Q-V_h(y) \end{bmatrix} \begin{bmatrix} g^{(1)}(k_t,y) \\ g^{(2)}(k_t,y) \end{bmatrix} = E(k_t) \begin{bmatrix} g^{(1)}(k_t,y) \\ g^{(2)}(k_t,y) \end{bmatrix}, \tag{2.17a}$$

$$-\begin{bmatrix} P-Q-V_h(y) & \tilde{R} \\ \tilde{R}^{+} & P+Q-V_h(y) \end{bmatrix} \begin{bmatrix} g^{(3)}(k_t,y) \\ g^{(4)}(k_t,y) \end{bmatrix} = E(k_t) \begin{bmatrix} g^{(3)}(k_t,y) \\ g^{(4)}(k_t,y) \end{bmatrix}, \tag{2.17b}$$

with

$$P = P_\varepsilon + \frac{\hbar^2\gamma_1}{2m_0}(k_t^2 - \frac{\partial^2}{\partial y^2}), \tag{2.18a}$$

$$Q = Q_\varepsilon + \frac{\hbar^2\gamma_2}{2m_0}(k_t^2 + 2\frac{\partial^2}{\partial y^2}), \tag{2.18b}$$

$$\tilde{R} = \frac{\hbar^2\sqrt{3}}{2m_0}\bar{\gamma}k_t^2 - \frac{\hbar^2\sqrt{3}}{m_0}\gamma_3 k_t\frac{\partial}{\partial y}, \tag{2.18c}$$

$$\tilde{R}^{+} = \frac{\hbar^2\sqrt{3}}{2m_0}\bar{\gamma}k_t^2 + \frac{\hbar^2\sqrt{3}}{m_0}\gamma_3 k_t\frac{\partial}{\partial y}. \tag{2.18d}$$

Here $V_h(y)$ is the quantum well potential, P_ε, Q_ε are strain related terms, and $\gamma_{1,2,3}$ are the Luttinger parameters with $\bar{\gamma} = (\gamma_2 + \gamma_3)/2$ [91].

After solving the eigenvalue equations, the electron and hole wave functions can be readily obtained for the calculation of the optical dipole matrix elements. The sub-band energies obtained from (2.17) as the eigen values, together with the dipole matrix elements, can then be applied in (2.15) for the stimulated and spontaneous gain calculation.

Finally, the material refractive index change can be obtained by applying the Kramers-Kronig transformation on the stimulated emission gain following [82]

$$\Delta n(\omega_0) = -\frac{c}{2\pi\omega_0}\int_{-\infty}^{\infty}\frac{g(\omega_0)}{\omega-\omega_0}d\omega. \tag{2.19}$$

And the index changes calculated at different carrier densities can be utilized together with the calculated stimulate emission gains to extract the LEF α_H following (2.6).

2.2.5 Thermal Diffusion Equations

The temperature distribution $T(\boldsymbol{r},t)$ inside the cavity is generally governed by the 3D thermal diffusion equation [92]

$$\frac{\partial}{\partial t}T(\boldsymbol{r},t) = D\nabla^2 T(\boldsymbol{r},t) + \left\{R_t(\boldsymbol{r})\left[\frac{E_g}{e}J(t) - \frac{P_{op}(t)}{V}\right]\right\}_{AR} + R_t(\boldsymbol{r})R_s(\boldsymbol{r})VJ^2(t), \tag{2.20}$$

where the second and third term on the RHS work as the junction and Ohmic thermal sources, respectively. D is the thermal diffusion coefficient, $R_t(\boldsymbol{r})$ is the reciprocal of material thermal capacity per volume, E_g is the bandgap energy, $J(t)$ is the injection current density, $P_{op}(t)$ is the optical output power, and $R_s(\boldsymbol{r})$ is the material series resistance distribution.

To incorporate the thermal effect into the 1D TWM, we can extract from (2.20) a 1D thermal model by assuming that the thermal flux will mainly travel downwards from the active region to heat sink as the distance between these two regions is much less than other geometrical dimensions. The active region temperature distribution $T(z,t)$ in the 1D thermal model can be expressed analytically as [92]:

$$\mathrm{T}(z,\mathrm{t}) = T_e + \sum_{n=0}^{\infty} t_n^1 \int_0^t e^{-\left[\frac{(n+0.5)\pi}{h}\right]^2 D(t-\tau)} J^2(z,\tau)d\tau + \sum_{n=0}^{\infty} t_n^2 \int_0^t e^{-\left[\frac{(n+0.5)\pi}{h}\right]^2 D(t-\tau)} \times \left[J(z,\tau) - \frac{e}{E_g V} P_{op}(\tau)\right] d\tau, \tag{2.21}$$

with

$$t_n^1 = (-1)^n \frac{2V}{h_{as}} \int_0^h R_t(y) R_s(y) sin\left[\frac{(n+0.5)\pi y}{h}\right] dy, \tag{2.22a}$$

$$t_n^2 = \frac{2E_g d}{eh} R_t(h). \tag{2.22b}$$

Here y is the flow direction of the injected current and the upper boundary at active region is assumed to be adiabatic and the lower boundary in equilibrium with the heat sink. h_{as} and d are the distance from active region to heat sink and the thickness of active region. T_e is the equilibrium temperature without injection current.

If we further assume constant R_t and R_s along y direction, we can get rid of the integral in (2.22a) and reach

$$t_n^1 = (-1)^n \frac{2VR_tR_s}{(n+0.5)\pi}. \tag{2.23}$$

It's worth mentioning that the nonuniformity of the active region temperature distribution along the cavity is the result of the nonuniformly injected current.

2.3 1D Time Domain Traveling Wave Model

2.3.1 Implementation of TWM

In the 1D TD TWM, spatial dependence of all the physical quantities is considered in the wave propagation direction, while behavior in the 2D transverse cross-section is described by effective parameters, e.g., effective refractive index, optical confinement factor. The effective parameters are obtained by first solving eigen equation (2.7) for the transverse mode $\phi(x, y)$, then integrating over the cross-section region to reduce the (x, y) dependence of the parameters. By considering the spatial dependence, TWM can capture phenomena like LSHB as well as those arising from nonuniformity along the laser cavity. The TWM consists of the PDE system (2.2) describing the propagation of the coupled optical waves, the ODE system (2.14) describing the carrier generation and recombination in active region, and the analytical expression (2.21) for the temperature in active region. The stimulated emission gains are calculated with (2.15a) at different carrier densities and is then used to extract the differential gain coefficient g_N and transparent carrier density N_{tr} by fitting to the empirical gain model for QW active region [93]

$$g = g_N log\left(\frac{N}{N_{tr}}\right). \tag{2.24}$$

After g_N and N_{tr} are obtained, optical gain can be calculated using

$$g(z,t) = \frac{g_N \exp\left(-\frac{T(z,t)-T_r}{T_a}\right) log\left(\frac{N(z,t)}{N_{tr} exp\left(\frac{T(z,t)-T_r}{T_n}\right)}\right)}{1+\varepsilon P(z,t)}. \tag{2.25}$$

Here ε is the nonlinear gain saturation coefficient introduced to describe the nonlinear gain suppression due to the carrier heating and spectral hole burning, and $P(z,t)$ is the photon density. $T(z,t)$ is the temperature of active region and T_r, T_a, T_n are equilibrium temperature without injection, characteristic temperature for differential gain coefficient, and characteristic temperature for transparent carrier density. The temperature induced refractive index change should also be introduced as

$$\Delta n_{eff0} = \frac{1}{2n_{eff}} \times \frac{\partial^2 n_{eff}}{\partial T}(T(z,t) - T_r), \tag{2.26}$$

with $\frac{\partial^2 n_{eff}}{\partial T}$ assumed to be constant.

To implement the TD TWM, the structure is usually divided into subsections along the propagation direction and structural and material parameters are considered uniform in each subsection. (2.14), (2.21), and (2.25) are solved locally in each subsection at each time step, and the results are applied in (2.2) to trace the evolution of the envelops of the forward/backward propagating waves at the boundaries of the subsections as shown in Figure 2-3.

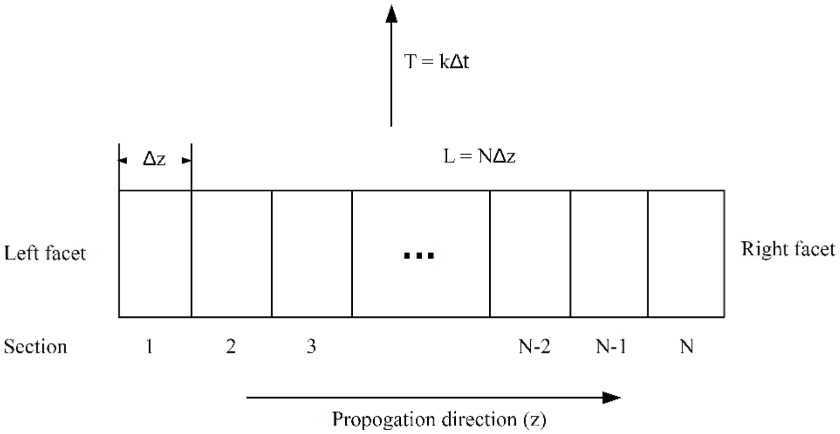

Figure 2-3 Spatial grid for TWM.

The coupled optical wave equations (2.2) can be solved with the split-step method by rewrite it in the form [94]

$$\pm\frac{\partial}{\partial z}\begin{bmatrix} e^{f}(z,t) \\ e^{b}(z,t) \end{bmatrix} = \begin{bmatrix} A^{11}(z,t) - \frac{1}{v_g}\frac{\partial}{\partial t} & A^{12}(z,t) \\ A^{21}(z,t) & A^{22}(z,t) - \frac{1}{v_g}\frac{\partial}{\partial t} \end{bmatrix}\begin{bmatrix} e^{f}(z,t) \\ e^{b}(z,t) \end{bmatrix} + \begin{bmatrix} C^{f}(z,t) \\ C^{b}(z,t) \end{bmatrix}. \tag{2.27}$$

Then the optical wave dependences on time and space are treated sequentially instead of simultaneously as did in the direct finite difference method. The sequentially obtained results can be combined to obtain the final form with the spontaneous emission contributions

$$\begin{bmatrix} e^{f}_{n+1,k+1} \\ e^{b}_{n,k+1} \end{bmatrix} = \frac{1}{\cosh(\gamma_{n,k}\Delta z) - \frac{A^{11}_{n,k} + A^{22}_{n,k}}{2\gamma_{n,k}}\sinh(\gamma_{n,k}\Delta z)}$$

$$\begin{bmatrix} e^{\frac{A^{11}_{n,k}-A^{22}_{n,k}}{2}\Delta z} & \frac{A^{12}_{n,k}}{\gamma_{n,k}}\sinh(\gamma_{n,k}\Delta z) \\ \frac{A^{21}_{n,k}}{\gamma_{n,k}}\sinh(\gamma_{n,k}\Delta z) & e^{-\frac{A^{11}_{n,k}-A^{22}_{n,k}}{2}\Delta z} \end{bmatrix}\begin{bmatrix} e^{f}_{n,k} \\ e^{b}_{n+1,k} \end{bmatrix} + \Delta z\begin{bmatrix} C^{f}_{n,k} \\ C^{b}_{n,k} \end{bmatrix}. \tag{2.28}$$

with $\gamma_{n,k}$ defined as

$$\gamma_{n,k} \equiv \pm\sqrt{\frac{A^{11}_{n,k}+A^{22}_{n,k}}{2}}^{2} - A^{12}_{n,k}A^{21}_{n,k}. \tag{2.29}$$

The length of each subsection Δz and the time step Δt should follow the relation

$$\Delta t = \Delta z / v_g. \tag{2.30}$$

The marching of the coupled optical waves in both space and time is illustrated in Figure 2-4.

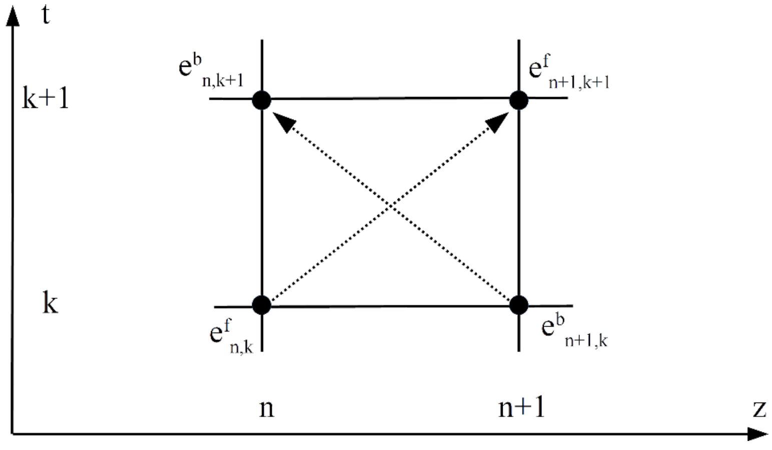

Figure 2-4 Marching of optical waves described in (2.28).

The carrier rate equation (2.14) could be solved with Runge-Kutta or Euler method with the time step determined from (2.30) [95]. The flow chart of the 1D TD TWM solver used in this thesis is presented in Figure 2-5 with the initial condition of $I(z,0) = 0, N(z,0) = 0, P(z,0) = 0$. The laser solver can carry out:

1. Threshold analysis,
2. Steady state analysis,
3. Small-signal analysis,
4. Large-signal analysis,
5. Spectrum analysis.

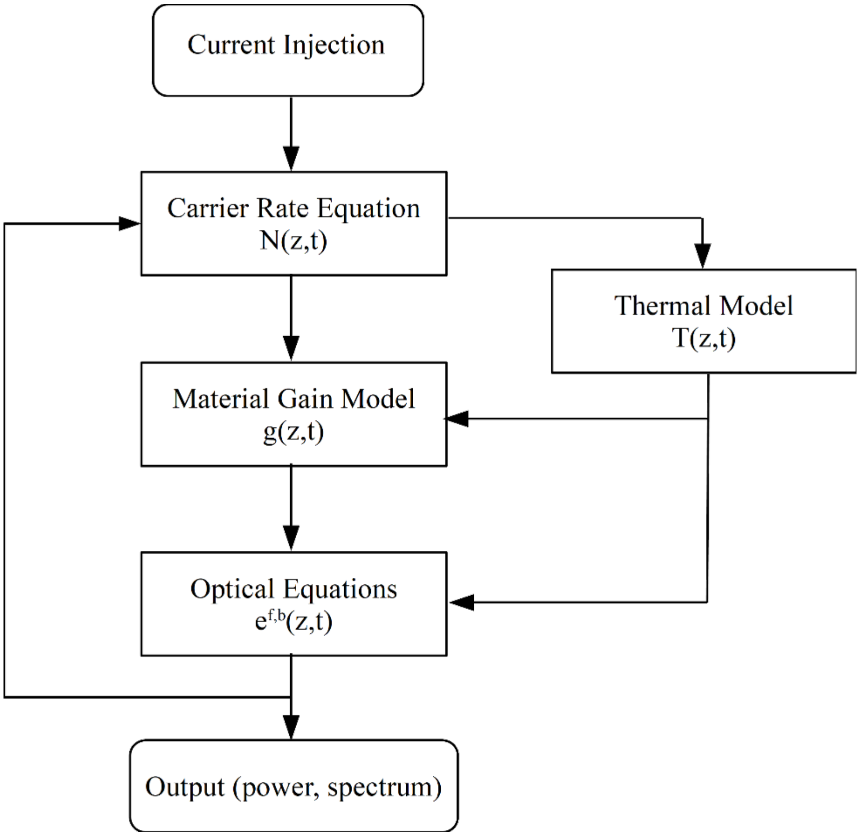

Figure 2-5 The flow chart of the 1D TD TWM solver.

The steady state analysis is performed by applying the desired DC current as the input and run the solver until the convergence is reached. Then the steady state distributions, i.e., carrier density distribution, normalized field distribution, together with the optical power from both facets given in (2.10) can be obtained. The optical spectrum can also be calculated by applying fast Fourier transform (FFT) to the time sequential output fields from both ends. The threshold current is determined by running steady state analysis for different DC currents and plotting the LI curve. Small signal analysis can be performed by providing a small sinusoidal AC current at different frequencies and collecting the sinusoidal optical output. Then the small signal response can be determined by dividing the peak-to-peak difference from the output by the peak-to-peak difference from the input over the frequency range of interest. The large signal analysis is performed directly by providing the desired wave form of current and collecting the output from facets.

2.3.2 Validation of Laser Solver

To validate the in-house built laser solver, a numerical simulation is performed using the same parameter set as in [93] and the results are compared to the published ones. The parameters used can be found in Table 2-1. The LI curves are displayed in Figure 2-6, carrier density and photon density distributions at the bias current of 60mA are compared in Figure 2-7 (a) and (b), respectively. The large signal optical wave forms with a non-return-to-zero input signal are shown in Figure 2-8 with a modulation speed of 0.5GHz. All the calculated results from the laser solver show excellent agreement with the published results.

Table 2-1
Parameters in Ref [93]

Symbol	Physical Meaning	Values
Λ	Bragg grating period (nm)	244.5
w	active region width (μm)	2
d	active region thickness (μm)	0.15
L	total cavity length (μm)	300
Γ	optical confinement factor	0.3
n_{eff}^0	effective index without injection	3.2
n_g	group index	3.6
α_L	internal loss (cm^{-1})	50
α_H	linewidth enhancement factor	4
g_N	differential gain for bulk ($10^{-16}cm^2$)	2.5
N_{tr}	transparent carrier density ($10^{18}cm^{-3}$)	1.0
ϵ	nonlinear gain saturation coefficient ($10^{-17}cm^3$)	6
τ_c	carrier lifetime ($10^{-9}s$)	1

$r_{1,2}$	facet reflectivity	0.0, 0.0

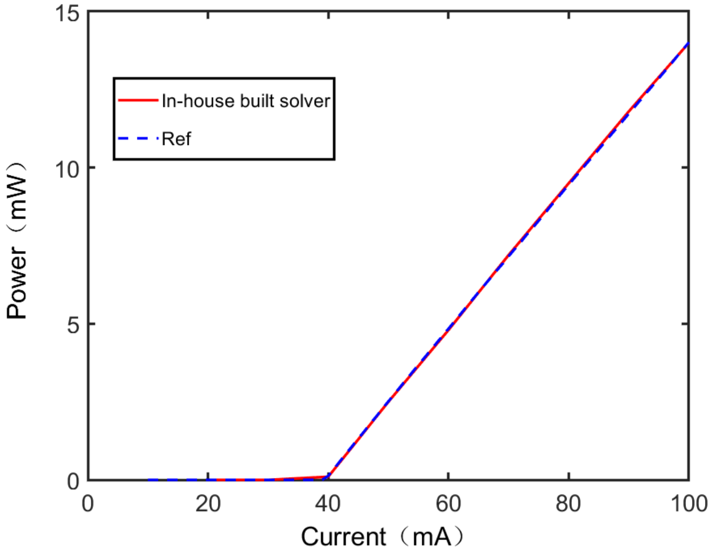

Figure 2-6 LI curve.

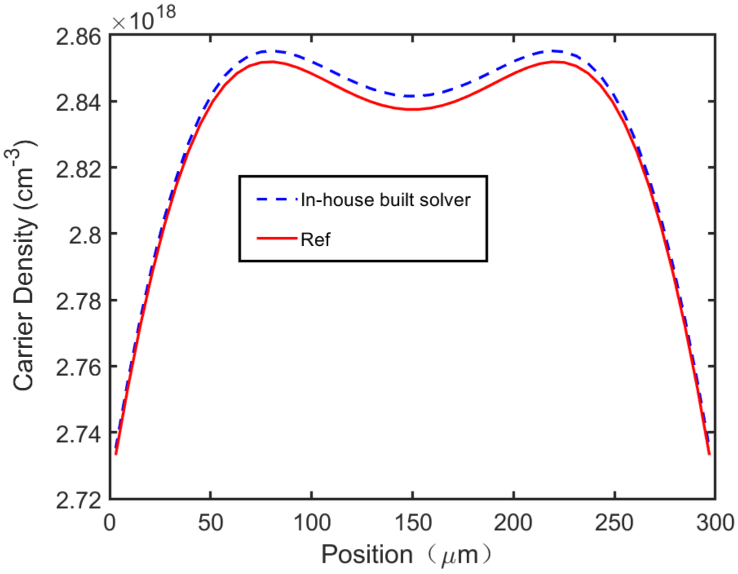

(a)

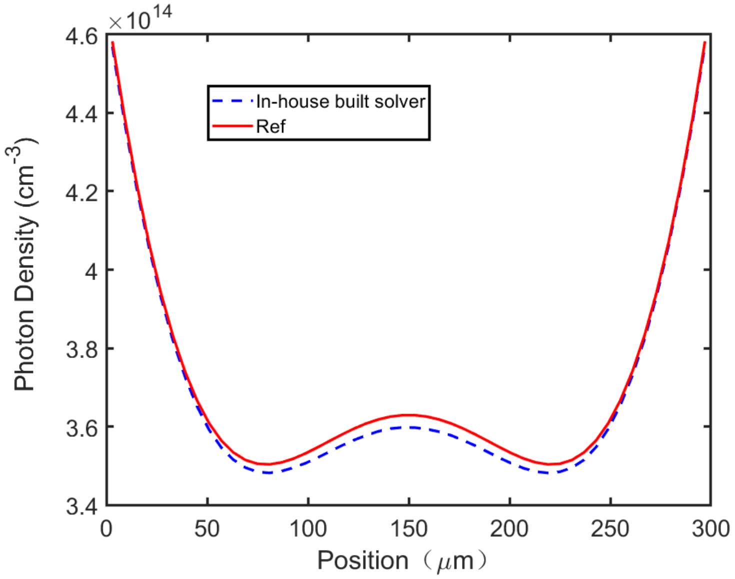

(b)

Figure 2-7 (a) Carrier density and (b) photon density distribution.

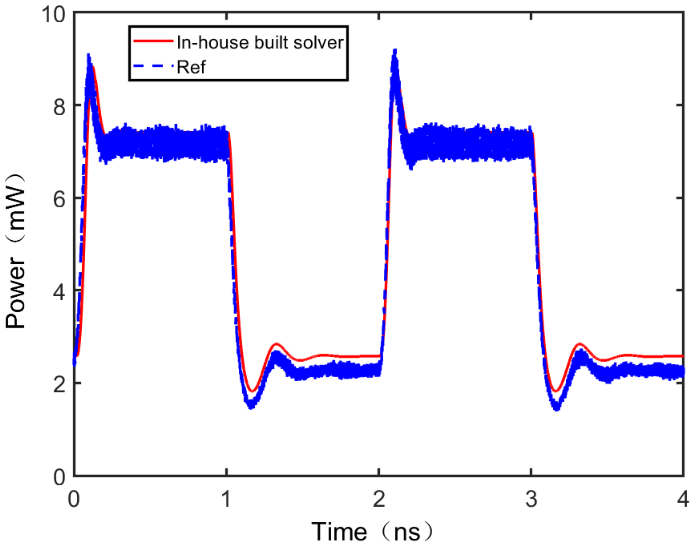

Figure 2-8 Large signal optical wave form.

2.4 Summary

In this chapter, numerical models of semiconductor DFB laser with different complexities are briefly described, followed by the detailed governing equations for (1) optical waves, (2) carriers, (3) heat, and (4) optical gains. The 1D TD TWM is also explained together with the effective parameter extraction and the fitting of the calculated stimulated emission gain to the empirical logarithm model. The split-step method is also discussed as the solution technique for the coupled wave equations. The TWM is then implemented and validated with published results and will be used as the main numerical tool for the investigation of different structures in the following chapters.

Chapter 3 Design of Directly Frequency-Modulated DFB Laser

3.1 Structure and Working Principle

The proposed 3-sectional DFL in this chapter is designed to increase the frequency modulation efficiency and to minimise the residual IM as well. The basic idea behind the DFL is established on the fact that a DFB laser with a uniform grating has its lasing mode on either side of the Bragg stopband, whereas a DFB laser with a $\lambda/4$ phase-shifted grating has its lasing mode at the center of the Bragg stopband. The only difference of these two structures lies in their different grating center phase shifts, which indicates that if the center phase of the grating continuously varies from 0 to π and from π to 2π, the lasing mode will move from one side of the Bragg stopband to the center, and then from the center to the other side accordingly. Since the lasing mode (frequency) follows the change of the grating center phase shift, we can, therefore, change the lasing frequency by introducing a modulation current in the grating center, as the local current injection will alter the material refractive index and consequently induce a local grating phase shift.

The DFL structure is schematically illustrated in Figure 3-1. It has the same structure as the conventional DFB laser except for the split top electrode. While the electrodes on the two side sections are electronically connected for the DC current bias (I_b), the isolated center electrode is set for the modulation current (I_m). In operation, the carrier density in the center section varies with the modulation current (I_m), which yields a local effective index change due to the carrier induced material refractive index change effect. An equivalent phase shift will then be introduced in the grating center and consequently the lasing frequency will change with the modulation current. The proposed DFL has a RW structure based on InGaAsP/InP system with its detailed layer design shown in Table 3-1.

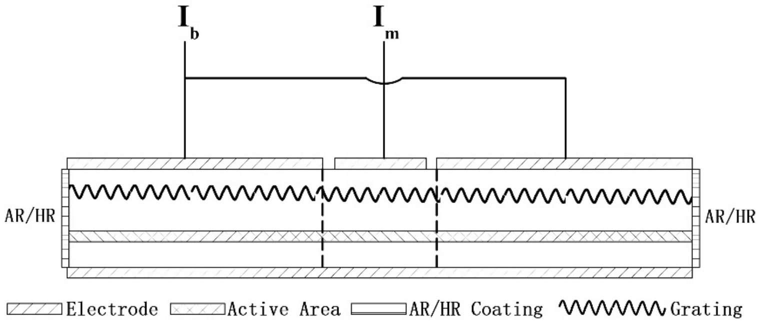

Figure 3-1 Schematic illustration of the DFL structure.

Table 3-1
Layer Structure for DFL

Layer	**Thickness (nm)**	**Composition of In(1-x)GaxAsyP(1-y) (x,y)**	**λ_g(nm)**
Cap InGaAs	200	(0.468,1.000)	1654
P-InP	1800	(0.000,0.000)	918.6
Etching stop	10	(0.108,0.236)	1050
Spacer InP	100	(0.000,0.000)	918.6
Grating layer	varied for different κ	(0.280,0.606)	1300
Spacer InP	10	(0.000,0.000)	918.6
GRINSCH	50	(0.145,0.317) to (0.216,0.469)	1100-1200
Barrier	10	(0.255,0.553)	1260
Well×10	5	(0.189,0.778)	1591
Barrier×10	10	(0.255,0.553)	1260
GRINSCH	100	(0.216,0.469) to (0.145,0.317)	1200-1100
Buffer N-InP	500	(0.000,0.000)	918.6
Substrate N-InP	-	(0.000,0.000)	918.6

Figure 3-2 shows how the aforementioned mechanism works in the DFL with a cavity length of 300μm and a normalized coupling coefficient of 2.8. Other parameters can be found in Table 3-2. Figure 3-2 (a) is the lasing wavelength detuning $\Delta\lambda$ (from the Bragg wavelength) as a function of the phase shift in grating center. The wavelength detuning is obtained by searching for the root with the lowest threshold gain from the eigen equation that describes the longitudinal cavity structure [81], [96]. It's clear that the lasing wavelength moves continuously from the red edge of the Bragg stopband to the stopband center (i.e., the Bragg wavelength), and then from the stopband center to the blue edge, as the grating center phase shift decreases from 0 to -π and then from -π to -2π. Figure 3-2 (b) shows the grating phase shift as a function of effective index change Δn in the grating center. The effective index change Δn is linked to the phase change $\Delta\phi$ by $(\Delta n L_2)/\lambda_B = \Delta\phi/2\pi$. Apparently, for a practically achievable Δn, we can always obtain a required phase shift by choosing the length of the phase shift section (L_2) long enough. Figure 3-2 (c) shows the dependence between the effective index change Δn and the injected carrier density. By exploiting a Bragg wavelength detuning towards the red side of the material gain peak, an enhanced linewidth enhancement factor [97] is obtainable, as shown in the inset of Figure 3-2 (c). With such a design (i.e., by setting the grating Bragg wavelength > active region material gain peak wavelength), we can optimize the efficiency of the effective index change Δn with the injected carrier density.

From the results presented in Figure 3-2, it is clear that the lasing frequency of the DFL can be tuned continuously within its stopband by varying the injected carrier density in the phase shift section located at the center of the grating. The injected carrier density in the phase shift section is determined by the external modulation current (I_m) applied, as well as the local optical field intensity. It can only be obtained by searching for a self-consistent solution of the carrier rate equation and the optical wave equation as described in Chapter 2. The simulation results of the entire device structure from the self-consistent laser solver are shown in section 3.4.

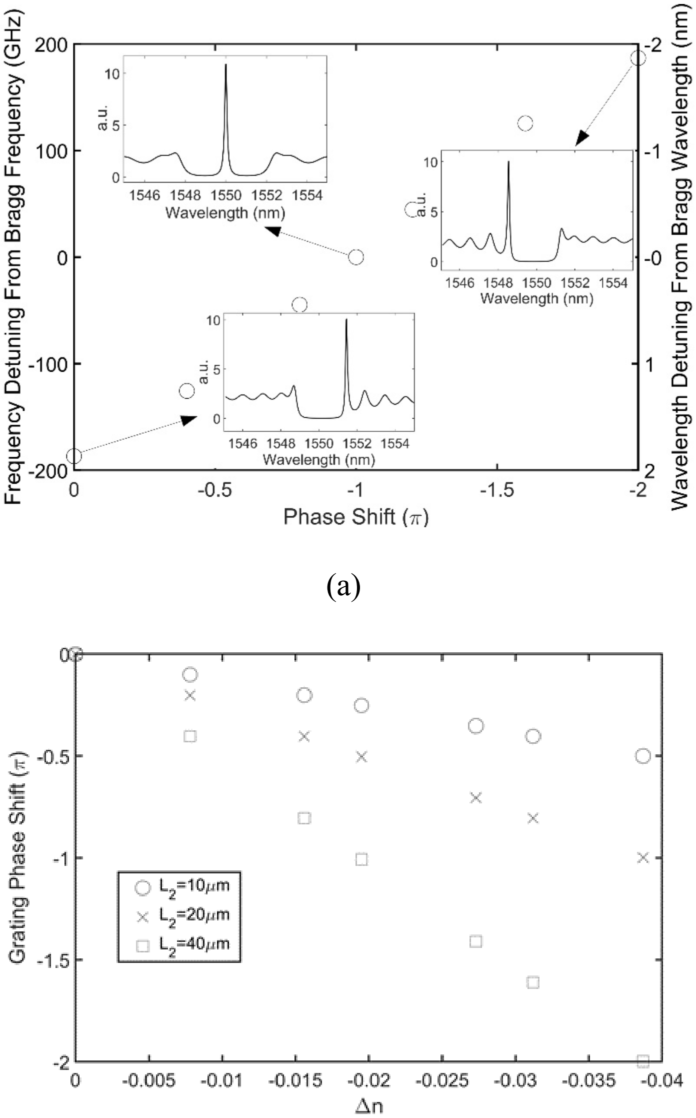

(a)

(b)

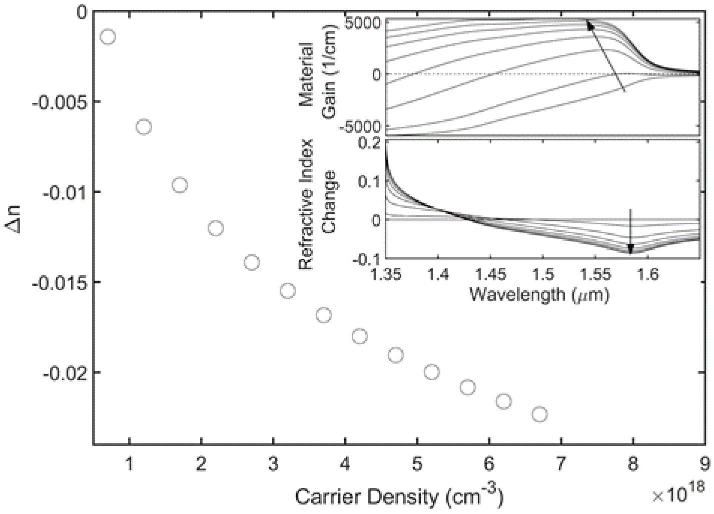

(c)

Figure 3-2 (a) Wavelength (frequency) detuning from the Bragg wavelength (frequency) as a function of the phase shift in grating center. (The cavity length is 300μm, the normalized coupling coefficient κL=2.8, both facet reflectivities are set to zero.) (b) Grating phase shift as a function of the effective index change Δn in the grating center. (Different markers are for different center lengths.) (c) Effective index change Δn as a function of the injected carrier density. (The inset shows material gain and material index change profiles. Different curves correspond to different injected carrier densities varying from 0.7×10^{18}cm^{-3} to 7×10^{18}cm^{-3}.)

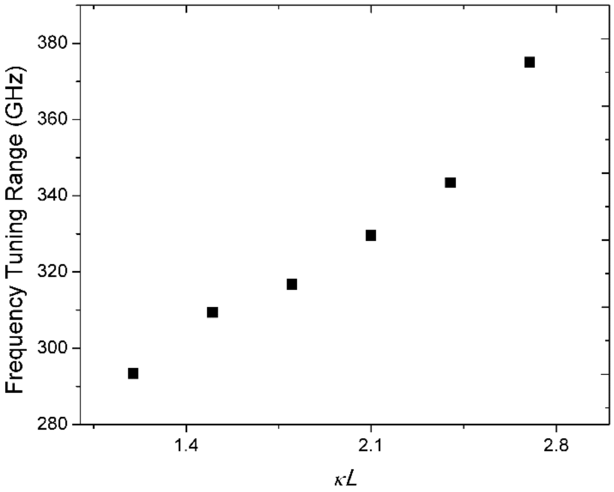

Figure 3-3 Dependence of the lasing frequency tuning range on the normalized coupling coefficient κL.

Figure 3-3 further shows the dependence of the lasing frequency tuning range on the normalized coupling coefficient κL. It is evident that a larger κL supports a wider frequency tuning range, which is not surprising as a larger κL generates a broader stopband, leading to a wider frequency tuning range.

3.2 Gain Elimination with QWI

With the parameters summarized in Table 3-2, the proposed DFL structure shown in Figure 3-1 is simulated by the in-house built laser solver. Figure 3-4 (a) and (b) show the injected carrier density in the phase shift section and the lasing frequency tuning of the DFL as functions of the modulation current I_m, respectively. As I_m increases, the carrier density increases as well, which introduces an effective index change and consequently a grating phase shift according to Figure 3-2 (b) and (c). A lasing frequency tuning therefore appears as the result of the grating phase shift. By comparing the result in Figure 3-2 (a) extracted from the threshold analysis with that in Figure 3-4 (b) obtained from the self-consistent model, however, we find a huge discrepancy on the lasing frequency tuning behavior and tuning range. In contrary to the prediction drawn from our simple threshold analysis, where the lasing frequency shows a continuous and monotonic increase with the injected carrier density (or the bias current), the actual lasing frequency decreases with the bias current regardless the lasing mode is at the red (longer wavelength) or blue (shorter wavelength) side of the Bragg stopband.

Table 3-2
Parameters in DFL Simulation

Symbol	**Physical Meaning**	**Values**
Λ	Bragg grating period (nm)	242.2
w	active region width (μm)	2
d	active region thickness (μm)	0.05
L	total cavity length (μm)	150~400
L_2	phase shift section length (μm)	20~60
Γ	optical confinement factor	0.08
n_{eff}^{0}	effective index without injection	3.2
n_g	group index	3.6
α_L	internal loss (cm^{-1})	10,13*
α_H	linewidth enhancement factor	3,2.82*
g_N	differential gain (cm^{-1})	2500,80*
N_{tr}	transparent carrier density ($10^{18}cm^{-3}$)	0.6,0.8*
ϵ	nonlinear gain saturation coefficient ($10^{-17}cm^{3}$)	3
τ_c	carrier lifetime ($10^{-9}s$)	0.1,0.1*~0.01*
n_{sp}	inversion factor	1.7
γ	spontaneous emission coupling coefficient	1×10^{-4}
$r_{1,2}$	facet reflectivities	0.0, 0.0

*: values used in the phase shift section.

The unexpected behavior can actually be explained by the accompanying change of the effective index in the DC biased sections (shown in the inset of Figure 3-4 (b)) aside the center phase shift section. As we raise the injected carrier density in the center phase shift section by increasing the bias current, the local material gain will be raised as well, as shown in Figure 3-5 (a). The increased gain in the center section will raise the photon density along the entire cavity as shown in Figure 3-5 (b). The carrier density in the side sections will be depleted as shown in Figure 3-5 (c), although a constant current I_b has been applied to these sections. According to Figure 3-2 (c), the reduced carrier density in these sections will induce a relative effective index increase, and will consequently cause a shift of the entire Bragg stopband towards the longer wavelength (lower frequency) side following the well-known Bragg wavelength dependence on the effective index ($\lambda_B = 2n_{eff}\Lambda$, with λ_B defined as the Bragg wavelength, n_{eff} the effective index, and Λ the grating period, respectively). This frequency shift is always opposite to the attempted tuning direction hence the two effects: the lasing frequency (blue) tuning (due to the grating center phase shift) and the overall Bragg stopband (red) shift (due to the effective index increase in side sections), cancel each other. Since the side sections have an overall length much longer than the center phase shift section, the latter effect offsets the former hence the lasing frequency start to tune along the opposite direction from the beginning or after the injection going beyond a critical point: 10mA as shown in Figure 3-4 (b) in this example. Since this cancellation reduces the lasing frequency tuning range as well as the modulation efficiency, we will then have to eliminate this unwanted effect.

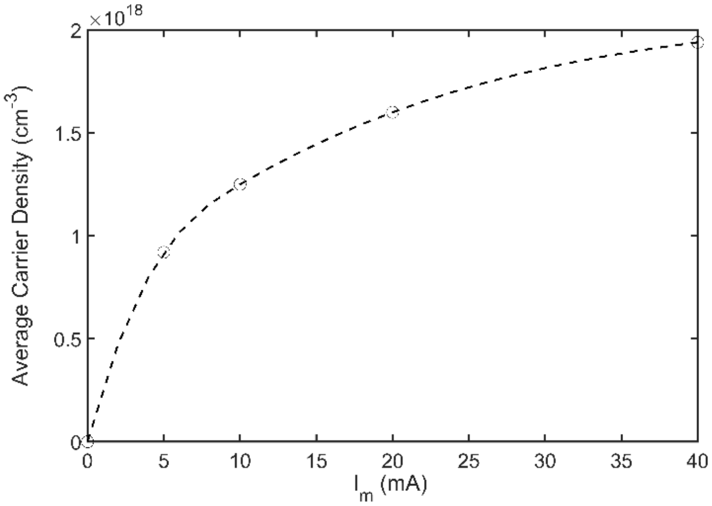

(a)

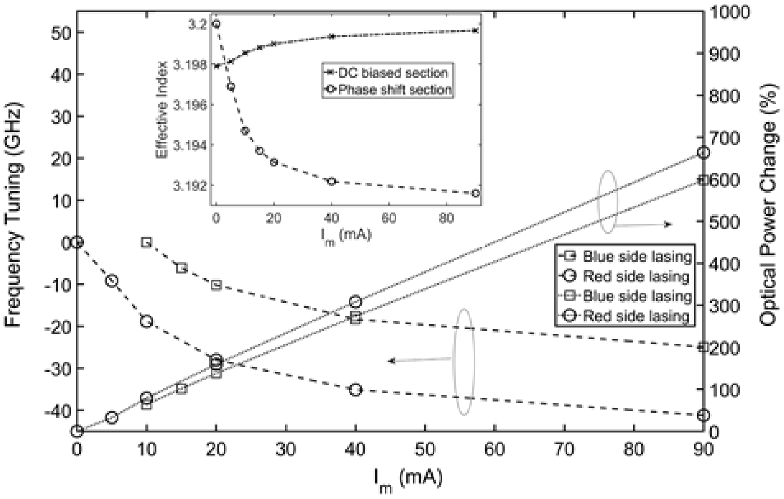

(b)

Figure 3-4 (a) Average injected carrier density in the phase shift section as a function of I_m. (b) Lasing frequency tuning and optical power change as functions of I_m. (The inset shows the average effective index of DC biased section and the phase shift section as a function of I_m, respectively.)

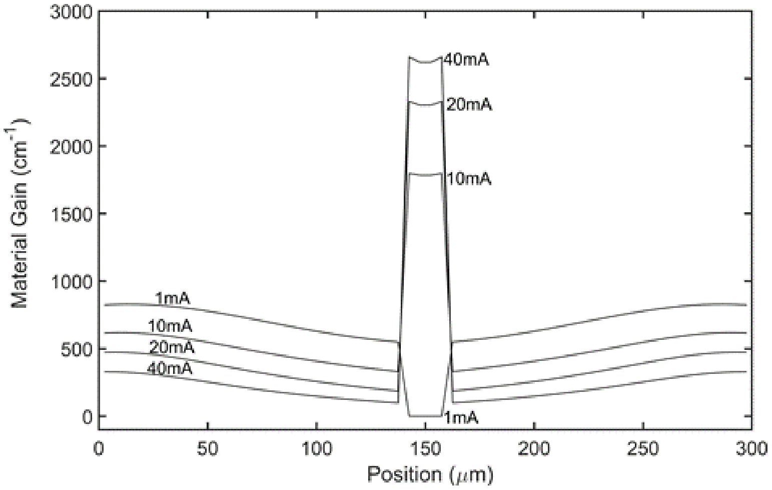

(a)

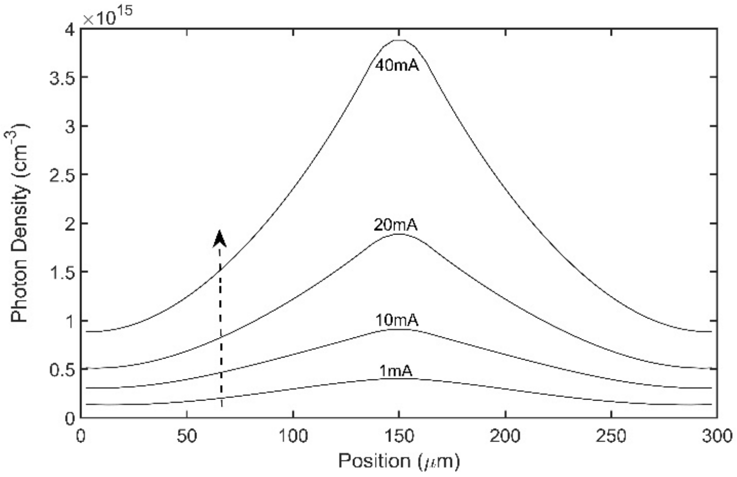

(b)

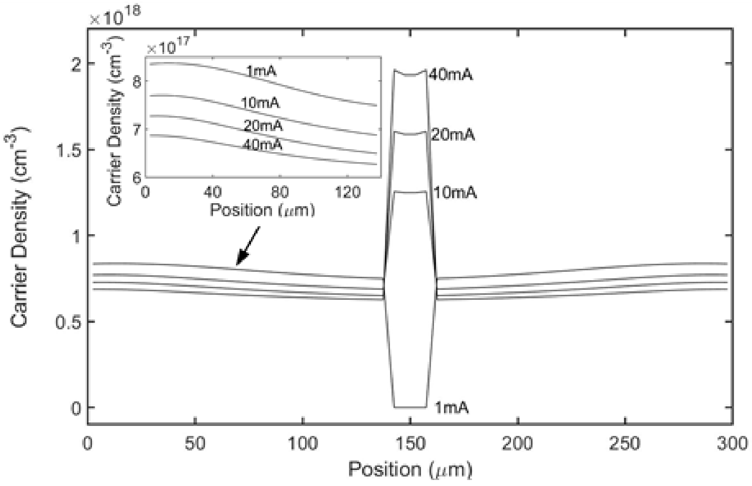

(c)

Figure 3-5 (a) Material gain distribution along the laser cavity under different I_m. (b) Photon density distribution along the laser cavity under different I_m. (c) Carrier density distribution along the laser cavity under different I_m. (The inset shows the magnified local carrier density distribution from 0μm to 140μm.)

Apparently, if we can reduce the local material gain in the center phase shift section caused by the modulation current I_m, the photon density in the side sections will not increase substantially. Hence the carrier density won't be heavily depleted, and the Bragg stopband won't have any significant shift. As a result, the cancellation on lasing frequency tuning will be minimized. Several approaches can be exploited for this purpose by turning the center phase shift section transparent or lossy through, e.g., quantum well intermixing (QWI) [98], [99], or Zn-diffusion into quantum well [100], or selective area growth [101], [102], or butt-joint regrowth [103], [104] of different barrier-well structure. Not only the suppression of the gain in the center phase shift section will enlarge the lasing frequency tuning range and enhance the modulation efficiency, but the parasitic optical power modulation will also be reduced, due to the damped photon density fluctuation in side-sections.

To find the impact of gain reduction on the refractive index change in the phase shift section, we have calculated the material gain and the index change spectra before and after a bandgap (blue) shift introduced by the QWI technique [105]. For the structure shown in Table 3-1 with a shift of 80nm, the result is shown in Figure 3-6. While the active region becomes almost transparent (with negligibly small gain/loss variation under different carrier injection levels) in the vicinity of 1550nm (i.e., the lasing wavelength determined by the grating), the refractive index change, however, only suffers a reduction of 6%. Therefore, it is possible to make the phase section transparent by reducing the gain but maintaining an almost unaffected refractive index change.

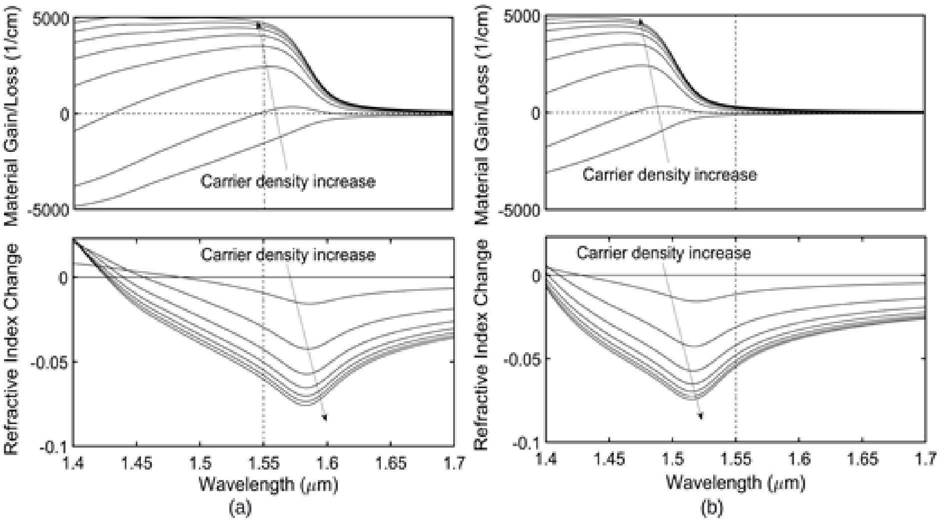

Figure 3-6 Calculated gain and index change profiles for InGaAsP/InP quantum wells (a) before intermixing; (b) after intermixing.

3.3 Performance Simulation and Results

To study the frequency tuning ability of the DFL after gain elimination, the DFL with transparent center phase shift section is simulated again incorporating the QWI effect in a self-consistent manner. The material parameters in the phase shift section are now replaced by those extracted from the gain profile, which is obtained from the post-QWI structure. Extracted parameters can be found in Table 3-2. As shown in Figure 3-7 (a), the unwanted tuning cancellation disappears, and the lasing frequency indeed increases in a continuous and monotonic fashion with the bias current. The output optical power change is shown in Figure 3-7 (b), which clearly proves that the parasitic power change with the bias current is almost negligible (less than 2%) for $\lambda/4$ phase-shifted grating while it's about 17% for the uniform grating structure.

Also as shown in Figure 3-7 (a), with a built-in $\lambda/4$ phase shift in the center, the lasing frequency tuning range is about 1.6 times broader as compared to its uniform grating (with zero built-in phase shift) counterpart. As shown in the inset of Figure 3-7 (b), the averaged index change in the phase shift section is almost identical for both structures. Hence the extra tuning range is due mainly to the high optical field concentration in the cavity center (as shown in the inset of Figure 3-7 (a)), rather than a larger index change in its phase shift section. This can be understood that, as the reduction of the optical gain, the local optical field will have little effect on the carrier density in the phase shift section since the latter will no longer be depleted by the former in a transparent region. As such, the carrier density in the phase shift section will be mainly determined by the injected current, so will the index change. The high optical field concentration in the center of the $\lambda/4$ phase-shifted grating ensures that more photons will experience the effective index change in the center phase shift section. This enhances the lasing frequency modulation efficiency defined as the slope of the curve in Figure 3-7 (a), and consequently expands the tuning range.

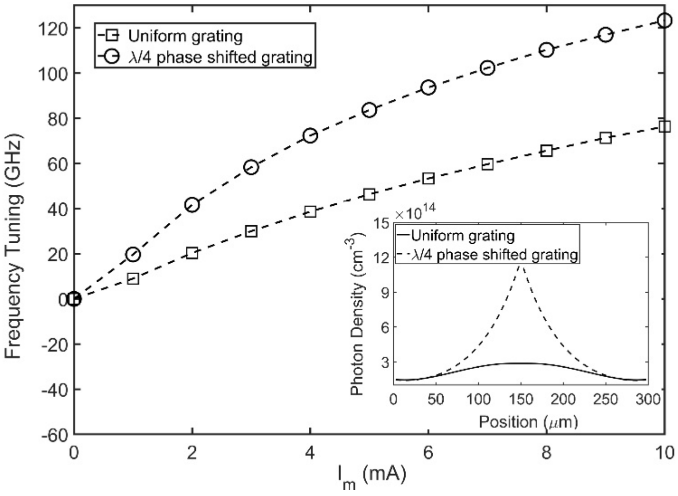

(a)

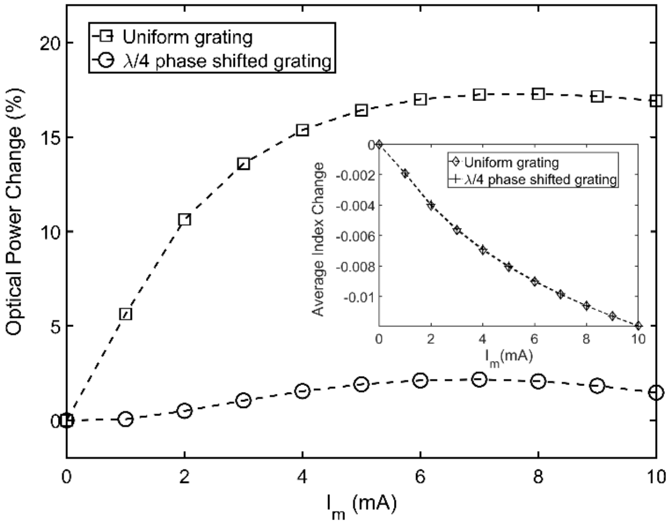

(b)

Figure 3-7 (a) Lasing frequency tuning as a function of I_m in DFL with the uniform and λ/4 phase-shifted grating, respectively. (The inset shows the photon density distribution inside the DFL cavity with the uniform and λ/4 phase-shifted grating, respectively.) (b) Optical power change as a function of I_m in DFL with the uniform and $\lambda/4$ phase-shifted grating, respectively. (The inset shows the average index changes of the phase shift sections under different I_m for two different gratings.)

Figure 3-8 gives the result of the lasing frequency tuning and parasitic optical power change as functions of the modulation current I_m for different combinations of (κ,L). For a same cavity length L, higher grating coupling coefficient κ is preferred for raising the lasing frequency tuning range; for a same κ, however, shorter L is preferred, as shown in Figure 3-8 (a) and (b), respectively. For a DFL with a fixed normalized coupling coefficient κL, we may conclude that a higher grating coupling coefficient κ and shorter cavity length L combination will expand the lasing frequency tuning range. Since the grating Bragg stopband is wider with a combination of higher κ and shorter L for a fixed κL as shown in Figure 3-8 (c), the lasing frequency tuning range will become broader, as the lasing frequency takes a continuous change inside the Bragg stopband with the phase shift in the grating center, following the aforementioned DFL working mechanism. Figure 3-9 shows the lasing frequency tuning and parasitic optical power change as functions of the modulation current I_m for different phase shift section lengths, where the total cavity length is fixed at 300μm.

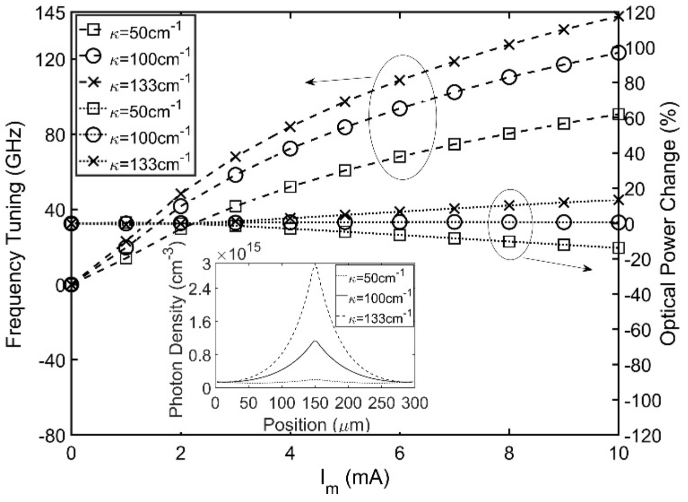

(a)

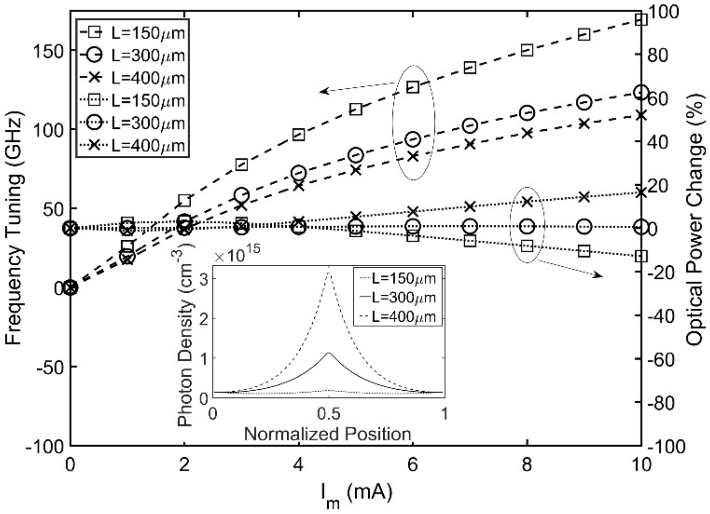

(b)

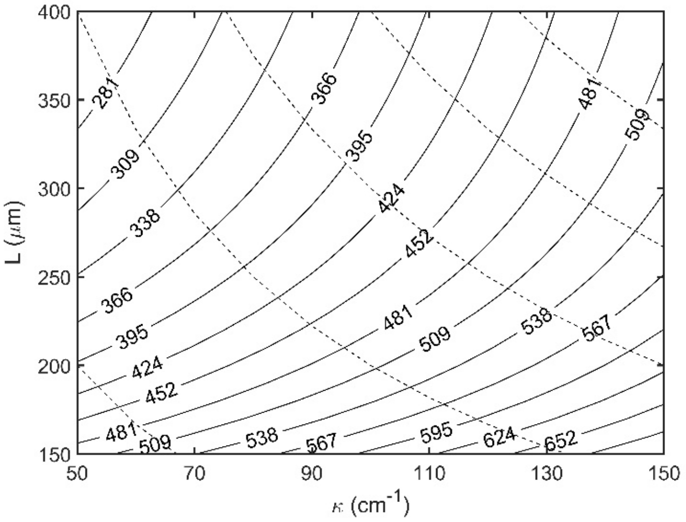

(c)

Figure 3-8 (a) Lasing frequency tuning and optical power change as functions of I_m for different values of the grating coupling coefficient κ, with a fixed cavity length L of 300μm. (b) Lasing frequency tuning and optical power change as functions of I_m for different values of the cavity length L, with a fixed grating coupling coefficient κ at 100cm^{-1}. The phase shift section length L_2 is fixed at 20μm in both cases. (c) The grating Bragg stopband width in GHz for different combinations of (κ, L), where the dashed lines indicate fixed κL values of 1.0 to 5.0 (from bottom left to top right) with an increment of 1.0.

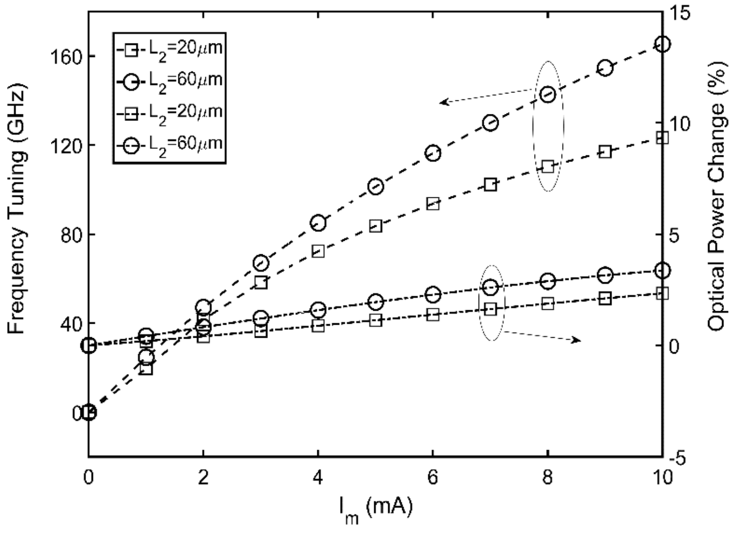

Figure 3-9 Lasing frequency tuning and optical power change as functions of I_m for different values of the phase shift section length L_2, with a fixed cavity length L of 300μm.

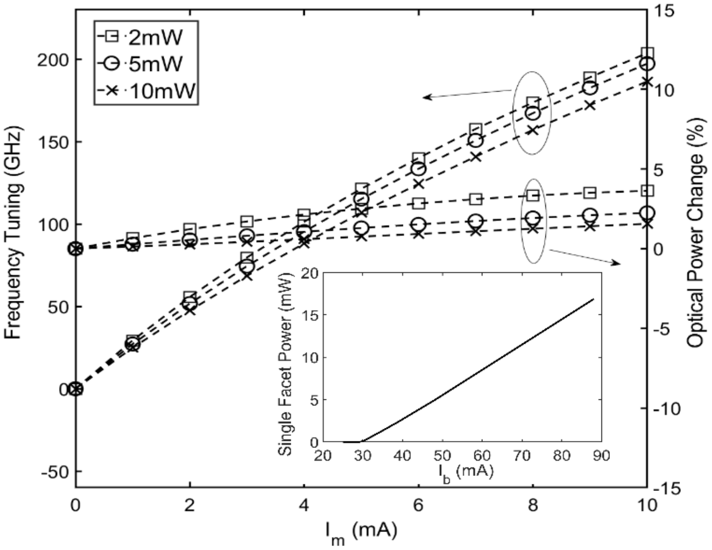

Figure 3-10 Lasing frequency tuning and optical power change of an optimized DFL as functions of the modulation current I_m at different output power levels. (The inset shows the LI curve of the optimized DFL.)

From previous study on parameter dependence of the lasing frequency tuning range, an optimized DFL structure with a $\lambda/4$ phase-shift grating, a cavity length L of 200μm, a phase shift section length L_2 of 60μm, and a normalized coupling coefficient κL of 3 is simulated with the result shown in Figure 3-10. The lasing frequency tuning range is around 200GHz with a modulation efficiency ranged from 26GHz/mA to 17GHz/mA. The relative parasitic optical power change in the full frequency tuning range is less than 4%. The DFL's LI (optical power – DC bias current I_b) curve is also shown in the inset of Figure 3-10. It is worth noting that neither the frequency tuning range nor the modulation efficiency is sensitive to the laser output power, which is different from those reported frequency modulated lasers in the literature [93], [95], [106], as the latter only exploited an indirect approach by enhancing the frequency chirp accompanied with the conventional IM, whereas this design attempted to modulate the lasing frequency directly at any given DC bias current. This feature provides us the convenience to obtain a frequency modulated laser source at any required optical power. The independence between the lasing frequency tuning range (and the modulation efficiency) and the laser output power is due mainly to the reduction of the optical gain in the phase shift section located in the grating center, which makes the lasing and the frequency modulation process decoupled.

Emission spectrum of the DFL at different modulation current I_m is shown in Figure 3-11. It is obvious that all side modes are sufficiently suppressed and there is no mode hopping in the entire tuning range. A scan of the front facet grating phase from 0 to 2π with an increment of π/4 (the rear facet grating phase is kept at 0), assuming a power reflectivity of 0.1% at each facet, is performed. Continuous lasing frequency tuning without mode hopping is verified for different sampled grating phases in the full range. It is worth mentioning though, with increased facet reflectivity, mode hopping in the tuning range may likely happen under different facet grating phase conditions due to the spatial hole burning effect.

Figure 3-12 represents the frequency tuning and optical power change of the proposed DFL with the thermal effect considered. It is clear from the simulation result that the thermal effect has a minor impact on the performance of the DFL, as the frequency tuning range is only reduced by about 5% with an optical power fluctuation increased from 3.6% to 3.9%. This is expectable as the DFL is mainly DC biased. The small modulation current (~10mA) applied to the device brings in no appreciable junction temperature fluctuation hence the thermal induced change on the gain and refractive index are negligible.

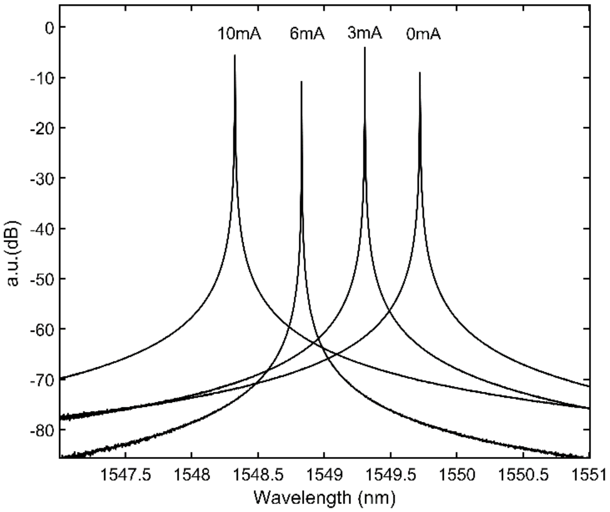

Figure 3-11 Emission spectrum of the DFL at different modulation current I_m with optical power of 2mW.

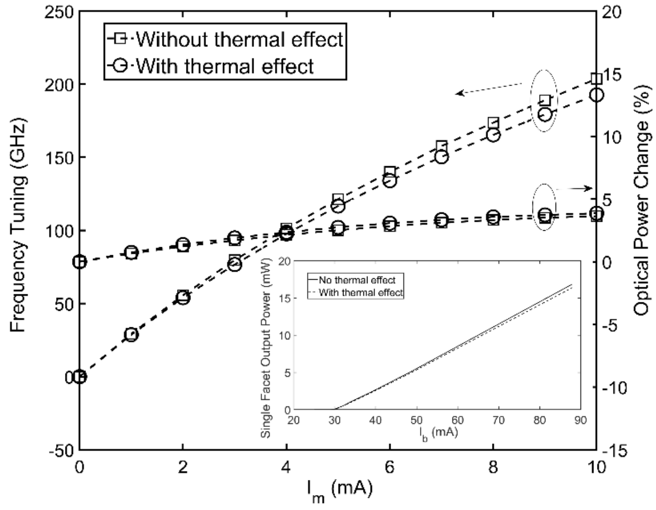

Figure 3-12 Lasing frequency tuning and optical power change as functions of the modulation current I_m with and without the thermal effect. (The inset shows the LI curve of the optimized DFL with and without the thermal effect.)

Figure 3-13 shows the effect of different carrier lifetimes in the phase shift section on the small signal frequency modulation response of the optimized DFL. It is observed that the product of the frequency modulation efficiency (measured by GHz/mA) and the bandwidth does not change with the carrier lifetime, which means we cannot obtain a high modulation efficiency with broad modulation bandwidth simultaneously. To raise the modulation bandwidth, the carrier lifetime in the phase shift section must be reduced [107], [108]. However, following the carrier rate equation [89], the reduction on the carrier lifetime makes the carrier density change in the phase shift section lower for an increment of modulation current ΔI_m, which reduces the phase shift in the grating center and consequently reduces the lasing frequency shift Δf. Hence the frequency modulation efficiency $\Delta f/\Delta I_m$ becomes smaller.

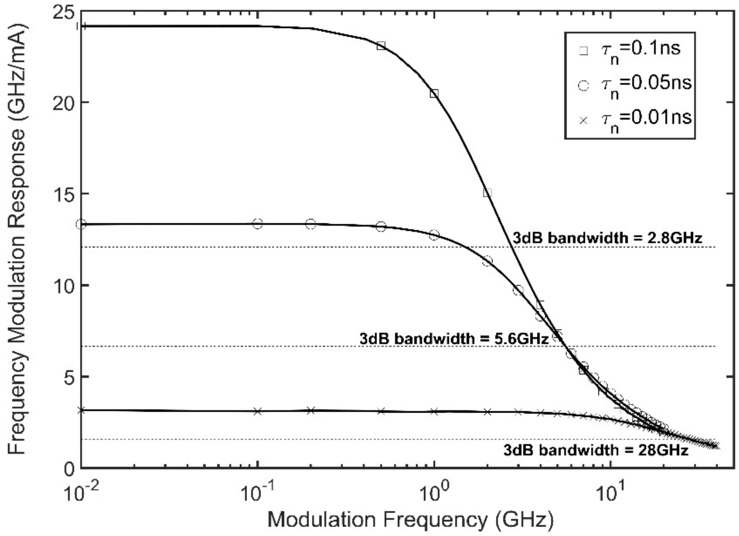

Figure 3-13 The frequency modulation response of the optimized DFL with different carrier lifetimes in the phase shift section. The carrier lifetime in the side sections are still 0.1ns, as listed in Table 3-2.

The proposed DFL can be used to generate optical FM/FSK signals directly. After transmission in optical fiber (or free space), the optical FM/FSK signal can be converted into a conventional IM signal through an optical slope filter and can then be directly detected by a photo detector, as shown in Figure 3-14.

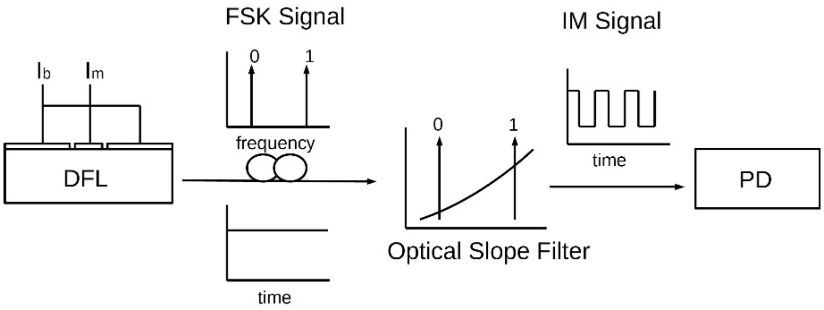

Figure 3-14 Schematic illustration of an optical FSK direct detection (DD) communication system with the DFL used as the light source.

Figure 3-15 gives the numerical simulation result of a back-to-back 25Gbps optical FSK-DD system. The DFL takes the optimized structure with a carrier lifetime of 0.01ns in the phase shift section. The DC bias current is set at 48mA. The modulation current is set between 0mA (for symbol 0) and 34mA (for symbol 1). A frequency shift of 100GHz is obtained under such a modulation current dynamic range. The Bragg wavelength, corresponding to the zero frequency in Figure 3-15 (c), is at 1550nm. The center lasing wavelength (right in the middle of symbol 0 lasing wavelength and symbol 1 lasing wavelength) is at 1549.3nm.

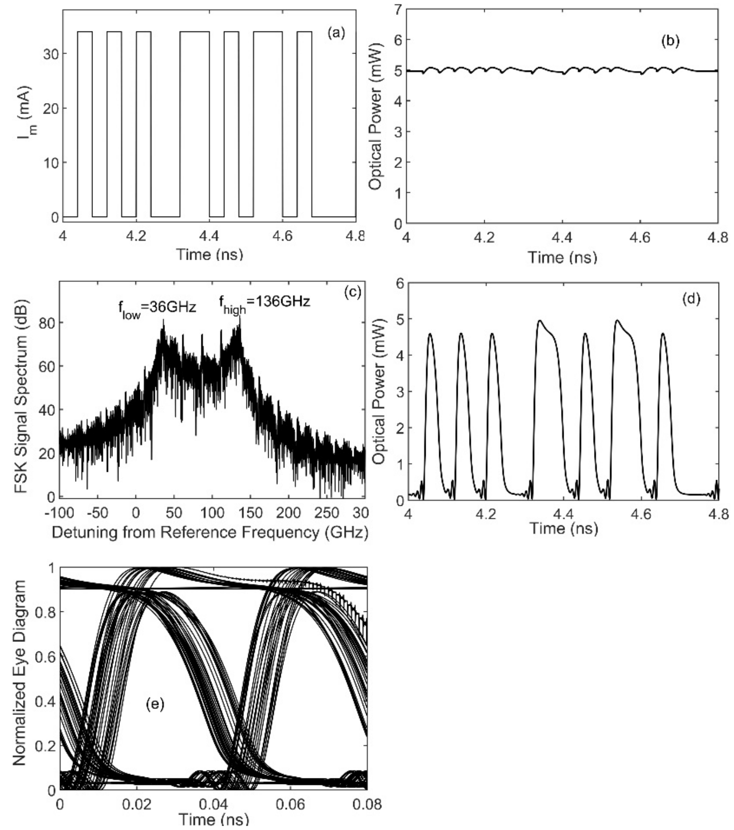

Figure 3-15 (a) The modulation current waveform. (b) The optical FSK signal power waveform. (c) The optical FSK signal power spectrum. (d) The optical IM signal power waveform after FSK to IM conversion by the slope filter. (e) The normalized eye-diagram.

3.4 Summary

We have proposed a DFL structure by utilizing the current induced refractive index tuning of a phase shift section positioned in the grating center. While the main section of the device is DC biased to make the lasing happen, the modulation current is applied to the phase shift section through an isolated electrode. As such, the modulation current changes the phase at the Bragg grating center directly, which consequently changes the lasing frequency. The DFL with optimized parameters can achieve a broad lasing frequency tuning range (~200GHz) with a high modulation efficiency (17~26GHz/mA) as evidenced by our numerical simulation result. A distinguished feature of such designed DFL is its small parasitic power fluctuation. It can also be conveniently DC biased in a broad range to generate the output power at flexible levels as required, without jeopardizing its frequency tuning range and modulation efficiency. As an appealing light source, the DFL can find its applications in various optical systems.

Chapter 4 Design of Direct-Modulated Semiconductor Laser with Asymmetric λ/8 Phase-Shifted Grating

4.1 Reduction of Relaxation Oscillation Peak and Improvement of RIN

In most scenarios, semiconductor lasers are either designed to operate under DC mode, in which high power, wavelength tunability, narrow linewidth, and low RIN can be reached simultaneously, or designed to operate under AC mode with broad modulation bandwidth. However, as the market becomes more demanding, simultaneous optimization of DC and AC performance is required in specific applications [57]. There are conflicts between requirements of structure parameters for optimization of DC and AC performances, e.g., longer cavity length is preferred for better DC performance such as high power and narrow linewidth, however, shorter cavity length is favored for broader modulation bandwidth. Therefore, proper selection of structure with certain compromise is unavoidable.

As mentioned in section 1.2, among all the available structures with wavelength tunability, external cavity lasers, coupled cavity lasers, and Vernier effect based tunable lasers usually suffer from poor performance in direct-modulation bandwidth and the only structure that can balance the DC and AC performance turns out to be the DFB array. The wavelength tunability requirement is relaxed for the individual DFB laser for exchange of broader direct-modulation bandwidth and proper cavity length should be chosen for the trade-off between the bandwidth and linewidth. However, structure optimization is still necessary to mitigate the RIN of the individual DFB laser. Unfortunately, most approaches discussed in section 1.2 are not suitable for the DFB arrays for either the complexity in operation or extra burden in fabrication.

As the main noise source in semiconductor lasers, the spontaneous noise yields fluctuations of both the intensity and phase in the light output [108]. RIN is the characterization of the intensity fluctuation and the spectral linewidth is the characterization of the phase fluctuation. The time dependent output power of a semiconductor laser can be expressed as the summation of the time-independent mean power $\langle P \rangle$ and the time-dependent component $\delta P(t)$

$$P(t) = \langle P \rangle + \delta P(t). \tag{4.1}$$

RIN is then defined as

$$RIN = \frac{\langle \delta P^2(t) \rangle}{\langle P \rangle^2}. \tag{4.2}$$

The RIN of single-mode laser diodes can be derived by considering the well-known rate equation model and expressed as [108]

$$RIN = |H(j\omega)|^2 \frac{\left(1/\tau_c'\right)^2 + \omega^2}{\tau_{p0}\omega_r^4 S_0} 4K_{tot} n_{sp} \Delta f, \tag{4.3}$$

where $H(j\omega_m)$ is the small signal modulation transfer function, ω_r is the relaxation oscillation frequency, S_0 is the photon number inside the cavity, τ_{p0} is the photon lifetime at S_0, n_{sp} is the population inversion factor, K_{tot} is the total spontaneous emission enhancement factor, and τ_c' is the effective carrier lifetime and is given as

$$\frac{1}{\tau_c'} = \frac{1}{\tau_c} + \omega_r^2 \tau_{p0}. \tag{4.4}$$

The linewidth of a single mode semiconductor laser can be given as [108]

$$\Delta v = \frac{K_{tot} n_{sp}}{4\pi \tau_{p0} S_0}(1 + \alpha_H^2), \tag{4.5}$$

with α_H been the linewidth enhancement factor. RIN in (4.3) and linewidth in (4.5) share the common factor of $\frac{K_{tot} n_{sp}}{\tau_{p0} S_0}$, indicating that a high quality factor of the lasing cavity should be kept to enhance the photon lifetime and the total photon number for better device performance.

From (4.3), it is clear that RIN is proportion to the square of small signal modulation transfer function and therefore will have a prominent peak at the relaxation oscillation frequency ω_r as shown in Figure 4-1. To achieve the targeted RIN of less than -150dB/Hz over the 20GHz range, suppression of the peak by introducing a significant damping is therefore the key. The damping to the relaxation oscillation peak can be enhanced by reducing the differential gain or raising the nonlinear gain saturation factor. However, the nonlinear gain saturation factor is mostly material related and can only be slightly raised by reducing the barrier height as well as number of quantum wells (to enhance the homogeneous broadening of the gain spectrum by "locking up" all quantum wells in one). While the former is out of our control, the latter will bring in a poor carrier confinement as a drawback, particularly under high ambient temperature. A reduced differential gain will result in higher threshold current, lower slope efficiency, and what is worse, a reduced direct modulation bandwidth. Since the output power and bandwidth cannot be sacrificed, and we cannot tolerant poor thermal characteristics either as we will rely on heating to tune the lasing wavelength, we must give up the attempt to control these parameters. The damping of the relaxation oscillation can also be introduced by increasing the injected current. However, the level of injection is preserved for the control of light output, therefore not free to manipulate in this case. This leaves us the only other option to introduce the LSHB effect to flatten the relaxation oscillation peak.

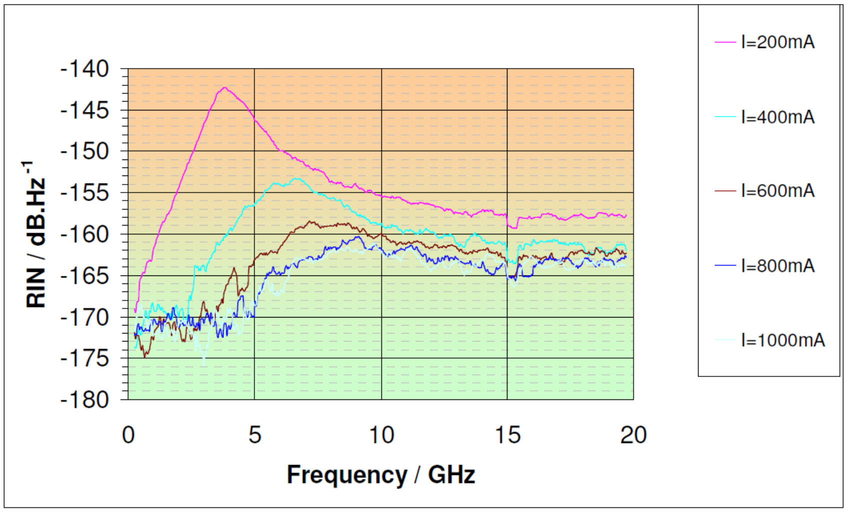

Figure 4-1 Measured RIN in Ref [109].

LSHB is the result of the standing-wave pattern inside the laser cavity and non-uniform distribution of the photon density is introduced by it. It is a common effect especially in edge-emitting semiconductor laser diodes. And because of the anti-correlation between the carrier and photon densities, the carrier density distribution will be non-uniform as well, which will cause the nonuniformity in the distribution of the optical gain and refractive index along the cavity. Generally, severe LSHB effect is detrimental to the operation of DFB lasers and may cause lasing instability [110] and linewidth broadening [111], etc. However, if properly designed, LSHB can also be used to dampen the relaxation oscillation by distributing the energy in the dominant peak over a variety of lower peaks. It can be understood as the non-uniformity along the cavity creates many slightly different small signal modulation transfer functions and the summation of all the functions gives the flattened final curve as shown in Figure 4-2 (a). A comparison of small signal modulation transfer functions of a conventional uniform grating DFB (weaker LSHB) and a conventional λ/4 phase-shifted grating DFB (stronger LSHB) is also given in Figure 4-2 (b) with the parameters summarized in Table 4-1 to show the damping.

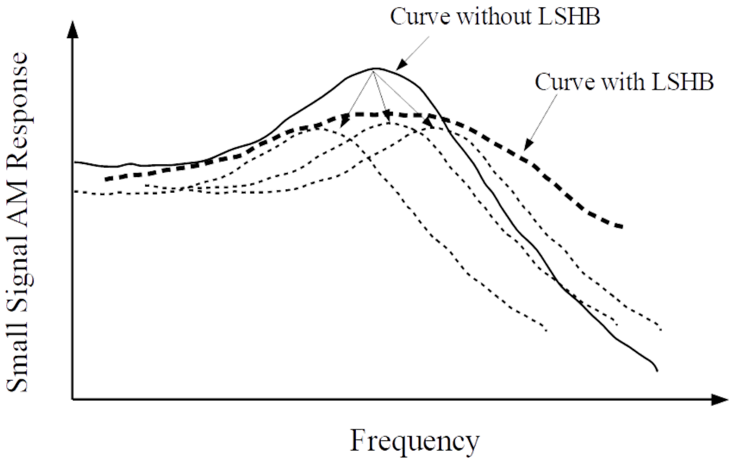

(a)

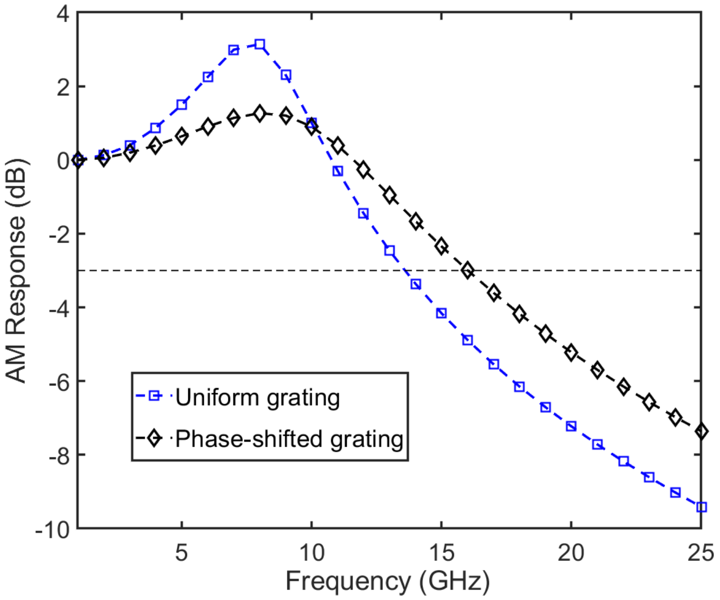

(b)

Figure 4-2(a) Illustration of the flattening of small signal modulation transfer function with LSHB and (b) small signal modulation transfer functions of a conventional uniform grating DFB and a conventional λ/4 phase-shifted grating DFB.

4.2 Asymmetric λ/8 Phase-Shifted Grating

The conventional λ/4 phase-shifted grating DFB has a stronger LSHB effect when compared to uniform grating DFB as the field distribution will have a peak at the position of the grating phase-shift. However, the λ/4 phase-shifted grating DFB is AR-coated on both ends to minimize the effect of the random grating phase at the facets on laser performance. This leads to the waste of half the output power since only one facet can be used to collect the light. With all the aforementioned considerations, an asymmetric λ/8 phase-shifted grating DFB with the rear and front facet HR- and AR-coated is adopted as the basic structure. It can be viewed as a folding of the conventional λ/4 phase-shifted grating DFB about its symmetric center as shown in Figure 4-3. Such a structure takes the advantage of the high quality factor and strong LSHB of the λ/4 phase-shifted grating DFB, yet will not suffer from the power waste issue.

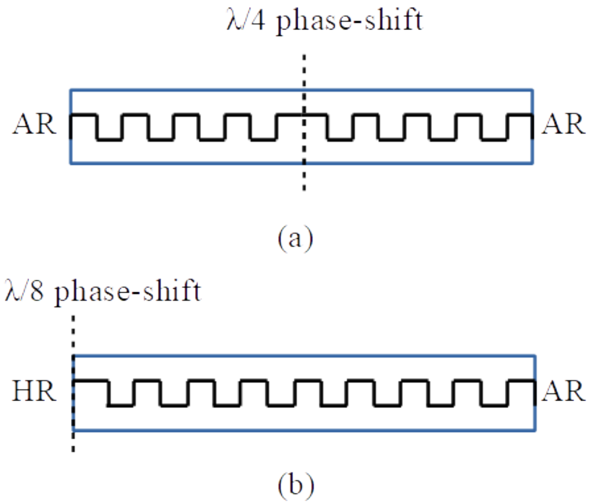

Figure 4-3 Illustration of the (a) conventional λ/4 phase-shifted grating DFB and (b) the asymmetric λ/8 phase-shifted grating DFB.

Table 4-1
Parameters in Laser Simulation

Symbol	Physical Parameter	Value
Λ	Bragg grating period (nm)	243
κ	coupling coefficient (cm^{-1})	50
w	active region width (μm)	2
d	active region thickness (μm)	0.025
Γ	optical confinement factor	3%
n_{eff}	effective index without injection	3.188
n_g	group index	3.6
α_L	internal loss (cm^{-1})	10
α_H	linewidth enhancement factor	1.0
g_N	differential gain (cm^{-1})	1500
N_{tr}	transparent carrier density ($10^{18} cm^{-3}$)	0.8
ϵ	nonlinear gain saturation coefficient ($10^{-17} cm^3$)	3
τ_c	carrier lifetime (ns)	0.7
n_{sp}	population inversion factor	1.7
γ	spontaneous emission coupling coefficient	1×10^{-4}
R_{HR}	rear facet power reflectivity	100% for ideal HR, 90% for real HR
R_{AR}	front facet power reflectivity	0% for ideal AR, 0.1% for real AR
L	cavity length (μm)	400~1000

With the value and position of the grating phase-shift determined, we investigated three different grating profiles for their performance, which includes the uniform grating (UG), the partially corrugated grating (PG), and the apodized grating (AG) as shown in Figure 4-4. With the laser parameters summarized in Table 4-1, numerical simulation is carried out assuming ideal HR (100%) and AR (0%) facet coatings to separate the study of performance dependence on grating profile from the one on facet conditions. The 3dB modulation bandwidth, linewidth, and RIN peak value (defined as the worst RIN value on the spectrum) of the three different designs together with those of a conventional uniform (no phase-shift) DFB laser are listed in Table 4-2 for comparison. The linewidth is calculated with (4.5) and RIN is obtained by first calculating the small signal modulation transfer function then applying (4.3). The normalized filed distribution along the laser cavity is also shown in Figure 4-5 for the four different structures.

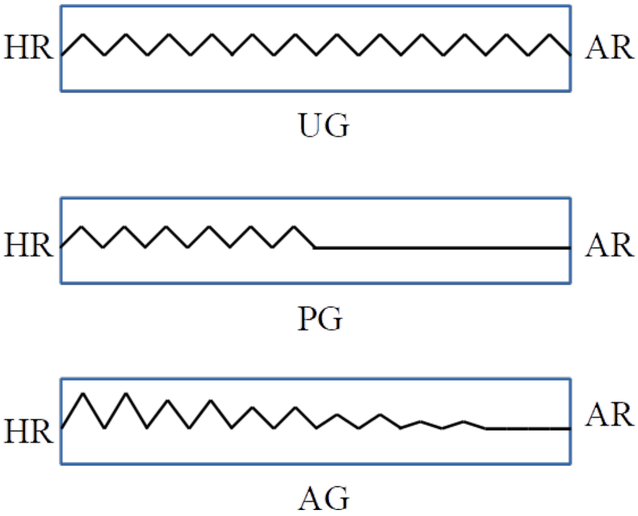

Figure 4-4 Grating profile of the uniform grating (UG), the partially corrugated grating (PG), and the apodized grating (AG).

Table 4-2
Comparison Result for Ideal Facet condition (100% HR and 0% AR)

L=400µm, output power at 20mW	**UG** $\kappa = 50cm^{-1}$	**PG** grating section length = 200µm	**AG** κ linearly varies from 100cm^{-1} to 0	**Conventional Uniform DFB**
f_{3dB} (GHz)	16.5	10	14	16
$\Delta\nu$ (MHz)	0.9	9.8	3.5	1.2
RIN peak value (dB/Hz)	-158	-135	-144	-150

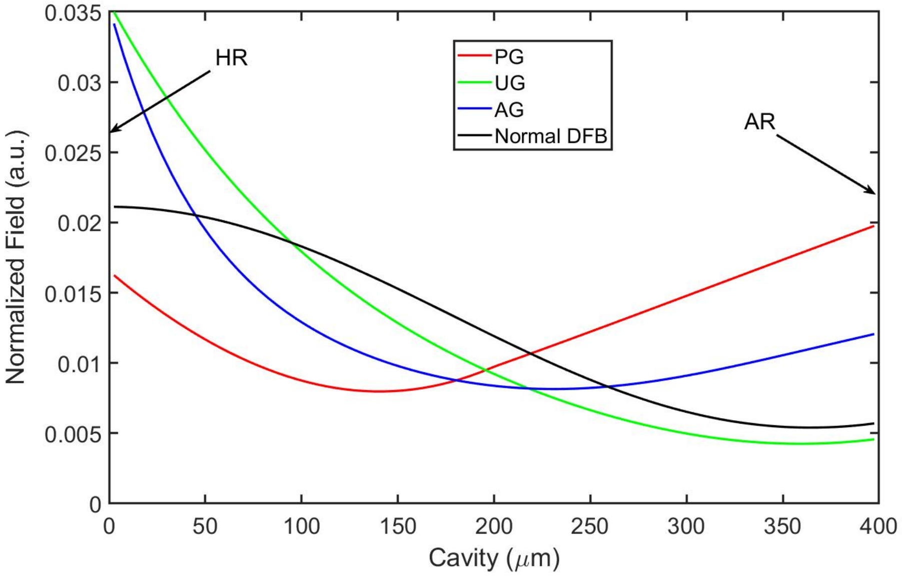

Figure 4-5 Normalized field distribution along laser cavity for UG, PG, AG, and conventional uniform DFB.

It is apparent that the asymmetric λ/8 phase-shifted DFB with uniform grating shows the strongest LSHB effect and highest quality factor (i.e., with weaker field near the AR-coated facet) along with the best performance among the structures investigated. Also, the field distribution in the UG structure is monotonically decaying away from the phase-shift and such a pattern will be preserved regardless of the variation of the grating coupling coefficient κ and the grating length L, which makes it a better choice in terms of fabrication easiness and robustness. For PG and AG structures, although it is possible to improve the performance by adjusting the grating section length or by changing the apodizing profile, the fabrication yield will be an issue as the field distribution in these more complicated structures varies with the cavity design parameters in a non-monotonic manner.

4.3 Performance Simulation and Results

The reflection of the HR-coated facet cannot be 100% in any practical fabrication process and can only reach a power reflectivity of about 90%. Also, the phase-shift cannot be accurately defined at the facet due to the uncertainty in the process of cleaving. Therefore, the position of the phase-shift should be optimized considering the achievable AR and HR reflectivity. Figure 4-6 shows the device performance in terms of the phase-shift position inside the cavity with the position defined as the percentage from the AR-coated facet.

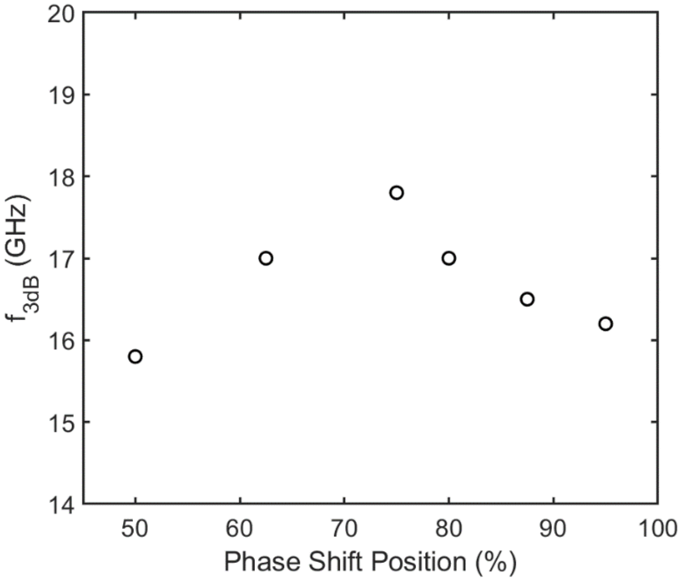

(a)

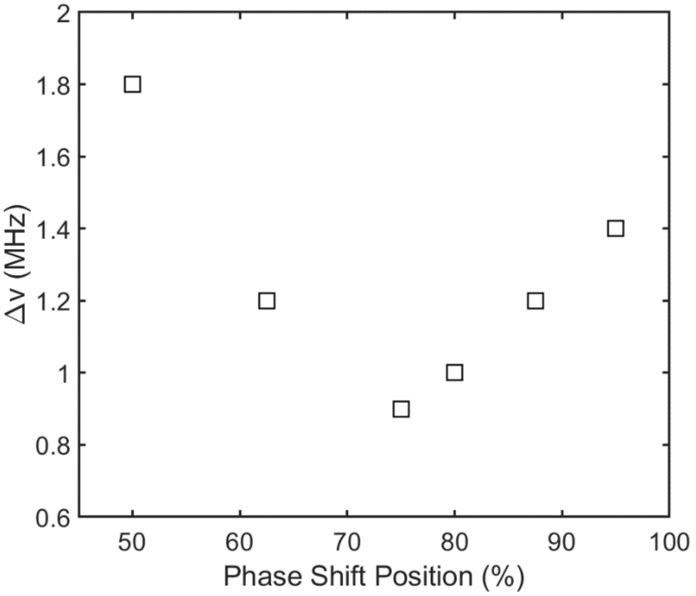
2
1.8
1.6
1.4
1.2
1
0.8
0.6
Δv (MHz)
50
60
70
80
90
100
Phase Shift Position (%)

(b)

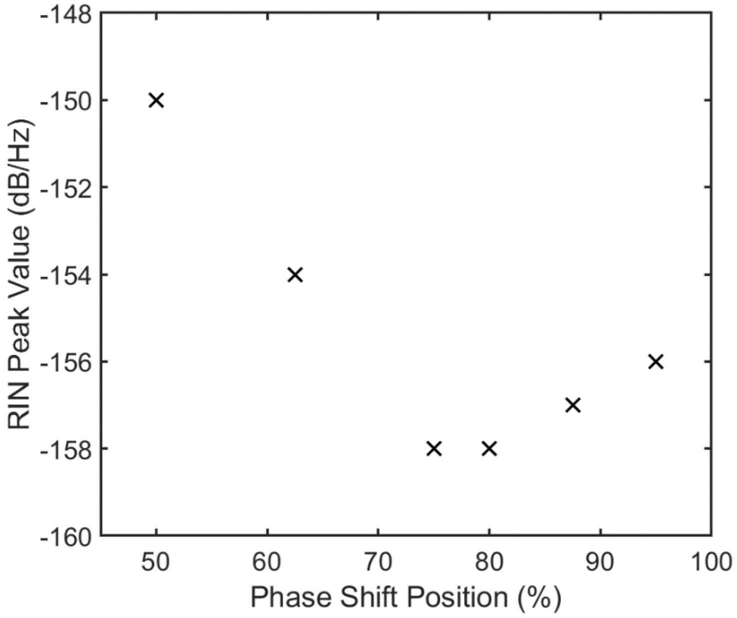
-148
-150
-152
-154
-156
-158
-160
RIN Peak Value (dB/Hz)
50
60
70
80
90
100
Phase Shift Position (%)

(c)

Figure 4-6(a) Modulation bandwidth, (b) linewidth, and (c) RIN peak value as the function of the grating phase-shift position. Power reflectivity of HR- and AR-coated facets are 90% and 0.1%, respectively. Cavity length is 400μm and output power is 20mW.

The numerical simulation results presented in Figure 4-6 suggest that the phase-shift position should be positioned at 75% of the cavity length away from the AR-coated facet (i.e., 25% of the cavity away from the HR-coated facet) with the given power reflectivity at two facets. The reason behind the relatively better performance from this specific phase-shift position is due mainly to the higher quality factor of the cavity. As shown in Figure 4-7, the optical field always has a peak at the phase-shift position and light wave escapes the cavity from both ends because of the non-ideal HR coating. The leaked power is the reason for a reduced quality factor from infinity and as the phase-shift position approaches the AR-coated facet from the HR-coated facet, the power leakage displays a minimum at the position around 75%. The minimum power leakage indicating the highest quality factor therefore the best linewidth and RIN as discussed in section 4.1. The increase of the field at the AR-coated facet is relatively smaller when compared to the counterpart at the HR-coated facet when the phase-shift moves toward them, however, the much lower reflectivity at the former still guarantees a larger increase in power leakage. That is why the device performance experience a more severe deterioration when moving toward the AR-coated facet from the optimized position.

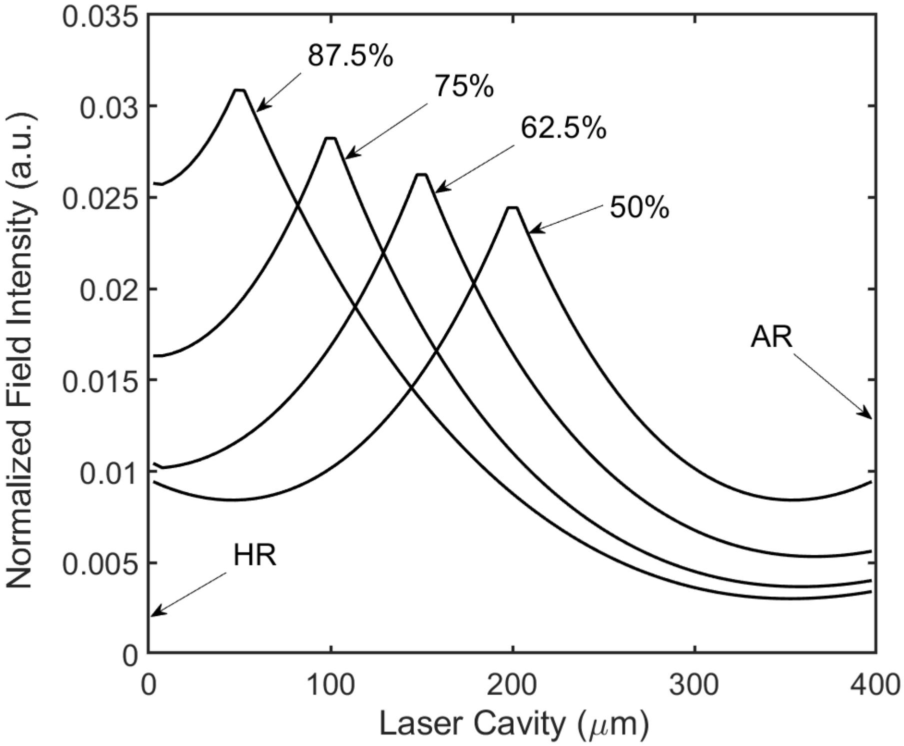

Figure 4-7 Normalized field distribution along laser cavity for different phase-shift positions.

With the phase-shift position optimized, the grating coupling coefficient κ and the cavity length L are investigated. Calculated modulation bandwidth, linewidth, and RIN peak value as functions of the grating coupling coefficient κ, cavity length L, and normalized coupling strength κL are shown in Figure 4-8, 4-9, and 4-10, respectively. While increasing κ or κL will improve both modulation bandwidth and noise characteristics (linewidth and RIN), increasing L can only improve the noise characteristics. Longer L will reduce the modulation bandwidth, but it can raise the output power. Its associated lower thermal resistance will improve thermal dissipation, thus will allow the current injection at a higher level, although the slope efficiency will actually be lower.

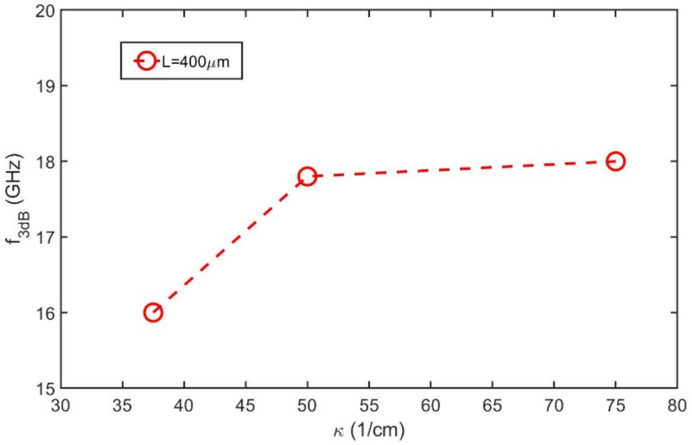
L=400μm
f_{3dB} (GHz)
20
19
18
17
16
15
30
35
40
45
50
55
60
65
70
75
80
κ (1/cm)

(a)

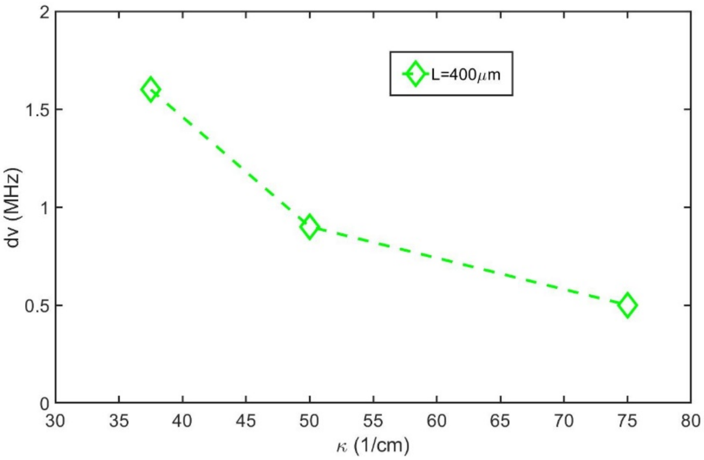
L=400μm
dv (MHz)
2
1.5
1
0.5
0
30
35
40
45
50
55
60
65
70
75
80
κ (1/cm)

(b)

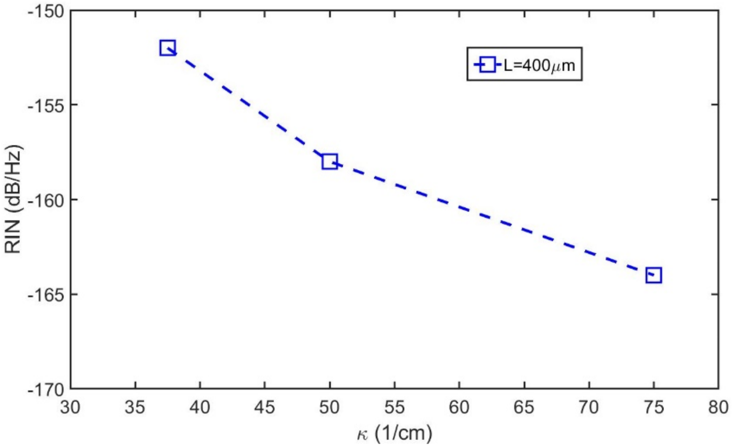

(c)

Figure 4-8(a) Modulation bandwidth, (b) linewidth, and (c) RIN peak value as functions of the grating coupling coefficient κ at 20mW.

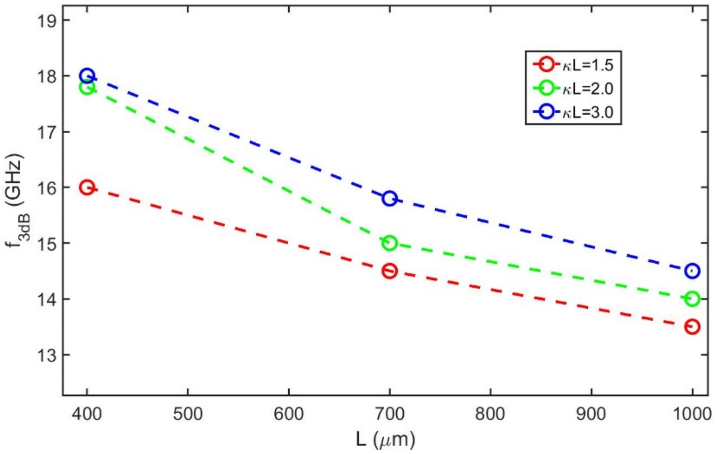

(a)

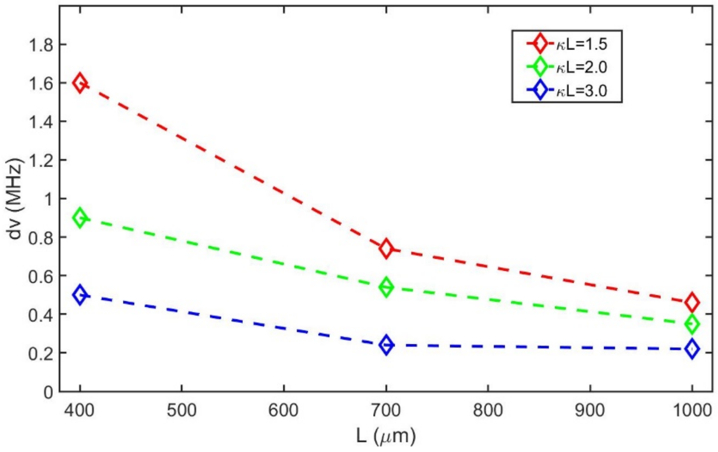

(b)

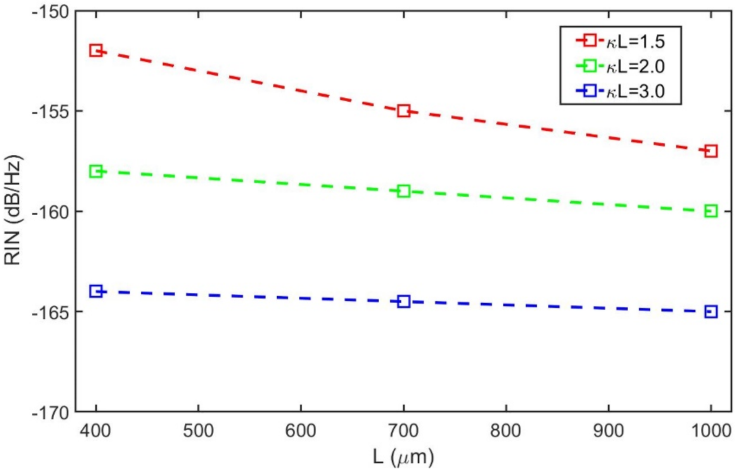

(c)

Figure 4-9(a) Modulation bandwidth, (b) linewidth, and (c) RIN peak value as functions of the cavity length L at 20mW.

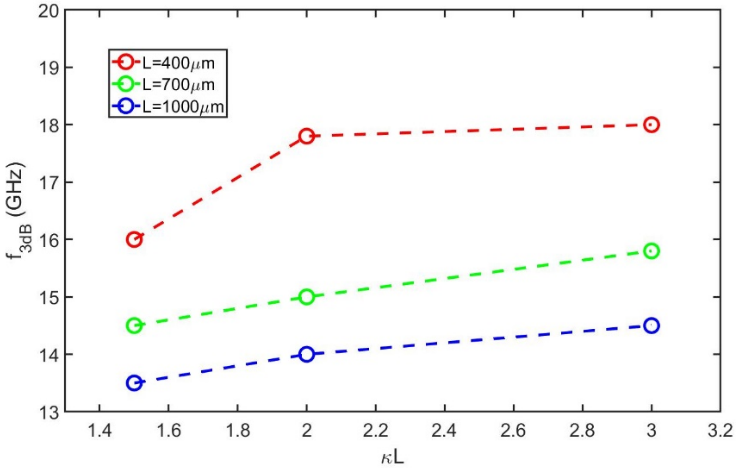
L=400μm
L=700μm
L=1000μm
f_{3dB} (GHz)
20
19
18
17
16
15
14
13
1.4
1.6
1.8
2
2.2
2.4
2.6
2.8
3
3.2
κL

(a)

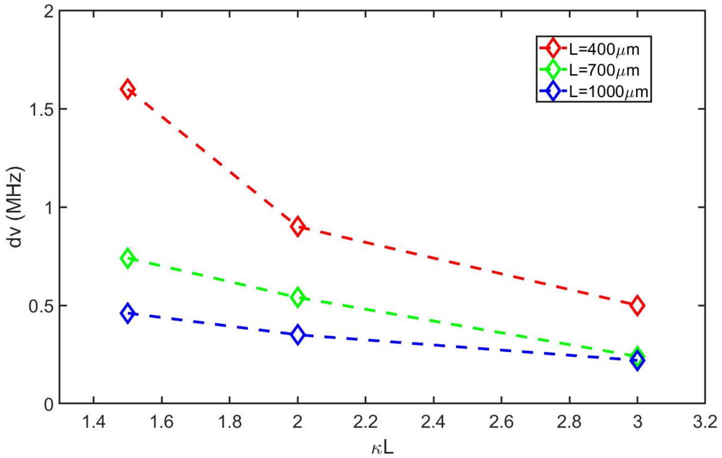
L=400μm
L=700μm
L=1000μm
dv (MHz)
2
1.5
1
0.5
0
1.4
1.6
1.8
2
2.2
2.4
2.6
2.8
3
3.2
κL

(b)

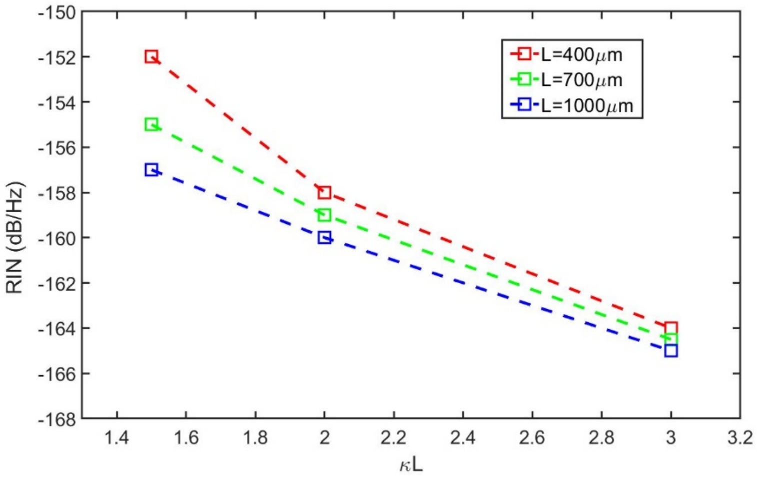

(c)

Figure 4-10(a) Modulation bandwidth, (b) linewidth, and (c) RIN peak value as functions of the normalized coupling strength κL at 20mW.

With all the conclusions made from the simulation results, a normalized grating coupling coefficient κL as high as possible (e.g., 3 as a viable value) is found to be desirable and two different cavity length L (e.g., 400μm and 700μm) are studied for a best combination of the output power and modulation bandwidth from experiment. The calculated LI curve and normalized field distribution are displayed in Figure 4-11 with small signal AM Response and RIN at 20mW displayed in Figure 4-12.

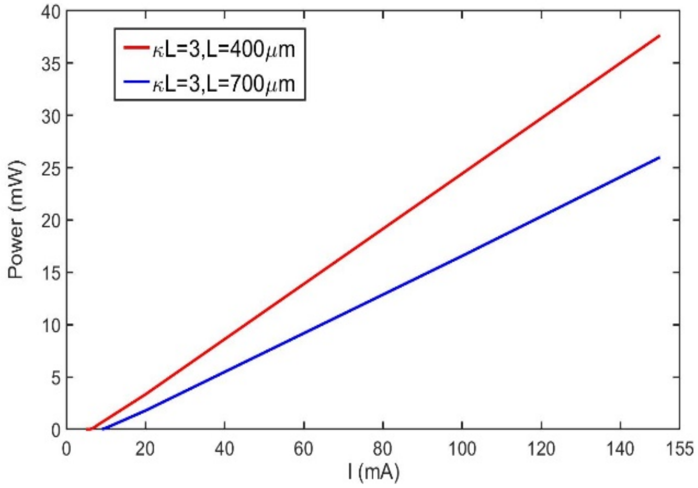

(a)

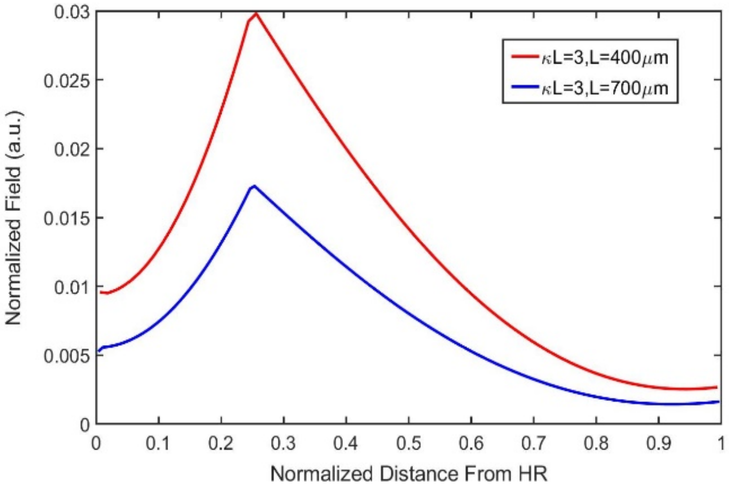

(b)

Figure 4-11(a) LI curve and (b) normalized field distribution at 20mW for the optimized structure.

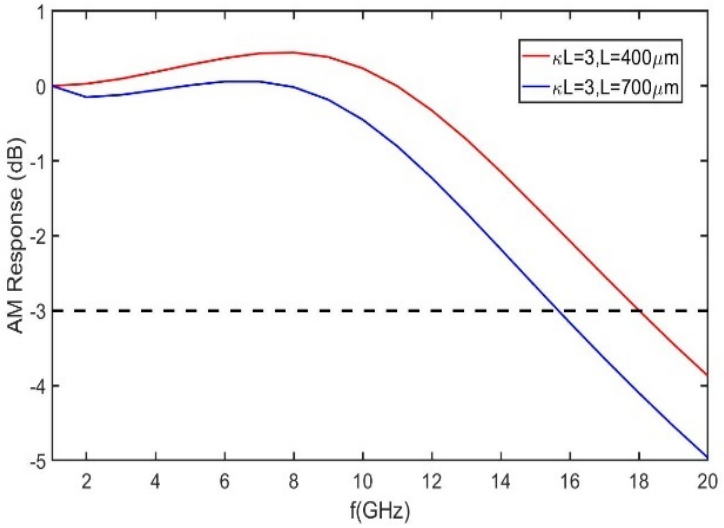

(a)

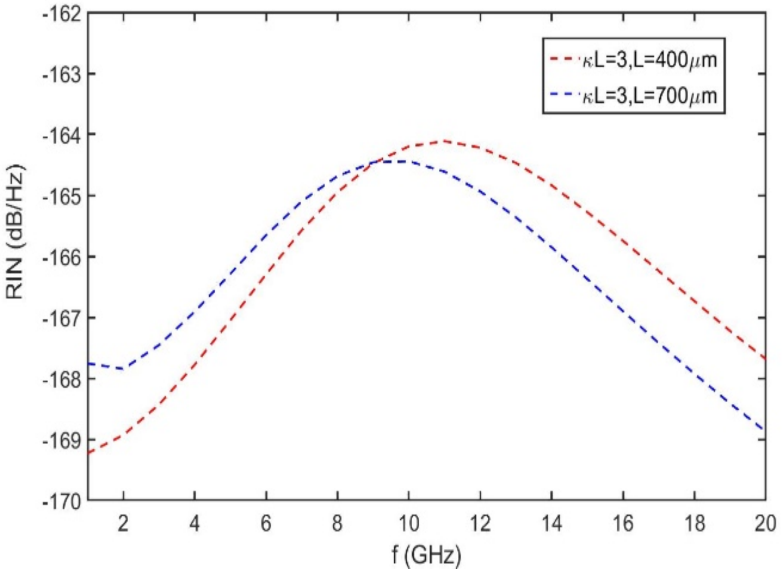

(b)

Figure 4-12(a) Small signal AM Response and (b) RIN at 20mW for the optimized structure.

4.4 Summary

In this chapter, the background and performance specification of a direct-modulated semiconductor laser with wavelength tunability and low noise (narrow linewidth and low RIN) is firstly explained. The link between RIN and the small signal modulation transfer function is then given with the damping of relaxation oscillation by LSHB discussed. Based on that, an asymmetric λ/8 phase-shifted grating DFB laser is proposed to take advantage of the strong LSHB in phase-shifted grating DFB structure to flatten the relaxation oscillation peak and also to avoid the power waste from a conventional λ/4 phase-shifted grating DFB laser. Three different grating profiles are investigated and the UG structure is found to be the best candidate given that the fabrication easiness and robustness have high priority in our consideration. The position of the phase-shift is then optimized considering achievable reflectivity from the HR- and AR-coated facets and the quality factor of the laser cavity is found to be the decisive figure-of-merit behind the optimization. The device performance dependence on grating coupling coefficient, cavity length, and normalized coupling coefficient is investigated with numerical simulation and design guideline is given at last.

Chapter 5 Design of Direct-Modulated Semiconductor Laser with the Periodic Current Blocking Grating

5.1 Comprehensive Rate Equation Model for Small Signal Response

In this chapter, we propose a periodic current blocking grating for improving of the modulation bandwidth of DMLs which requires no extra fabrication steps when compared to a traditional III-V DFB laser. The approach can be applied separately on DMLs or combined with other effects, e.g., PPR or detuned loading, if needed. The proposed approach aims at improving the net differential gain by reducing the differential cavity loss with a specially designed periodic current blocking grating. The net differential gain is the difference between the differential gain and the differential loss. Although the former is difficult to improve with the given constraints on material and strain, however, the net differential gain can still be enhanced by making the differential loss negative, i.e., a reduced loss with increased bias. The total loss for a laser is the sum of the internal loss and cavity loss [108] and the former is fixed under different biases while the latter shows different behaviour for different types of semiconductor lasers. With the proposed grating design, a negative differential loss could be realized in DFB lasers by periodically blocking the current flow in the grating high index region, therefore enhancing the modulation bandwidth.

From the standard behavior model, the AM response of a semiconductor laser is described by the 2nd order low-pass filter transfer function [108]

$$H(\omega) = \frac{1}{\left(j\frac{\omega}{\omega_r}\right)^2 + j\frac{\omega}{\omega_d} + 1}, \tag{5.1}$$

where ω is the modulation frequency of the bias current, ω_r and ω_d are the relaxation oscillation frequency, i.e., CPR frequency, and the damping frequency, respectively and can be expressed as

$$\omega_r = \sqrt{\frac{\Gamma S_0 v_g}{\tau_{p0} V} \frac{\partial g}{\partial N} |_{N_0}}, \tag{5.2a}$$

$$\omega_d = \frac{\omega_r^2}{\frac{K_{tot} n_{sp}}{\tau_{p0} S_0} - \Gamma S_0 v_g \frac{\partial g}{\partial S} |_{S_0} + \frac{1}{\tau_c} + \frac{\Gamma S_0 v_g}{V} \frac{\partial g}{\partial N} |_{N_0}}. \tag{5.2b}$$

Here N_0, S_0, and τ_{p0} are the steady state carrier density, photon number, and the corresponding photon lifetime with a given bias current I_0, respectively. $\frac{\partial g}{\partial N}|_{N_0}$ and $\frac{\partial g}{\partial S}|_{S_0}$ are the differential gain in terms of carrier density and photon number at the steady state (N_0, S_0). The spontaneous term $\frac{K_{tot} n_{sp}}{\tau_{p0} S_0}$ is usually negligible compared to other terms in (5.2b) when the laser is biased above threshold and can be ignored.

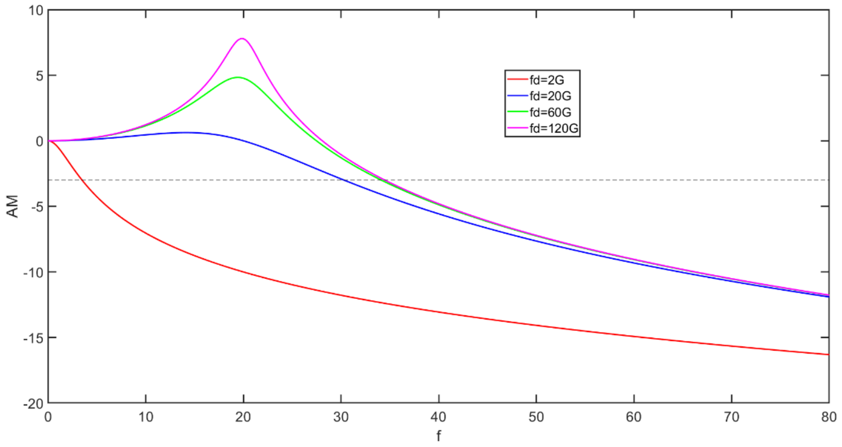

(a)

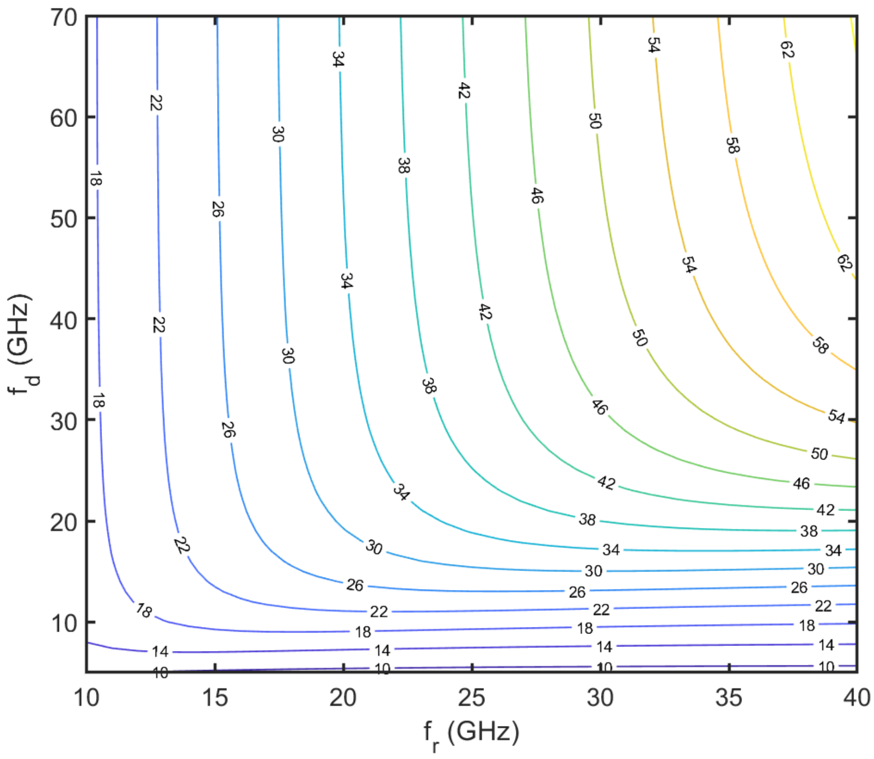

(b)

Figure 5-1 (a) AM response curves for different f_d with fixed f_r of 20GHz. (b) 3dB-bandwidth calculated from (5.1).

Transfer functions in (5.1) with different values of f_d ($2\pi f_d = \omega_d$) are displayed in Figure 5-1 (a) and it is clear that the position of the relaxation oscillation peak is mostly determined by f_r and the height of the peak is governed by the ratio f_r/f_d. To achieve a large modulation bandwidth for DMLs, the 3dB bandwidth calculated from (5.1) should be large enough and the value is determined jointly by f_r and f_d. A contour graph of the 3dB bandwidth is presented in Figure 5-1 (b) and we can find that increasing either f_r or f_d will lead to an extended 3dB bandwidth yet with a saturation effect if the other parameter is fixed. For semiconductor lasers, f_d is generally larger than f_r which indicates a maximum

3dB bandwidth of $f_{3dB} \approx 1.7 f_r$. Therefore, the effort to obtain a large modulation bandwidth should be mostly focused on improving the relaxation oscillation frequency f_r. From (5.2a), it's clear that we could enhance f_r by adopting optimized MQW structure to increase the differential gain and the ratio between Γ and V, biasing the laser with a large current to increase the photon number S_0, and utilizing a cavity with high cavity loss to decrease the photon lifetime τ_{p0}, corresponding to the aforementioned approaches in section 5.1.

It should be noticed that (5.2a) and (5.2b) are derived from the rate equation model with the assumption of constant cavity loss which is not always valid. By lifting the assumption, a more comprehensive description of the relaxation oscillation frequency and damping frequency can be reached as

$$\omega_r = \sqrt{\frac{\Gamma S_0 v_g g_N}{\tau_{p0} V N_0}\left(1 - \frac{1}{\Gamma}\frac{\partial \alpha_c/\partial N}{g_N/N_0}\right)}, \tag{5.3a}$$

$$\omega_d = \frac{v_g g_N \left(1 - \frac{1}{\Gamma}\frac{\partial \alpha_c/\partial N}{g_N/N_0}\right)}{\varepsilon N_0 \left(1 + \frac{\tau_{p0} v_g g_N}{\varepsilon N_0} + \frac{\tau_{p0} V}{\Gamma \tau_c \varepsilon S_0}\right)}\,. \tag{5.3b}$$

Here the logarithmic material gain equation Eq. (A6) is used and the detailed derivation can be found in appendix A. Definition of the other parameters can be found in Table 5-2 and previous chapters. The term $\frac{1}{\Gamma}\frac{\partial \alpha_c/\partial N}{g_N/N_0}$ inside the bracket reflects the effect of a carrier density dependent cavity loss and (5.3) will reduce to the conventional description of (5.2) without this term. As the differential gain coefficient g_N, optical confinement factor Γ, and steady carrier density N_0 are always positive, a negative dependence of cavity loss α_c over carrier density N will provide an enhancement of both the relaxation oscillation frequency and damping frequency which is beneficial for 3dB bandwidth extension.

For FP type laser, the cavity loss given as $\frac{1}{2L}ln(\frac{1}{R_1R_2})$ is basically fixed due to its fixed facet reflectivity R_1 and R_2, which will give a differential cavity loss of zero for any bias condition. While for a DFB type laser, the cavity loss is inversely proportional to the grating coupling strength and is no longer a fixed value, providing us an opportunity to achieve a negative differential cavity loss. Unfortunately, for DFB lasers with conventional grating, the differential cavity loss is actually a small positive value as the grating coupling strength will be reduced with an increased bias together with the inverse correlation between grating coupling strength and cavity loss. This is explained as the high index (small bandgap) material in the grating will experience more index reduction when carriers been injected compared to low index (large bandgap) material [112]. Therefore, when bias being raised, the index difference between high index and low index material of the grating will be lowered and results in a reduced grating coupling strength. Yet a negative differential cavity loss is realizable with the periodic current blocking grating. The special designed grating blocks the current flow in high index grating regions with a p-n-p junction while allowing current flow in the low index grating regions. With such a selective current blocking, the index in the high index regions will be kept almost unchanged when the bias is raised, while the index in low index regions will be reduced as usual. A raised index difference between these two regions will then be created with increased bias and therefore a negative differential cavity loss.

5.2 Structure of the Periodic Current Blocking Grating

Figure 5-2 shows the 3D structure of a sample AlGaInAs/InP DFB laser with the periodic current blocking grating layer locating on the P side, however, the design can also be modified to accommodate a grating on the N side. The grating layer consists of three sub-layers and the detailed structure is displayed in Figure 5-3.

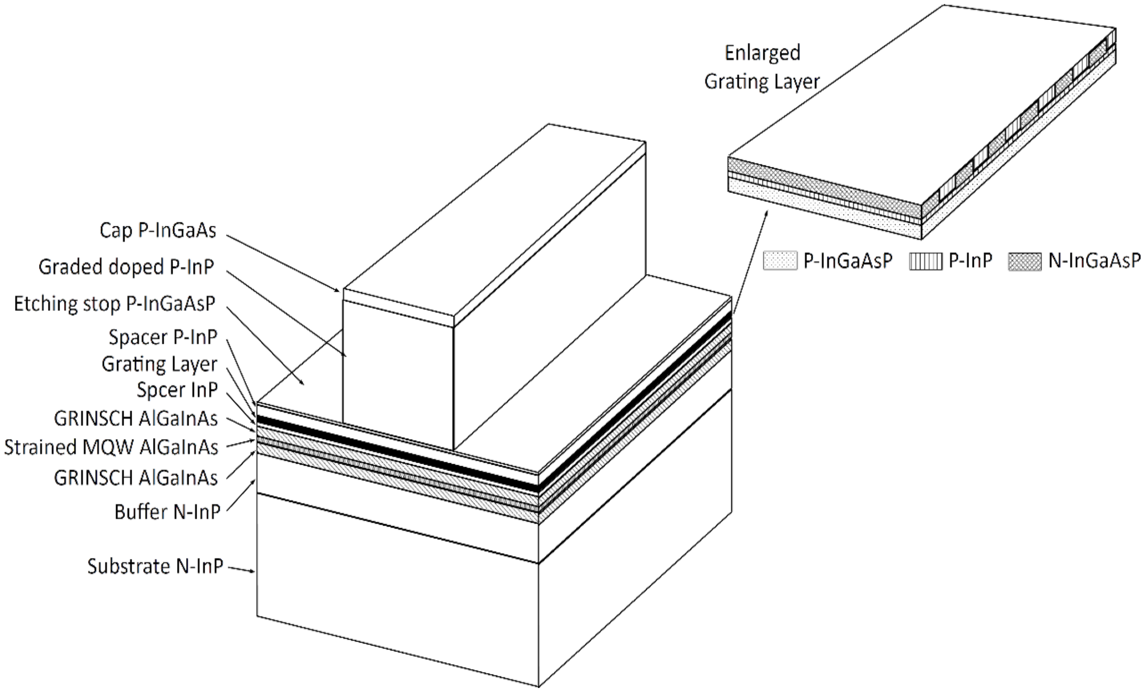

Figure 5-2 3D schematic diagram of the DFB laser.

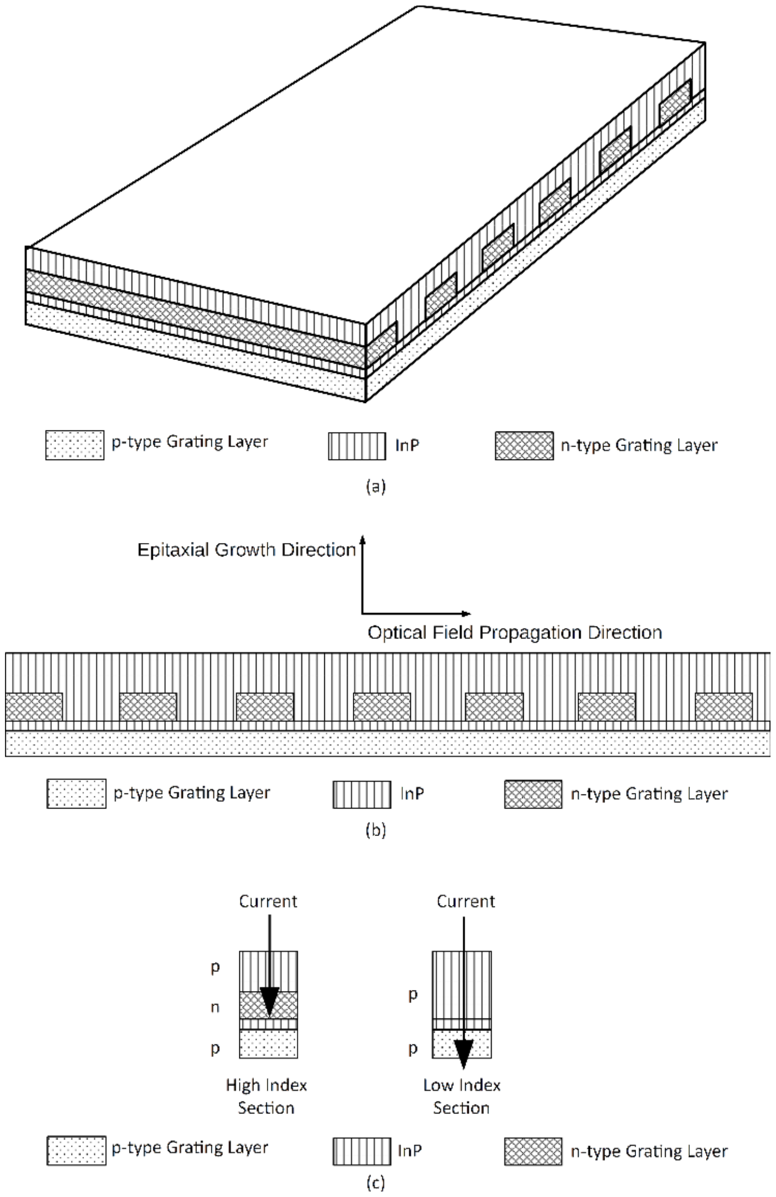

Figure 5-3 (a) 3D schematic diagram of the periodic current blocking grating; (b) Side view of the grating structure; (c) Illustration of the current flow in high index and low index regions.

The three sub-layers are p-type grating layer, InP etching stop layer, and n-type grating layer, following the epitaxial growth order. The side view of the grating in Figure 5-3 (b) shows the structure with the n-type grating layer been periodically removed and the complete structure been buried with low index material, i.e., InP, via standard epitaxy process. Area defined by the remaining n-type grating layer then form the high index regions of the grating and area with n-type grating layer removed from the low index regions. The InP etching stop layer sandwiched between the p- and n-type grating layer is utilized to provide protection for the p-type grating layer when the n-type grating layer been selectively removed.

The periodic current blocking mechanism can be explained with the current flows in high index and low index regions shown in Figure 5-3 (c). When the DFB laser is forward biased, the p-type grating layer and the remaining n-type grating layer form a reverse biased PN junction in the high index regions and blocks the injected current from entering the bottom p-type grating layer. While in the low index regions, the absence of the n-type grating layer allows the current to flow through the p-type grating layer and results in a locally increased carrier density. And due to this increased carrier density, the refractive index of p-type grating layer in low index regions will experience a drop due to the plasma effect [74]. Meanwhile, because of the blocking effect from the reverse biased PN junction, the carrier density in high index region p-type grating layer will remain largely unchanged and so does the refractive index there. As the index difference between the n-type grating layer and InP forms the base index difference of the grating, the index difference will be enhanced when current been injected into this periodic current blocking grating. Therefore, a positive dependence between normalized grating coupling strength κL and carrier density N will be realized, indicating a negative differential cavity loss following the inverse correlation between the cavity loss and normalized grating coupling strength in DFB lasers.

Figure 5-4 shows the dependences between the normalized cavity loss $\alpha_c L$ and the normalized grating coupling strength κL for two different grating structures. Normalized cavity loss of DFB laser is calculated numerically by solving the corresponding eigen equation given the value of κL [94]. In both cases the normalized cavity loss displays a higher decline rate at lower κL range and the phase-shifted grating gives a steeper decline for any κL value. The results indicate that low κL value should always be preferred for the desired 3dB bandwidth enhancement while phase-shifted structure will likely experience a stronger extension effect compared to the uniform one. However, the conventional uniform grating structure generally has a broader base 3dB bandwidth, therefore which structure will exhibit a final better performance will require further investigation.

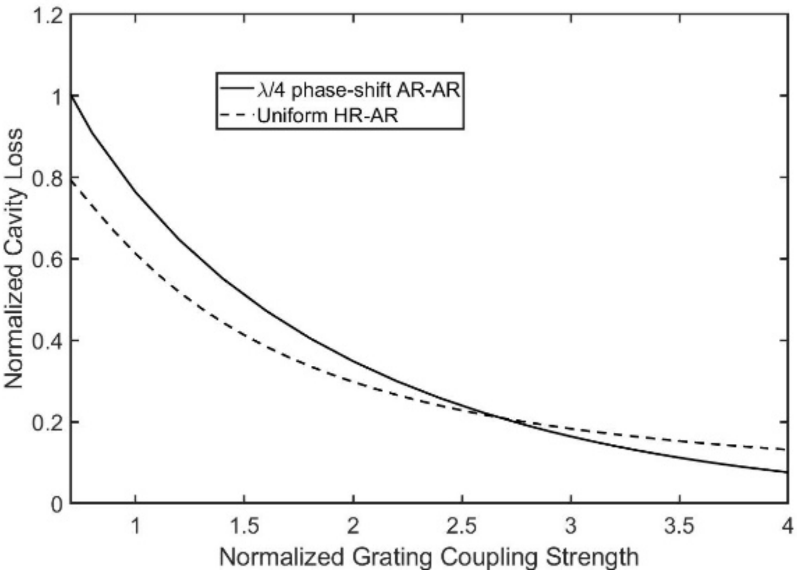

Figure 5-4 Normalized cavity loss of DFB laser as a function of the normalized grating coupling strength.

5.3 Performance Simulation and Results

A 1310nm strained MQW RW DFB laser is adopted to present the 3dB bandwidth enhancement introduced by the periodic current blocking grating through numerical simulation in this section. The 3D graph of the DFB laser is presented in Figure 5-2 and the detailed layer structure is summarized in Table 5-1.

Table 5-1
Layer Structure for the 1310nm DFB Laser

Layer	Thickness (nm)	Composition (x,y)	λ_g(nm)	Index
Cap $In_{1-x}Ga_xAs$	200	(0.466,0.0)	1654	3.5597
P-InP cladding	1600	(0.000,0.000)	918.6	3.2069
$In_{1-x}Ga_xAs_yP_{1-y}$ etching stop	10	(0.144,0.316)	1100	3.3356
InP spacing	100	(0.000,0.000)	918.6	3.2069
$In_{1-x}Ga_xAs_yP_{1-y}$ n-type grating	50	(0.108,0.236)	1050	3.3010
InP etching stop	20	(0.000,0.000)	918.6	3.2069
$In_{1-x}Ga_xAs_yP_{1-y}$ p-type grating	80	(0.216,0.469)	1200	3.4077
InP spacing	30	(0.000,0.000)	918.6	3.2069
$Al_xGa_yIn_{1-x-y}As$ P-GRINSCH	30	(0.47,0.0) - (0.269,0.202)	841-1120	3.2652-3.3761
$Al_xGa_yIn_{1-x-y}As$ Wells×11	5	(0.168,0.127) CS1.2%	1399	3.4199
$Al_xGa_yIn_{1-x-y}As$ Barriers×12	6	(0.251,0.22)	1150	3.3871
$Al_xGa_yIn_{1-x-y}As$ N-GRINSCH	50	(0.269,0.202) - (0.47,0.0)	1120-841	3.3761-3.2652
InP buffer	500	(0.000,0.000)	918.6	3.2069
InP substrate	-	(0.000,0.000)	918.6	3.2069

The numerical investigation of the structure is divided into 3 steps which are:

1. Refractive index change (Δn) is calculated under different carrier densities (N) following the approaches explained in Chapter 2 for the P-type grating layer. Therefore, the dependence between Δn and N is obtained.

2. Field distribution of the optical mode in the low index region is calculated in the 2D cross-section for different Δn (from previous step) together with the index summarized in Table 5-1. The results are then used with the field distribution in the high index region for the calculation of the grating coupling strength κ. Step 2 will be repeated for different Δn to obtain the dependence between κ and Δn.

3. The dependence between κ and N together with other effective parameters are then applied in the 1D TWM laser simulator for device performance simulation.

Dependence between Δn and N:

To introduce enough refractive index change under bias in the p-type grating layer while avoiding significant optical absorption, the material of this layer is chosen to be 1200nm InGaAsP as indicated in Table 5-1 to guarantee a wider bandgap compared to the 1310nm operating wavelength. The index change spectrum under different carrier density of the 1200nm InGaAsP is calculated from the optical gain spectrum using Kramers-Kronig transform and displayed in Figure 5-5 (a). The index change at 1310nm is then extracted from the spectrum as a function of carrier density and been fitted with a 3rd order polynomial as shown in Figure 5-5 (b). The fitting is carried out to avoid repeated calculation of refractive index change when performing device simulation using TWM solver.

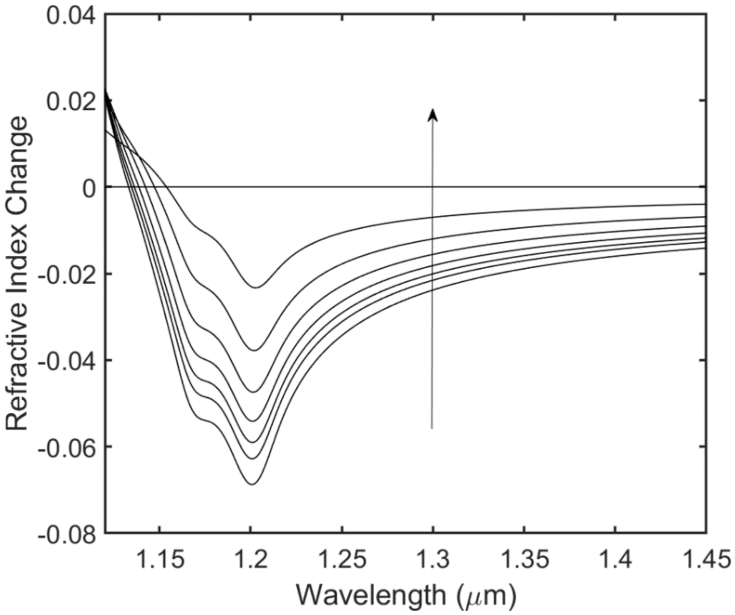

(a)

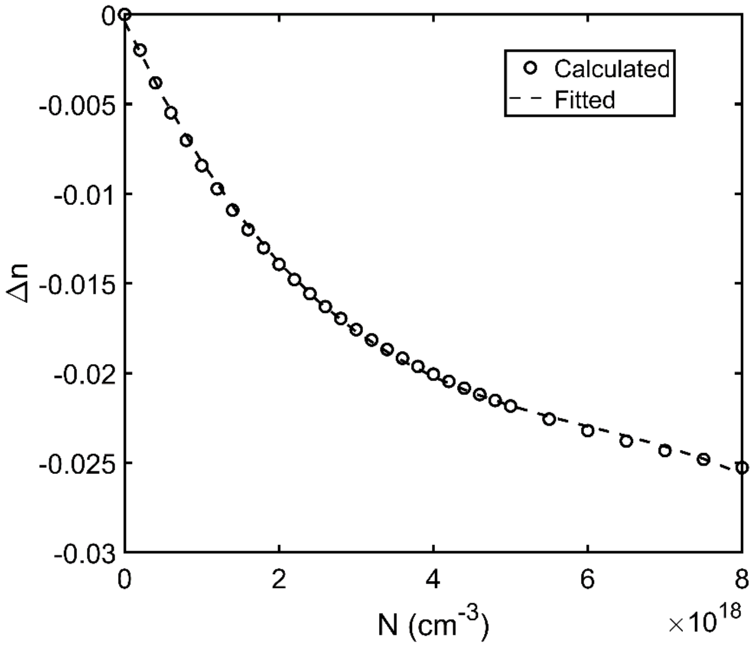

(b)

Figure 5-5 (a) Calculated refractive index change spectrum for the p-type grating layer; (b) Calculated Refractive index change as a function of the carrier density at 1310nm. The fitting polynomial is $\Delta n = p_1 \times N^3 + p_2 \times N^2 + p_3 \times N + p_4$ with $p_1 = -7.2598 \times 10^{-5}, p_2 = 0.0013\ , p_3 = -0.0091\ , p_4 = -4.0075 \times 10^{-4}$.

Dependence between κ and Δn:

To obtain the grating coupling strength κ, the cross-section structure should be determined first. As displayed in Figure 5-4, low κL is beneficial for 3dB bandwidth enhancement indicating a thin n-type grating layer. Also, the bandgap of this layer should be close to the burying material, i.e., InP, to ensure a small base index difference between the high index and low index region. The thickness of the sandwiched InP etching stop layer should be chosen so that it's thick enough to provide proper protection for the p-type grating layer during the etching process while not too thick that the carriers in low index regions can diffuse into the p-type grating layer in high index regions. The p-type grating layer is the layer providing the index change so should be chosen with a relatively larger thickness. With all the considerations, the grating structure is determined and summarized in Table 5-1 with a desired normalized grating coupling strength κL of 1.1~1.2.

The grating coupling coefficient κ is evaluated by first calculating the effective indices n_{eff} and field distribution $\phi(x, y)$ in the cross-section as shown in Figure 5-6 (a), then performing the integration defined in Eq. (2.6). Given the range of index change in the p-type grating layer shown in Figure 5-5 (b) and the cross-section structure, κ is calculated as a function of Δn and displayed in Figure 5-6 (b). The κ~Δn curve is then again fitted with a straight line and will be adopted in the laser solver.

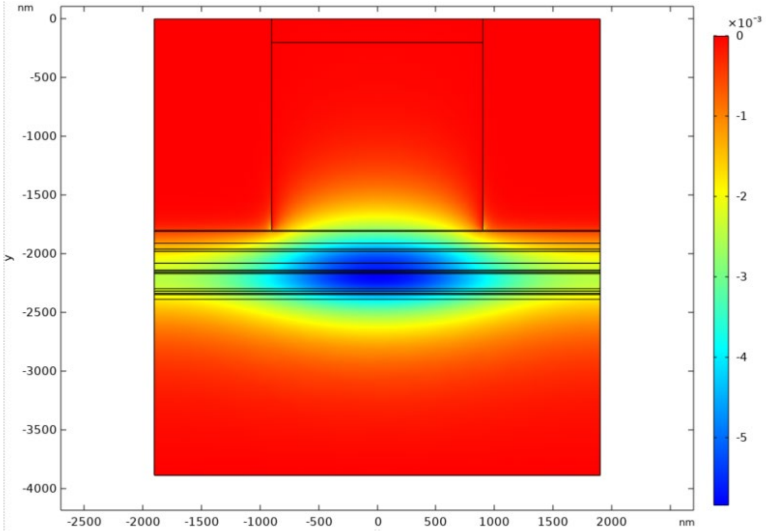

(a)

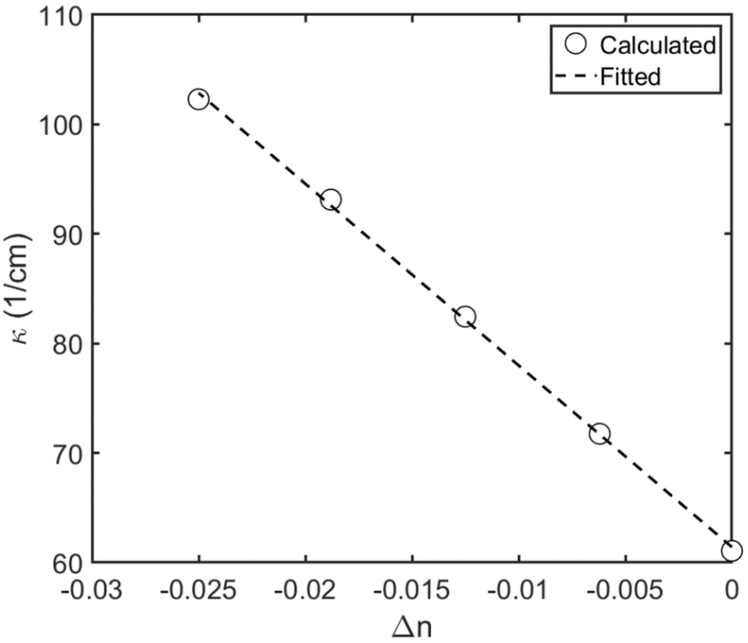

(b)

Figure 5-6 (a) Example of the field distribution for optical mode in the cross-section and (b) the calculated κ~ Δn curve.

Device performance simulation:

The extracted effective parameters from cross-section and other laser parameters used in the TWM laser solver are summarized in Table 5-2. The dependence between grating coupling coefficient κ and carrier density N is obtained from the results of previous sections and will be called in the solver to calculate the varying of κ under different bias. Two DFB structures, one HR-AR coated uniform grating and one AR-AR coated $\lambda/4$ phase-shifted grating, are simulated and Figure 5-7 displays the L-I curves and AM small signal responses of the two structures with conventional grating, i.e., no periodic current blocking, as the reference. Figure 5-8 shows the L-I curves and AM small signal responses of the two structures with the proposed periodic current blocking grating. The proposed grating has minor effect on the DC characteristics, i.e., threshold current and slope efficiency, of the DFB laser except for a slight nonlinearity in the LI curve for the uniform grating structure. The 3dB bandwidth improvement for different structures are summarized in Table 5-3 and Table 5-4. As discussed in the last paragraph of section 5.3, the cavity loss of phase-shifted grating decreases faster with increasing grating coupling strength compared with uniform grating, therefore will see a stronger extension of the 3dB bandwidth. This phenomenon is verified by the results from the self-consistent simulation and it is also clear from Table 5-3 that the enhancement will gradually saturate as the DC bias current been raised. Saturation effect is understandable as the slope of $\alpha_c \sim \kappa$ curve decreases with increasing κ.

Table 5-2
Parameters in Laser Simulation

Symbol	Physical Meaning	Values
Λ	Bragg grating period (nm)	203
w	active region width (μm)	1.8
d	active region thickness (nm)	55
L	total cavity length (μm)	180
V_p	volume of p-type layer (μm^3)	
Γ	optical confinement factor	0.1
n_{eff}^0	effective index without injection	3.226
n_g	group index	3.7
α_L	internal loss (cm^{-1})	8.83
α_H	linewidth enhancement factor	2.5
g_N	differential gain (cm^{-1})	1935
N_{tr}	transparent carrier density ($10^{18} cm^{-3}$)	0.595
ϵ	nonlinear gain saturation coefficient ($10^{-17} cm^3$)	3
τ_c	carrier lifetime (ns)	0.5
n_{sp}	population inversion factor	1.7
γ	spontaneous emission coupling coefficient	1×10^{-4}

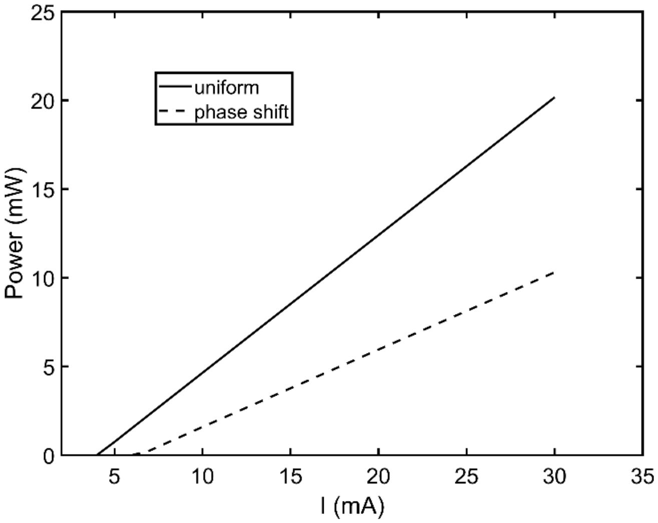
Power (mW)
I (mA)
uniform
phase shift
0
5
10
15
20
25
5
10
15
20
25
30
35

(a)

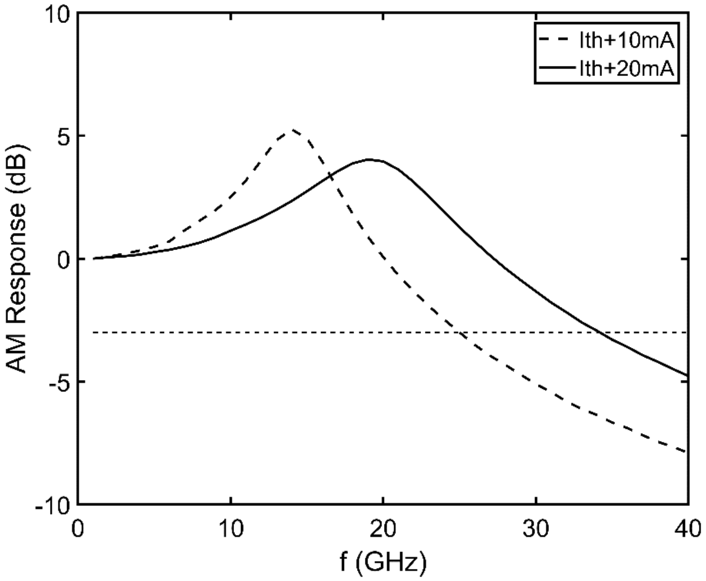
AM Response (dB)
f (GHz)
Ith+10mA
Ith+20mA
10
5
0
-5
-10
0
10
20
30
40

(b)

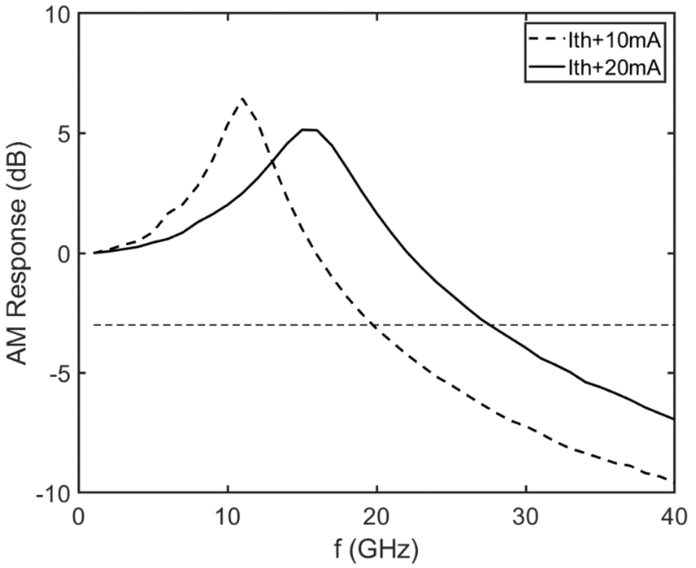

(c)

Figure 5-7 (a) L-I curves of DFB laser with conventional grating; (b) AM small signal response of conventional uniform grating DFB laser; (c) AM small signal response of conventional λ/4 phase-shifted grating DFB laser.

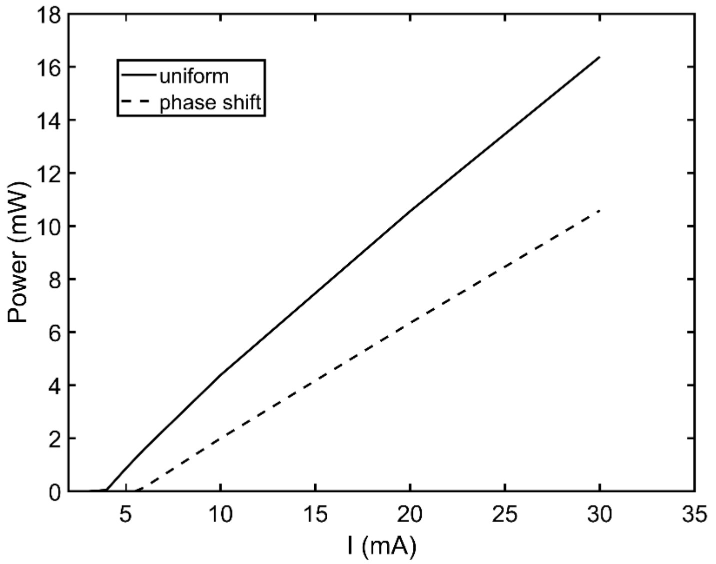

(a)

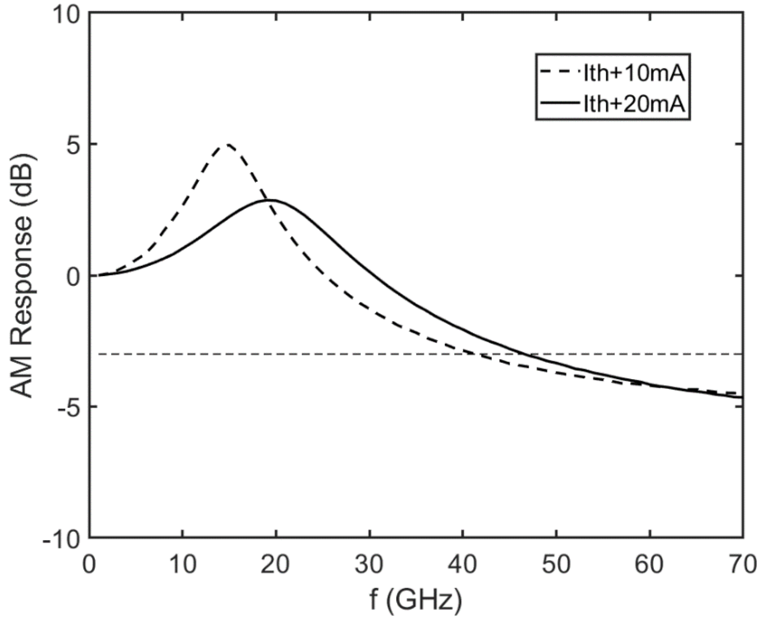
AM Response (dB)
f (GHz)
Ith+10mA
Ith+20mA
10
5
0
-5
-10
0
10
20
30
40
50
60
70

(b)

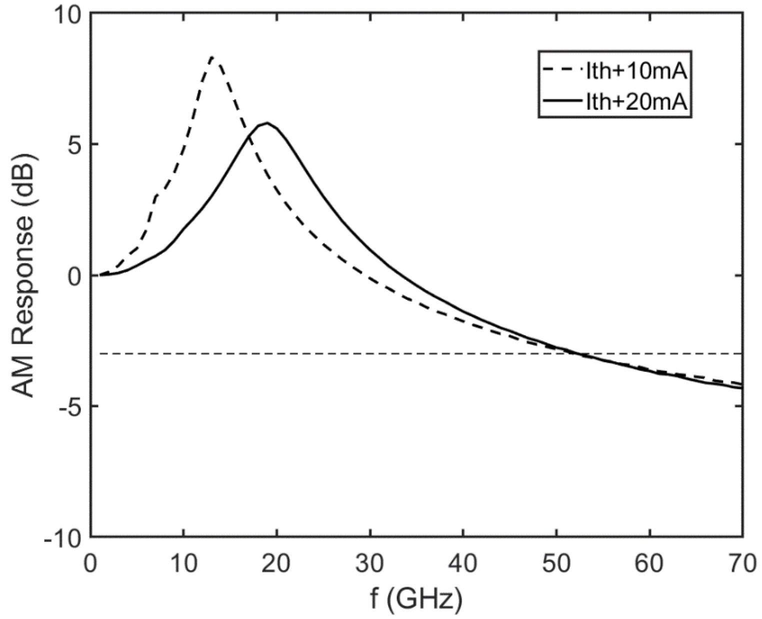
AM Response (dB)
f (GHz)
Ith+10mA
Ith+20mA
10
5
0
-5
-10
0
10
20
30
40
50
60
70

(c)

Figure 5-8 (a) L-I curves of DFB laser with conventional grating; (b) AM small signal response of conventional uniform grating DFB laser; (c) AM small signal response of conventional λ/4 phase-shifted grating DFB laser.

Table 5-3
3dB Bandwidth Enhancement

	Uniform		**Phase shift**	
	Ith+10mA	**Ith+20mA**	**Ith+10mA**	**Ith+20mA**
f_{3dB} **for conventional grating (GHz)**	25	34	20	28
f_{3dB} **for proposed grating (GHz)**	41	46	51	52
f_{3dB} **improvement**	64%	36%	155%	86%

Table 5-4
3dB Bandwidth Enhancement Under Constant Output Power (one facet)

	Uniform		**Phase shift**	
	5mW	**10mW**	**5mW**	**10mW**
f_{3dB} **for conventional grating (GHz)**	20	28	21	30
f_{3dB} **for proposed grating (GHz)**	35	44	51	59
f_{3dB} **improvement**	75%	57%	142%	96%

5.4 Summary

In this chapter, different approaches for DML modulation bandwidth enhancement and the concept of improving the net differential gain by introducing a negative differential loss is briefly explained first. The conventional small signal transfer function derived from the rate equation model is then discussed to show the connection between the 3dB bandwidth and the relaxation oscillation frequency, damping frequency. A more comprehensive transfer function is also derived with the constant cavity loss assumption lifted and the improvement of the relaxation oscillation frequency and damping frequency from the negative differential cavity loss is presented analytically. The structure of the proposed periodic current blocking grating is then explained in detail to show the mechanism of reverse p-n junction behind the negative differential cavity loss realization. The method to link the variation of grating coupling strength with different carrier densities and guidance for grating structure design are displayed in section 5.4 followed by a self-consistent simulation of the proposed DFB laser. The results from numerical simulation shows excellent 3dB bandwidth improvement with both uniform and phase-shifted grating.

Chapter 6 Conclusions and Future Work

6.1 Conclusions

Semiconductor lasers is a key enabling device in a variety of optical communication and sensing systems and numerical simulation provides an indispensable tool for designing of such devices. The primary objective of this research is to investigate novel laser structures with numerical simulation tools to improve the device performance in terms of tunability, noise, and modulation bandwidth. Laser modeling and solution techniques have been described and in-house built solver is developed and verified. A DFL, a DFB laser with asymmetric $\lambda/8$ phase-shifted grating, and a DFB laser with periodic current blocking grating are studied numerically for their performance.

For the DFL, the cancelling effect between the shift of the grating stopband and the tuning of the lasing mode inside the stopband is identified as the reason for the low tuning efficiency in the initial design. The gain elimination in the center section through QWI technique is proposed for improvement and numerical simulation of the modified design exhibit high modulation efficiency. A small parasitic power fluctuation and good linearity in tuning are also displayed. It can also be conveniently DC biased in a broad range to generate the output power at flexible levels as required, without jeopardizing its frequency tuning range and modulation efficiency.

For the asymmetric $\lambda/8$ phase-shifted grating DFB laser, reduction of the RIN through LSHB introduced by the grating phase-shift is explained. The reason behind an optimized grating phase-shift position away from the HR-coated facet is identified as the power leakage resulting from the non-ideal HR coating. The quality factor of the laser cavity is found to be the decisive figure-of-merit behind the optimization and the device performance dependence on grating coupling coefficient, cavity length, and normalized coupling coefficient is investigated and design guideline is given.

For the DFB laser with periodic current blocking grating, a small signal transfer function is derived with the constant cavity loss assumption lifted and the improvement of the relaxation oscillation frequency and damping frequency from the negative differential cavity loss is presented analytically. The structure of the proposed periodic current blocking grating is explained in detail to show the negative differential cavity loss realization. Self-consistent simulation of the proposed structure confirms excellent 3dB bandwidth improvement with both uniform and phase-shifted grating.

6.2 Future work

Based on the research work done in this thesis, following topic are worth further investigation:

1. In chapter 3, the normalized grating coupling coefficient κL of the DFL is chosen to be high for a broader tuning range (wider stopband). However, large κL will generally introduce strong LSHB and affect the yield of the device, which require more investigation into this problem together with the possible mode hopping issue under different facet phase conditions considering different combinations of laser parameters.

2. The DFB laser with asymmetric $\lambda/8$ phase-shifted grating is in fabrication process now and testing should be performed once the completed chips are delivered. The RIN of the laser should be evaluated and compared to conventional structure to verify the RIN reduction through LSHB. The yield of the design should also be studied considering the strong LSHB in the cavity.

3. In chapter 5, the numerical simulation of the periodic current blocking grating DFB is performed without considering carrier diffusion in the grating region. However, full carrier transport model is necessary for a more accurate analysis of the 3dB bandwidth enhancement. Also, experimental verification should be done to confirm the ability to generate negative differential cavity loss from the current blocking effect.

Bibliography

[1] J. J. Martínez, J. I. Gregorio, A. L. Lucia, A. V. Velasco, J. C. Aguado, and M. Á. Binué, “Novel WDM-PON architecture based on a spectrally efficient IM-FSK scheme using DMLs and RSOAs”, *IEEE J. Light. Technol.*, vol. 26, no. 3, pp. 350-356, Feb. 2008.

[2] J. Prat, V. Polo, C. Bock, C. Arellano, J. J. Vegas Olmos, “Full-duplex single fiber transmission using FSK downstream and IM remote upstream modulations for fiber-to-the-home”, *IEEE Photon. Technol. Lett.*, vol. 17, no. 3, pp. 702-704, Mar. 2005.

[3] D. van Veen, W. Pohlmann, B. Farah, T. Pfeiffer, P. Vetter, “Measurement and mitigation of wavelength drift due to self-heating of tunable burst-mode DML for TWDM-PON”, *Proc. 2014 Int. Conf. Opt. Fiber Commun.*, Mar. 2014.

[4] N. Grote, M. Baier, and F. Soares, ‘Ultra-Fast Semiconductor Laser Sources’, in Herbert Venghaus, Norbert Grote (ed.) Fibre Optic Communication: Key Devices (second ed). Switzerland: Springer International Publishing, 2017, pp. 819-820.

[5] Jens Buus and Edmond J. Murphy, “Tunable Lasers in Optical Networks,” *IEEE J. Light. Technol.*, Vol. 24, Issue 1, pp. 5-11, Jan. 2006.

[6] B. Guenther and R. Buser, "Tunable lasers - An overview," *IEEE J. Quantum Electron.*, vol. 18, no. 8, pp. 1179-1185, August 1982.

[7] L. A. Coldren, G. A. Fish, Y. Akulova, J. S. Barton, L. Johansson and C. W. Coldren, "Tunable semiconductor lasers: a tutorial," *IEEE J. Light. Technol.*, vol. 22, no. 1, pp. 193-202, Jan. 2004.

[8] G. Fish and K. Affolter, “Tunable lasers and their impact on optical networks,” presented at the *Communications Design Conf.*, San Jose, CA, Aug. 2002.

[9] D. J. Blumenthal, B. E. Olsson, G. Rossi, T. Dimmick, L. Rau, M. L. Ma’anovic’, O. A. Lavrova, R. Doshi, O. Jerphagnon, J. E. Bowers, V. Kaman, L. A. Coldren, and J. Barton, “All-Optical label swapping networks and technologies,” *IEEE J. Light. Technol., Special Issue Optical Networks*, vol. 18, pp. 2058–2075, Dec. 2000.

[10] Joji Maeda, Kazutoyo Kusama, and Yutaka Fukuchi, "Mitigation of signal fading in radio over fiber transmission using fiber nonlinearity," *Opt. Express*, vol. 17, no. 6, pp. 4518-4525, 2009.

[11] M. J. Fice, E. Rouvalis, F. van Dijk, A. Accard, F. Lelarge, C. C. Renaud, G. Carpintero, and A. J. Seeds, "146-GHz millimeter-wave radio-over-fiber photonic wireless transmission system," *Opt. Express*, vol. 20, no. 2, pp. 1769-1774, 2012.

[12] C. H. Cox, E. I. Ackerman, G. E. Betts and J. L. Prince, "Limits on the performance of RF-over-fiber links and their impact on device design," IEEE Trans. Microw. Theory Tech., vol. 54, no. 2, pp. 906-920, Feb. 2006.

[13] Y. Zhao et al., "High-power and low-noise DFB semiconductor lasers for RF photonic links," *IEEE Avionics, Fiber-Optics and Photonics Digest CD*, Cocoa Beach, FL, pp. 66-67, 2012.

[14] M. Faugeron et al., "High-Power, Low RIN 1.55-μm Directly Modulated DFB Lasers for Analog Signal Transmission," *IEEE Photon. Technol. Lett.*, vol. 24, no. 2, pp. 116-118, Jan.15, 2012.

[15] M. G. Allen, "Challenges and opportunities for next generation diode laser active sensing," *2009 Conference on Lasers and Electro-Optics and 2009 Conference on Quantum electronics and Laser Science Conference*, Baltimore, MD, 2009, pp. 1-2, doi: 10.1364/CLEO.2009.CThI3.

[16] P. A. Morton and M. J. Morton, "High-Power, Ultra-Low Noise Hybrid Lasers for Microwave Photonics and Optical Sensing," *IEEE J. Light. Technol.*, vol. 36, no. 21, pp. 5048-5057, 1 Nov.1, 2018.

[17] Masahiro Aoki and Ute Troppenz, 'Ultra-Fast Semiconductor Laser Sources', in Herbert Venghaus, Norbert Grote (ed.) *Fibre Optic Communication: Key Devices (second ed)*. Switzerland: Springer International Publishing, 2017, pp. 151-208.

[18] Edward Harstead, Pieter H. van Heyningen, 'Optical Access Networks', in Ivan Kaminow Tingye Li (ed.) *Optical Fiber Telecommunications IV-B: Optics and Photonics (fourth ed)*. Academic Press, 2002, pp.438-513.

[19] Lam, C. F., Liu, H., Koley, B., Zhao, X., Kamalov, V., and Gill, V., "Fiber optic communication technologies: what's needed for datacenter network operations," *Proceedings of the IEEE Commun. Mag.*, 48, pp. 32–39, 2010.

[20] J. J. Huang et al., "Manufacturing excellence and future challenges of wireless laser components for 4G/5G optical mobile fronthaul networks," *2018 27th Wireless and Optical Communication Conference (WOCC)*, Hualien, pp. 1-2, 2018.

[21] Alavi, S E et al. "Towards 5G: A Photonic Based Millimeter Wave Signal Generation for Applying in 5G Access Fronthaul," *Scientific reports*, vol. 6, pp. 19891, 27 Jan. 2016.

[22] T. Yamamoto, "High-speed directly modulated lasers," *OFC/NFOEC*, Los Angeles, CA, 2012, pp. 1-39.

[23] Yasuhiro Matsui, 'Directly Modulated Laser Technology: Past, Present, and Future', in Frank Chang (ed.) *Datacenter Connectivity Technologies: Principles and Practice*. River Publishers, 2018, pp. 87-171.

[24] P. A. Morton et al., "Packaged 1.55μm DFB laser with 25 GHz modulation bandwidth," *Electron. Lett.*, vol. 30, no. 24, pp. 2044-2046, 24 Nov. 1994.

[25] N. Nakamura et al., "25.8Gbps Direct Modulation AlGaInAs DFB Lasers of Low Power Consumption and Wide Temperature Range Operation for Data Center," *Optical Fiber Communication Conference*, OSA Technical Digest (online) (Optical Society of America, 2015), paper W2A.53.

[26] T. Tadokoro, T. Yamanaka, F. Kano, H. Oohashi, Y. Kondo and K. Kishi, “Operation of a 25-Gb/s Direct Modulation Ridge Waveguide MQW-DFB Laser up to 85°C,” *IEEE Photon. Technol. Lett.*, vol. 21, no. 16, pp. 1154-1156, Aug.15, 2009.

[27] 400G Ethernet http://www.ieee802.org/3/bs/timeline 3bs 0915.pdf

[28] Hélène Debrégeas, ‘Widely Tunable Laser Diodes’, in Herbert Venghaus, Norbert Grote (ed.) *Fibre Optic Communication: Key Devices (second ed)*. Switzerland: Springer International Publishing, 2017, pp. 209-248.

[29] Sören Dhoore, Anna Köninger, Ralf Meyer, Gunther Roelkens, Geert Morthier, “Electronically Tunable Distributed Feedback (DFB) Laser on Silicon,” *Lasers Photonics Rev.*, vol. 13, 1800287, March 2019.

[30] D. Vakhshoori, P. D. Wang, M. Azimi, K. J. Knopp, and M. Jiang, "MEMS-Tunable Vertical-Cavity Surface-Emitting Lasers," *Optical Fiber Communication Conference and International Conference on Quantum Information*, 2001 OSA Technical Digest Series (Optical Society of America, 2001), paper TuJ1.

[31] H. Cai, A. Q. Liu, X. M. Zhang, J. Tamil, Q. X. Zhang, D. Y. Tang, C. Lu, “A Miniature Tunable Coupled-Cavity Laser Constructed by Micromachining Technology”, *Appl. Phys. Lett.*, vol. 92, 031105, 2008.

[32] Oh Kee Kwon, Jong Hoi Kim, Kang Ho Kim, Eun Deok Sim, and Kwang Ryong Oh, "Widely tunable multichannel grating cavity laser," *IEEE Photon. Technol. Lett.*, vol. 18, no. 16, pp. 1699-1701, Aug. 2006.

[33] E. Geerlings et al., "Widely Tunable Micro-Mechanical External-Cavity Diode Laser Emitting Around 2.1μm," *IEEE J. Quantum Electron.*, vol. 44, no. 11, pp. 1071-1075, Nov. 2008.

[34] R. Todt, T. Jacke, R. Laroy, G. Morthier and M. -. Amann, "Demonstration of Vernier effect tuning in tunable twin-guide laser diodes," *IEE Proceedings-Optoelectronics*, vol. 152, no. 2, pp. 66-71, 8 April 2005.

[35] M. J. Wallace, Gaurav Jain, Robert Mckenna, Frank Bello, and J. F. Donegan, "Tuning behaviour of slotted vernier widely tunable lasers," *Opt. Express* 27, 17122-17137 (2019).

[36] K. Y. Lau, "Frequency modulation and linewidth of gain-levered two-section single quantum well lasers," *Appl. Phys. Lett.*, vol. 57, no. 20, pp. 2068-2070, Nov. 1990.

[37] M. Ferreira, "Frequency noise and modulation of a four-section DBR laser," *IEEE J. Quantum Electron.*, vol. 32, no. 5, pp. 851-858, May 1996.

[38] S. Ogita, Y. Kotaki, M. Matsuda, Y. Kuwahara, H. Onaka, H. Miyata, and H. Ishikawa, "FM response of narrow-linewidth, multielectrode λ/4 shift DFB laser," *IEEE Photon. Technol. Lett.*, vol. 2, no. 3, pp. 165-166, Mar. 1990.

[39] M. Okai, M. Suzuki, and M. Aoki, "Complex-coupled λ/4-shifted DFB laser with a flat FM response," *IEEE J. Sel. Top. Quantum Electron.*, vol. 1, no. 2, pp. 461-465, June 1995.

[40] K. Tsuzuki et al., "Full C-Band Tunable DFB Laser Array Copackaged With InP Mach–Zehnder Modulator for DWDM Optical Communication Systems," *IEEE J. Sel. Top. Quantum Electron.*, vol. 15, no. 3, pp. 521-527, May-June 2009.

[41] H. Ishii, K. Kasaya, H. Oohashi, Y. Shibata, H. Yasaka and K. Okamoto, "Widely Wavelength-Tunable DFB Laser Array Integrated With Funnel Combiner," *IEEE J. Sel. Top. Quantum Electron.*, vol. 13, no. 5, pp. 1089-1094, Sept.-Oct. 2007.

[42] Suhyun Kim, Youngchul Chung, Su Hwan Oh and Moon-Ho Park, "Design and analysis of widely tunable sampled grating DFB laser diode integrated with sampled grating distributed Bragg reflector," *IEEE Photon. Technol. Lett.*, vol. 16, no. 1, pp. 15-17, Jan. 2004.

[43] J. Klamkin, J. M. Hutchinson, J. T. Getty, L. A. Johansson, E. J. Skogen and L. A. Coldren, "High efficiency widely tunable SGDBR lasers for improved direct modulation performance," *IEEE J. Sel. Top. Quantum Electron.*, vol. 11, no. 5, pp. 931-938, Sept.-Oct. 2005.

[44] M. Kuznetsov, "Design of widely tunable semiconductor three-branch lasers," *J. Light. Technol.*, vol. 12, no. 12, pp. 2100-2106, Dec. 1994.

[45] K. Yoon et al., "10-Gb/s Tunable External Cavity Laser Using an Asymmetric Ring Resonator Reflector," *IEEE Photon. Technol. Lett.*, vol. 24, no. 17, pp. 1481-1483, Sept.1, 2012.

[46] Yeyu Zhu and Lin Zhu, "Narrow-linewidth, tunable external cavity dual-band diode lasers through InP/GaAs-Si_3N_4 hybrid integration," *Opt. Express* 27, 2354-2362 (2019).

[47] T. Komljenovic, S. Srinivasan, E. Norberg, M. Davenport, G. Fish and J. E. Bowers, "Widely Tunable Narrow-Linewidth Monolithically Integrated External-Cavity Semiconductor Lasers," *IEEE J. Sel. Top. Quantum Electron.*, vol. 21, no. 6, pp. 214-222, Nov.-Dec. 2015.

[48] W. T. Tsang, N. A. Olsson, R. A. Linke and R. A. Logan, "1.5µm wavelength GaInAsP C3 lasers: single-frequency operation and wideband frequency tuning," *Electron. Lett.*, vol. 19, no. 11, pp. 415-417, 26 May 1983.

[49] L. A. Coldren, B. I. Miller, K. Iga, and J. A. Rentschler, “Monolithic two-section GaInAsP/InP active-optical-resonator devices formed with RIE mirrors,” *Appl. Phys. Lett.*, vol. 38, no. 5, pp. 315–317, 1981.

[50] S. Cheung, "High-Speed, Directly-Modulated Widely Tunable 1310nm Coupled Cavity Laser Via Multimode Interference," *IEEE J. Light. Technol.*, vol. 37, no. 9, pp. 2133-2139, 1 May1, 2019.

[51] V. Jayaraman, D. A. Cohen, and L. A. Coldren, “Extended tuning range semiconductor lasers with sampled gratings,” *Proc. IEEE LEOS ’91*, San Jose, CA, 1991, paper SDL15.5.

[52] A. J. Ward et al., "Realization of phase grating comb reflectors and their application to widely tunable DBR lasers," *IEEE Photon. Technol. Lett.*, vol. 16, no. 11, pp. 2427-2429, Nov. 2004.

[53] T. Matsumoto et al., "Narrow spectral linewidth full band tunable laser based on waveguide ring resonators with low power consumption," *2010 Conference on Optical Fiber Communication (OFC/NFOEC), collocated National Fiber Optic Engineers Conference*, San Diego, CA, 2010, pp. 1-3.

[54] M. Ren, H. Cai, J. M. Tsai, W. M. Zhu, D. L. Kwong and A. Q. Liu, "A tunable laser using double-ring resonator external cavity via free-carrier dispersion effect," *2011 16th International Solid-State Sensors, Actuators and Microsystems Conference*, Beijing, 2011, pp. 1504-1507.

[55] H. Ishii, T. Tanobe, F. Kano, Y. Tohmori, Y. Kondo, and Y. Yoshikuni, “Broad-range wavelength coverage (62.4nm) with superstructure-grating DBR laser,” *Electron. Lett.*, vol. 32, pp. 454–455, 1996.

[56] L. A. Coldren, "Monolithic tunable diode lasers," *IEEE J. Sel. Top. Quantum Electron.*, vol. 6, no. 6, pp. 988-999, Nov.-Dec. 2000.

[57] M. Faugeron et al., "High-Power, Low RIN 1.55-μm Directly Modulated DFB Lasers for Analog Signal Transmission," *IEEE Photon. Technol. Lett.*, vol. 24, no. 2, pp. 116-118, Jan.15, 2012.

[58] W. K. Marshall, J. Paslaski, and A. Yariv,” Reduction of relative intensity noise of the output field of semiconductor lasers due to propagation in dispersive optical fiber,” *Appl. Phys. Lett.*, vol. 68, no.18, pp. 2496-2498, 1996.

[59] M. A. Newkirk and K. J. Vahala, "Amplitude-phase decorrelation: a method for reducing intensity noise in semiconductor lasers," *IEEE J. Quantum Electron.*, vol. 27, no. 1, pp. 13-22, Jan. 1991.

[60] G. Baili et al., "Novel architectures of very low RIN semiconductor lasers in extended cavities for high performance microwave links," *2006 International Topical Meeting on Microwave Photonics*, Grenoble, 2006, pp. 1-4.

[61] J. Liu et al., "Narrow linewidth distributed-feedback laser with low relative intensity noise," *2015 14th International Conference on Optical Communications and Networks (ICOCN)*, Nanjing, 2015, pp. 1-3.

[62] P.A. Morton, R.A. Logan, T. Tanbun-Ek, P.F. Sciortino, A.M. Sergent, R.K. Montgomery, and B.T. Lee, “25 GHz bandwidth 1.55μm GaInAsP p-doped strained multiquantum-well lasers,” *Electron. Lett.*, vol. 28, pp. 2156–2157, 1992.

[63] S. Weisser, E.C. Larkins, K. Czotscher, W. Benz, J. Daleiden, I. Esquivias, J. Fleissner, J.D. Ralston, B. Romero, R.E. Sah, A. Schonfelder, and J. Rosenzweig, “Damping-limited modulation bandwidths up to 40 GHz in undoped short-cavity $In_{0.35}Ga_{0.65}As$-GaAs multiple-quantum-well lasers “, *IEEE Photon. Technol. Lett.*, vol. 8, pp. 608–610, 1996.

[64] Y. Matsui, H. Murai, S. Arahira, Y. Ogawa, and A. Suzuki, “Enhanced modulation bandwidth for strain-compensated InGaAlAs-InGaAsP MQW lasers,” *IEEE J. Quantum Electron.*, vol. 34, pp. 1970–1978, 1998.

[65] K. Vahala, and A. Yariv, “Detuned loading in coupled cavity semiconductor lasers - effect on quantum noise and dynamics,” *Appl. Phys. Lett.*, vol. 45, p. 501, 1984.

[66] S. Yamaoka et al., "239.3-Gbit/s net rate PAM-4 transmission using directly modulated membrane lasers on high-thermal-conductivity SiC," *45th European Conference on Optical Communication (ECOC 2019)*, Dublin, Ireland, 2019, pp. 1-4.

[67] A. A. Tager and B. B. Elenkrig, “Stability Regimes and High-Frequency Modulation of Laser Diodes with Short External Cavity,” *IEEE J. Quantum Electron.*, vol. 29, pp. 2886–2890, 1993.

[68] U. Troppenz, J. Kreissl, M. M¨ohrle, C. Bornholdt, W. Rehbein, B. Sartorius, I. Woods, and M. Schell, “40 Gbit/s directly modulated lasers: physics and application,” *Proceedings of the SPIE*, vol. 7953, id. 79530F, 2011.

[69] J. Qi, Y. Xi and X. Li, "Enhanced modulation bandwidth by exploiting photon resonance in push-pull modulated DFB lasers," *2015 International Conference on Numerical Simulation of Optoelectronic Devices (NUSOD)*, Taipei, 2015, pp. 127-128.

[70] J. Kreissl, V. Vercesi, U. Troppenz, T. Gaertner, W. Wenisch, and M. Schell, “Up to 40 Gb/s Directly Modulated Laser Operating at Low Driving Current: Buried-

Heterostructure Passive Feedback Laser (BH- PFL),” *IEEE Photon. Technol. Lett.*, vol. 24, pp. 362–364, 2012.

[71] J. Kreissl, U. Troppenz, W. Rehbein, T. Gaertner, P. Harde and M. Radziunas, "40 Gbit/s Directly Modulated Passive Feedback Laser with Complex-Coupled DFB Section," *33rd European Conference and Exhibition of Optical Communication*, Berlin, Germany, 2007, pp. 1-2.

[72] Y. Matsui, R. Schatz, T. Pham, W. A. Ling, G. Carey, H. M. Daghighian, D. Adams, T. Sudo, and C. Roxlo, “55 GHz Bandwidth Distributed Reflector Laser,” *IEEE J. Light. Technol.*, vol. 35, pp. 397–403, 2017 (Invited).

[73] Y. Matsui, T. Pham, W. A. Ling, R. Schatz, G. Carey, H. Daghighian, T. Sudo, C. Roxlo, “55-GHz bandwidth short-cavity distributed reflector laser and its application to 112-Gb/s PAM-4,” *Optical Fiber Communications Conference and Exhibition (OFC)*, PDP paper Th5B.4, 2016.

[74] S. Murata, A. Tomita and A. Suzuki, "Influence of free carrier plasma effect on carrier-induced refractive index change for quantum-well lasers," *IEEE Photon. Technol. Lett.*, vol. 5, no. 1, pp. 16-19, Jan. 1993.

[75] R. J. Keyes and T. M. Quist, “Recombination radiation emitted by gallium arsenide,” *Proc. IRE*, 50 (8), pp. 1822-1823, 1962.

[76] R. H. Rediker, “Research at Lincoln Laboratory leading up to the development of the injection laser in 1962,” *IEEE J. Quantum Electron.*, QE-23 (6), 692 –695 (1987).

[77] R. N. Hall, G. E. Fenner, J. D. Kingsley, T. J. Soltys, and R. O. Carlson, "Coherent light emission from GaAs junctions," *Phys. Rev. Lett.*, 9 (9), 366 –368 (1962).

[78] https://optics.synopsys.com/rsoft/rsoft-system-network-optsim.html

[79] Xun Li, A. D. Sadovnikov, W. -. Huang and T. Makino, "A physics-based three-dimensional model for distributed feedback laser diodes," *IEEE J. Quantum Electron.*, vol. 34, no. 9, pp. 1545-1553, Sept. 1998.

[80] Wei Li, Wei-Ping Huang and Xun Li, "Digital filter approach for Simulation of a complex integrated laser diode based on the traveling-wave model," *IEEE J. Quantum Electron.*, vol. 40, no. 5, pp. 473-480, May 2004.

[81] H. Kogelnik and C. V. Shank, "Coupled-wave theory of distributed feedback lasers," *J. Appl. Phys.*, vol. 43, no. 5, pp. 2327-2335, May 1972.

[82] Xun Li, 'Distributed Feedback Lasers: Quasi-3D Static and Dynamic Model,' in Joachim Piprek, *Optoelectronic Devices - Advanced Simulation and Analysis*. Springer, New York, 2005, pp. 87-119.

[83] M. Sargent III, M. O. Scully, and W. E. Lamb: *Laser Physics* (Addison-Wesley, Reading, MA 1974).

[84] C. H. Henry, R. A. Logan, and K. A. Bertness, "Spectral dependence of the change in refractive index due to carrier injection in GaAs lasers," *J. Appl. Phys.*, 52, pp. 4457, 1981.

[85] C. Henry, "Theory of the linewidth of semiconductor lasers," *IEEE J. Quantum Electron.*, vol. 18, no. 2, pp. 259-264, Feb. 1982.

[86] X. Li, 'Solution techniques for carrier transport and thermal diffusion equations' in *Optoelectronic Device: Design, Modeling, and Simulation*. New York, NY, USA: Cambridge Univ. Press, 2009.

[87] X. Li, 'Solution techniques for material gain equations' in *Optoelectronic Device: Design, Modeling, and Simulation*. New York, NY, USA: Cambridge Univ. Press, 2009.

[88] S. L. Chuang, *Physics of Optoelectronic Devices*. Wiley, New York, 1995.

[89] D. Ahn, S. L. Chuang, and Y. C. Chang, "Valence-band mixing effects on the gain and the refractive index change of quantum-well lasers," *J. Appl. Phys*., 64, pp. 4056, 1988.

[90] S. L. Chuang, "Efficient band-structure calculations of strained quantum wells," *Phys. Rev. B*, 43, 9649, April 1991.

[91] I. Vurgaftman, J. R. Meyer, and L. R. Ram-Mohan, "Band parameters for III–V compound semiconductors and their alloys," *J. Appl. Phys.*, 89, pp. 5815, 2001.

[92] X. Li and W. P. Huang, "Simulation of DFB semiconductor lasers incorporating thermal effects", *IEEE J. Quantum Electron.*, vol. 31, no. 10, pp. 1848-1855, Oct. 1995.

[93] Y. P. Xi, X. Li, and W. P. Huang, “Time-domain standing-wave approach based on cold cavity modes for simulation of DFB lasers,” *IEEE J. Quantum Electron.*, vol. 44, no. 10, pp. 931-937, Oct. 2008.

[94] X. Li, ‘Solution techniques for optical equations’ in *Optoelectronic Device: Design, Modeling, and Simulation*. New York, NY, USA: Cambridge Univ. Press, 2009.

[95] William H. Press, Saul A. Teukolsky, William T. Vetterling, and Brian P. Flannery, *Numerical Recipes in C (second ed)*. Cambridge University Press, Cambridge, 1992.

[96] M. Kuznetsov, “Theory of wavelength tuning in two-segment distributed feedback lasers,” *IEEE J. Quantum Electron.*, vol. 24, no. 9, pp. 1837-1844, Sept. 1988.

[97] T. Yamanaka, Y. Yoshikuni, K. Yokoyama, W. Lui, and S. Seki, “Theoretical study on enhanced differential gain and extremely reduced linewidth enhancement factor in quantum-well lasers,” *IEEE J. Quantum Electron.*, vol. 29, no. 6, pp. 1609-1616, June 1993.

[98] B. Qiu, X. Liu, M. Ke, H. Lee, A. Bryce, J. Aitchison, J. Marsh, and C. Button, “Monolithic fabrication of 2×2 crosspoint switches in InGaAs\InAlGaAs multiple quantum wells using quantum-well intermixing,” *IEEE Photon. Technol. Lett.*, vol. 13, no. 12, pp. 1292–1294, Dec. 2001.

[99] D. Hofstetter, B. Maisenholder, and H. P. Zappe, “Quantum-well intermixing for fabrication of lasers and photonic integrated circuits,” *IEEE J. Sel. Top. Quantum Electron.*, vol. 4, no. 4, pp. 794-802, July/Aug. 1998.

[100] K. Itaya, M. J. Mondry, P. D. Floyd, L. A. Coldren, and J. L. Merz, "Impurity-induced disordering of AlGaInAs quantum wells by low temperature Zn diffusion," *J. Electron. Mater.*, vol. 25, no. 4, pp. 565-569, May 1996.

[101] T. Sasaki and M. Yamaguchi, "Narrow stripe selective MOVPE for high-quality InGaAsP MQWs and its application to photonic integrated circuits," *10th Intern. Conf. on Indium Phosphide and Related Materials*, pp. 353-356, May 1998.

[102] Aoki, M. Suzuki, H. Sano, T. Kawano, T. Ido, T. Taniwatari, K. Uomi, and A. Takai, "InGaAs/InGaAsP MQW electroabsorption modulator integrated with a DFB laser fabricated by bandgap energy control selective-area MOCVD," *IEEE J. Quantum Electron.*, vol. 29, no. 6, pp. 2088–2096, June 1993.

[103] W. Kobayashi, M. Arai, T. Yamanaka, N. Fujiwara, T. Fujisawa, T. Tadokoro, K. Tsuzuki, Y. Kondo, and F. Kano, "Design and fabrication of 10-/40-Gb/s, uncooled electroabsorption modulator integrated DFB laser with butt-joint structure," *IEEE J. Light. Technol.*, vol. 28, no. 1, pp. 164–171, Jan. 2010.

[104] I. V. Kulkova, S. Kadkhodazadeh, N. Kuznetsova, A. Huck, E. S. Semenova, and K. Yvind, "High-quality MOVPE butt-joint integration of InP/AlGaInAs/InGaAsP-based all-active optical components," *J. Cryst. Growth*, vol. 402, pp. 243-248, Sept. 2014.

[105] C. Chen, H. S. Djie, Y. H. Ding, B. S. Ooi, J. C. M. Hwang, and V. Aimez, "Fundamental and dynamic properties of intermixed InGaAs-InGaAsP quantum-well Lasers," *IEEE J. Quantum Electron.*, vol. 46, no. 9, pp. 1368-1374, Sept. 2010.

[106] A. E. Willner, M. Kuznetsov, I. P. Kaminow, U. Koren, T. L. Koch, C. A. Burrus, and G. Raybon, “Multigigahertz bandwidth FM response of frequency tunable two-electrode DFB lasers,” *IEEE Photon. Technol. Lett.*, vol. 1, no. 11, pp. 360-363, Nov. 1989.

[107] R. S. Tucker and D. J. Pope, “Circuit modeling of the effect of diffusion on damping in a narrow-stripe semiconductor laser,” *IEEE J. Quantum Electron.*, vol. 19, no. 7, pp. 1179–1183, July 1983.

[108] K. Petermann, *Laser Diode Modulation and Noise*. Norwell, MA, USA: Kluwer Academic Publishers, 1988.

[109] J.-R. Burie, G. Beuchet, M. Mimoun, P. Pagnod-Rossiaux, B. Ligat, J. C. Bertreux, J.-M. Rousselet, J. Dufour, P. Rougeolle, and F. Laruelle "Ultra high power, ultra low RIN up to 20 GHz 1.55 μm DFB AlGaInAsP laser for analog applications," *Proc. SPIE 7616, Novel In-Plane Semiconductor Lasers IX*, 76160Y, 12 February 2010.

[110] Schatz R, “Longitudinal spatial instability in symmetric semiconductor lasers due to spatial hole burning,” *IEEE J. Quantum Electron.*, vol. 28, pp. 1443–1449, June 1992.

[111] Pan X, Olesen H, Tromborg B,” Spectral linewidth of DFB lasers including the effects of spatial hole burning and nonuniform current injection,” *IEEE Photon. Technol. Lett.*, vol. 2, pp. 312–315, 1990.

[112] Y. Keith Lee, Genlin Tan, G. Pakulski, Toshi Makino, J. M. Xu, "Plasma and thermal effects on the performance of high power floating grating DFB laser," *Proc. SPIE 3038, High-Speed Semiconductor Lasers for Communication*, 10 April, 1997.

Appendix A Derivation of Small Signal AM Response

Assuming the optical field at an arbitrary place inside the laser cavity is $E(z,t)$ and after a round trip it becomes:

$$E(z,t+\tau_L) = E(z,t) r_l r_r \, exp\{\left[\tfrac{1}{2}\Gamma g - \tfrac{1}{2}(1-\Gamma)\alpha + j\beta\right] 2L\}, \qquad \text{(A1)}$$

where g and α are the optical material gain and loss, respectively, β is the optical guided mode propagation constant, L is the cavity length, r_L and r_R are the left and right facet amplitude reflectivities, respectively, and τ_L is the round trip delay time.

By only retaining the first order item, we can approximate the right-hand side (RHS) of Eq. (A1) with

$$[1 + \Gamma g L - (\alpha_i + \alpha_c)L + j2\beta L]E(z,t). \qquad \text{(A2)}$$

Here $\alpha_i = (1-\Gamma)\alpha$ is the modal loss and α_c is the cavity loss, respectively. By the definition of differential, we have $E(z,t+\tau_L) \approx E(z,t) + \tau_L \frac{\partial E(z,t)}{\partial t}$ and it can combined with Eq. (A2) to reach

$$\frac{dE(t)}{dt} = v_g \left[\tfrac{1}{2}\Gamma g - \tfrac{1}{2}(\alpha_i + \alpha_c) + j\beta\right] E(t). \qquad \text{(A3)}$$

Here the position dependence is dropped by an integration over the cavity length and assuming constant parameters everywhere.

By defining the photon number $S(t)$ with $E(t) = \sqrt{S(t)}e^{j\phi(t)}$, we can convert Eq. (A3) to

$$\frac{dS(t)}{dt} = \frac{d[E(t)E^*(t)]}{dt} = v_g[\Gamma g - (\alpha_i + \alpha_c)]S(t). \qquad \text{(A4)}$$

By defining $1/\tau_p = v_g(\alpha_i + \alpha_c)$ as the photon lifetime, and by adding on the spontaneous emission contribution, we finally obtain the photon number rate equation as:

$$\frac{dS(t)}{dt} = \left[v_g \Gamma g - \frac{1}{\tau_p}\right] S(t) + K n_{sp} v_g \Gamma g, \tag{A5}$$

where K is the Petermann's factor, n_{sp} is the population inversion factor. The material gain model for quantum well active region is

$$g = \frac{g_N ln\left(\frac{N(t)}{N_{tr}}\right)}{1+\frac{\Gamma \varepsilon S(t)}{V}}, \tag{A6}$$

where $N(t)$ is the carrier density, N_{tr} is the transparent carrier density, ε is the nonlinear gain suppression factor.

The carrier density rate equation is

$$\frac{dN(t)}{dt} = \eta \frac{I(t)}{qV} - \frac{N(t)}{\tau_n} - \frac{v_g \Gamma g S(t)}{V}, \tag{A7}$$

where η is the current injection efficiency, q is the unit electron charge, τ_n is the carrier lifetime.

For small signal analysis, we have the following assumptions:

$$I(t) = I_0 + \Delta I(t), \Delta I(t) \ll I_0, \tag{A8-1}$$

$$S(t) = S_0 + \Delta S(t), \Delta S(t) \ll S_0, \tag{A8-2}$$

$$N(t) = N_0 + \Delta N(t), \Delta N(t) \ll N_0, \tag{A8-3}$$

where I_0, S_0, and N_0 are defined in the steady state solutions:

$$\left[v_g \Gamma g_0 - \frac{1}{\tau_{po}}\right] S_0 + K n_{sp} v_g \Gamma g_0 = 0, \tag{A9-1}$$

$$g_0 = \frac{g_N ln\left(\frac{N_0}{N_{tr}}\right)}{1+\frac{\Gamma \varepsilon S_0}{V}}, \tag{A9-2}$$

$$\eta\frac{I_0}{qV}-\frac{N_0}{\tau_{n0}}-\frac{v_g\Gamma g_0 S_0}{V}=0. \tag{A9-3}$$

By utilizing Eq. (A8-2) and Eq. (A9-1) and ignoring higher order items, we can convert Eq. (A5) into

$$\frac{d\Delta S}{dt}=\left[v_g\Gamma\left(g_0+\frac{\partial g}{\partial N}\Delta N+\frac{\partial g}{\partial S}\Delta S\right)-\left(\frac{1}{\tau_{p0}}+\frac{\partial\frac{1}{\tau_p}}{\partial N}\Delta N\right)\right](S_0+\Delta S)+$$

$$Kn_{sp}v_g\Gamma\left(g_0+\frac{\partial g}{\partial N}\Delta N+\frac{\partial g}{\partial S}\Delta S\right)\approx\left[v_g\Gamma g_0-\frac{1}{\tau_{p0}}+v_g\Gamma\left(S_0+Kn_{sp}\right)\frac{\partial g}{\partial S}\right]\Delta S+$$

$$\left[v_g\Gamma\left(S_0+Kn_{sp}\right)\frac{\partial g}{\partial N}-\frac{\partial\frac{1}{\tau_p}}{\partial N}S_0\right]\Delta N, \tag{A10}$$

and from Eq. (A6) we have

$$\frac{\partial g}{\partial S}=\frac{g_N ln\left(\frac{N_0}{N_{tr}}\right)\left(-\frac{\Gamma\varepsilon}{V}\right)}{\left(1+\frac{\Gamma\varepsilon S_0}{V}\right)^2}=\frac{-\frac{\Gamma\varepsilon}{V}}{1+\frac{\Gamma\varepsilon S_0}{V}}g_0, \tag{A11-1}$$

$$\frac{\partial g}{\partial N}=\frac{g_N}{N_0\left(1+\frac{\Gamma\varepsilon S_0}{V}\right)}=\frac{g_0}{N_0 ln\left(\frac{N_0}{N_{tr}}\right)}. \tag{A11-2}$$

By assuming a constant optical internal loss, we also have

$$\frac{\partial\frac{1}{\tau_p}}{\partial N}=\frac{\partial[v_g(\alpha_i+\alpha_c)]}{\partial N}=v_g\frac{\partial\alpha_c}{\partial N}. \tag{A12}$$

Again, by utilizing Eq. (A8-1), Eq. (A8-3), and Eq. (A9-3) and ignoring higher order items, we can convert Eq. (A7) into

$$\frac{d\Delta N}{dt}=\eta\frac{I_0+\Delta I}{qV}-\left(\frac{1}{\tau_{n0}}+\frac{\partial\frac{1}{\tau_n}}{\partial N}\Delta N\right)(N_0+\Delta N)-\frac{v_g\Gamma}{V}\left(g_0+\frac{\partial g}{\partial N}\Delta N+\frac{\partial g}{\partial S}\Delta S\right)(S_0+$$

$$\Delta S)\approx-\frac{v_g\Gamma}{V}\left(S_0\frac{\partial g}{\partial S}+g_0\right)\Delta S-\left(\frac{v_g\Gamma}{V}S_0\frac{\partial g}{\partial N}+\frac{1}{\tau_{n0}}+\frac{\partial\frac{1}{\tau_n}}{\partial N}N_0\right)\Delta N+\eta\frac{\Delta I}{qV}, \tag{A13}$$

where

$$\frac{\partial \frac{1}{\tau_n}}{\partial N} = \frac{\partial (A+BN+CN^2)}{\partial N}\Big|_{N=N_0} = B + 2CN_0. \tag{A14}$$

By defining

$$A' \equiv -[v_g \Gamma g_0 - \frac{1}{\tau_{p0}} + v_g \Gamma\big(S_0 + Kn_{sp}\big)\frac{\partial g}{\partial S}] \approx v_g \Gamma g_0 \frac{\frac{\Gamma\varepsilon S_0}{V}}{1+\frac{\Gamma\varepsilon S_0}{V}}, \tag{A15-1}$$

$$B' \equiv v_g \Gamma\big(S_0 + Kn_{sp}\big)\frac{\partial g}{\partial N} - \frac{\partial \frac{1}{\tau_p}}{\partial N} S_0 \approx [\frac{v_g \Gamma g_0}{N_0 ln(\frac{N_0}{N_{tr}})} - v_g \frac{\partial \alpha_c}{\partial N}]S_0, \tag{A15-2}$$

$$D' \equiv \frac{v_g \Gamma}{V}(S_0 \frac{\partial g}{\partial S} + g_0) = \frac{v_g \Gamma g_0}{V}(\frac{-\frac{\Gamma\varepsilon S_0}{V}}{1+\frac{\Gamma\varepsilon S_0}{V}} + 1) = \frac{v_g \Gamma g_0}{V}\frac{1}{1+\frac{\Gamma\varepsilon S_0}{V}}, \tag{A15-3}$$

$$E' \equiv \frac{v_g \Gamma}{V} S_0 \frac{\partial g}{\partial N} + \frac{1}{\tau_{n0}} + \frac{\partial \frac{1}{\tau_n}}{\partial N} N_0 = \frac{v_g \Gamma g_0}{N_0 ln(\frac{N_0}{N_{tr}})}\frac{S_0}{V} + \frac{1}{\tau_{n0}} + (B + 2CN_0)N_0, \tag{A15-4}$$

we can rewrite Eq. (A10) and Eq. (A13) as

$$\frac{d\Delta S}{dt} = -A'\Delta S + B'\Delta N, \tag{A16-1}$$

$$\frac{d\Delta N}{dt} = -D'\Delta S - E'\Delta N + \eta \frac{\Delta I}{qV}. \tag{A16-2}$$

By applying Fourier transform on Eq. (A16-1) and Eq. (A16-2), we obtain

$$j\omega\Delta S = -A'\Delta S + B'\Delta N, \tag{A17-1}$$

$$j\omega\Delta N = -D'\Delta S - E'\Delta N + \eta \frac{\Delta I}{qV}. \tag{A17-2}$$

And by solving Eq. (A17) we can reach the standard AM response as

$$\frac{\Delta S}{\Delta I} = \frac{\eta}{qV}\frac{B'}{(j\omega)^2 + j\omega(A'+E') + (A'E'+B'D')} = \frac{\eta B'}{qV}\frac{1}{(j\omega)^2 + (j\omega)\frac{\omega_r}{Q} + \omega_r^2}. \tag{A18}$$

Here the relaxation oscillation frequency ω_r is defined as

$$\omega_r^2 = A'E' + B'D' = v_g \Gamma g_0 \frac{\frac{\Gamma\varepsilon S_0}{V}}{1+\frac{\Gamma\varepsilon S_0}{V}}\left[\frac{v_g \Gamma g_0}{N_0 ln(\frac{N_0}{N_{tr}})}\frac{S_0}{V} + \frac{1}{\tau_{n0}} + (B + 2CN_0)N_0\right] +$$

$$\frac{v_g \Gamma g_0}{V} \frac{S_0}{1+\frac{\Gamma \varepsilon S_0}{V}} \left[\frac{v_g \Gamma g_0}{N_0 \ln\left(\frac{N_0}{N_{tr}}\right)} - v_g \frac{\partial \alpha_c}{\partial N} \right] \approx \frac{v_g S_0 \Gamma g_N}{\tau_{p0} V N_0} \left[1 - \frac{1}{\Gamma} \frac{\partial \alpha_c / \partial N}{g_N / N_0} \right], \tag{A19}$$

by utilizing the conditions $A'E' \ll B'D'$, $1 + \frac{\Gamma \varepsilon S_0}{V} \approx 1$, $\frac{g_0}{ln\left(\frac{N_0}{N_{tr}}\right)} \approx g_N$, and $v_g \Gamma g_0 \approx \frac{1}{\tau_{p0}}$.

The quality factor Q is defined in

$$\frac{\omega_r}{Q} = A' + E' \approx \frac{\Gamma \varepsilon S_0}{\tau_{p0} V} + \frac{v_g \Gamma g_N}{N_0} \frac{S_0}{V} + \frac{1}{\tau_{n0}} + (B + 2CN_0) N_0, \tag{A20}$$

by utilizing the same conditions.

Appendix B List of Publications Related to the Thesis Work

Journals

P.1. Sangzhi Zhao and Xun Li, “Design and Simulation of a Directly Frequency Modulated DFB Laser,” *IEEE J. Quantum Electron.*, vol. 56, no. 6, pp. 1-9, Dec. 2020.

P.2. Sangzhi Zhao and Xun Li, “Modulation Bandwidth Improvement of Distributed Feedback Laser with Periodic Current Blocking Grating,” In Process.